

## NRC Publications Archive Archives des publications du CNRC

### The importance of accurately modelling soot and radiation coupling in laminar and laboratory-scale turbulent diffusion flames

Liu, Fengshan; Consalvi, Jean-Louis; Nmira, Fatiha

This publication could be one of several versions: author's original, accepted manuscript or the publisher's version. / La version de cette publication peut être l'une des suivantes : la version prépublication de l'auteur, la version acceptée du manuscrit ou la version de l'éditeur.

For the publisher's version, please access the DOI link below. / Pour consulter la version de l'éditeur, utilisez le lien DOI ci-dessous.

#### **Publisher's version / Version de l'éditeur:**

<https://doi.org/10.1016/j.combustflame.2022.112573>

*Combustion and Flame*, 2022-12-30

#### **NRC Publications Archive Record / Notice des Archives des publications du CNRC :**

<https://nrc-publications.canada.ca/eng/view/object/?id=4efe7547-fda8-40d4-9902-88b7ce4eefa1>

<https://publications-cnrc.canada.ca/fra/voir/objet/?id=4efe7547-fda8-40d4-9902-88b7ce4eefa1>

Access and use of this website and the material on it are subject to the Terms and Conditions set forth at

<https://nrc-publications.canada.ca/eng/copyright>

READ THESE TERMS AND CONDITIONS CAREFULLY BEFORE USING THIS WEBSITE.

L'accès à ce site Web et l'utilisation de son contenu sont assujettis aux conditions présentées dans le site

<https://publications-cnrc.canada.ca/fra/droits>

LISEZ CES CONDITIONS ATTENTIVEMENT AVANT D'UTILISER CE SITE WEB.

**Questions?** Contact the NRC Publications Archive team at

PublicationsArchive-ArchivesPublications@nrc-cnrc.gc.ca. If you wish to email the authors directly, please see the first page of the publication for their contact information.

**Vous avez des questions?** Nous pouvons vous aider. Pour communiquer directement avec un auteur, consultez la première page de la revue dans laquelle son article a été publié afin de trouver ses coordonnées. Si vous n'arrivez pas à les repérer, communiquez avec nous à PublicationsArchive-ArchivesPublications@nrc-cnrc.gc.ca.



ELSEVIER

Contents lists available at ScienceDirect

Combustion and Flame

journal homepage: [www.elsevier.com/locate/combustflame](http://www.elsevier.com/locate/combustflame)

# The importance of accurately modelling soot and radiation coupling in laminar and laboratory-scale turbulent diffusion flames

Fengshan Liu<sup>a,\*</sup>, Jean-Louis Consalvi<sup>b</sup>, Fatiha Nmira<sup>c</sup><sup>a</sup> Metrology Research Centre, National Research Council, 1200 Montreal Road, Ottawa, ON K1A 0R6, Canada<sup>b</sup> Aix-Marseille Université, IUSTI/UMR CNRS 7343, 5 rue E. Fermi, Marseille Cedex 13 13453, France<sup>c</sup> Direction R&D EDF, 6 Quai Watier, Chatou Cedex, 78401, France

## ARTICLE INFO

### Article history:

Received 1 May 2022

Revised 1 December 2022

Accepted 4 December 2022

Available online xxx

### Keywords:

Soot models

Non-gray thermal radiation

Soot/radiation interaction

Laminar diffusion flames

Turbulent diffusion flames

Turbulence/radiation interaction

## ABSTRACT

Ultrafine and highly light absorbing soot particles have been known to be harmful to human health and a major climate forcer. Understanding the mechanisms of soot formation and developing reliable and robust soot models are essential to design efficient and clean combustion systems. Thermal radiation is often the dominant heat transfer mode in both turbulent and laminar flames and affects soot formation through its influence on temperature. Significant progress has been made in modelling soot formation, thermal radiation transfer, and turbulence radiation interaction in hydrocarbon flames over the last three decades. However, the optically thin approximation has still been used to simplify thermal radiation transfer modelling and turbulence radiation interaction has often been neglected in soot formation modelling without proper justification. In this paper, soot models developed for laminar and laboratory scale turbulent jet diffusion flames, non-gray radiative heat transfer models, and turbulence radiation interaction models are reviewed. The aim of this review is to highlight the importance of thermal radiation heat transfer in both laminar and turbulent diffusion flames and turbulence radiation interaction in turbulent jet diffusion flames. Use of the optically thin approximation is often not justified even in laminar diffusion flames. This is particularly true in diffusion flames at elevated pressures or microgravity. Although the prediction of soot in both laminar and turbulent flames is primarily influenced by soot kinetic model, it is also significantly affected by aerosol dynamic model, thermal radiation heat transfer model, and turbulence radiation interaction model. It is important to accurately model soot aerosol dynamics and non-gray thermal radiation transfer in laminar diffusion flames and additionally to adequately model turbulence radiation interaction in turbulent flames for the purpose of validating reaction mechanisms and soot kinetic models.

Crown Copyright © 2022 Published by Elsevier Inc. on behalf of The Combustion Institute. All rights reserved.

## 1. Introduction

Global energy consumption and carbon dioxide emissions in the energy and power sectors will continue to increase as a result of accelerated growth in population and economy. To mitigate climate changes caused by combustion-generated CO<sub>2</sub> and soot emissions, considerable progress has been achieved in the production and utilization of renewable energy resources. However, combustion of fossil fuels is still the main source of energy and will remain so in the foreseeable future. In 2018, the major World energy supply sources were oil, coal, natural gas, and biofuels at 31.6%, 26.9%, 22.8%, and 9.3%, respectively [1]. It was estimated in the Interna-

tional Energy Outlook 2016 [2] that fossil fuels will continue to supply approximately 80% of the World's energy by 2040. Although progress in clean energy transitions will continue to grow rapidly, oil, natural gas, and coal will remain the major energy sources in the next few decades.

The drawbacks of fossil fuel combustion are the emissions of carbon dioxide (CO<sub>2</sub>) and other pollutants, such as nitric oxides (NO<sub>x</sub>), carbon monoxide (CO), unburnt hydrocarbons (UHCs), and soot, that are detrimental to human health, environment, and climate. Soot is a major by-product formed during incomplete combustion or pyrolysis of hydrocarbon fuels, biomass burning, and fires. Soot particles are ultrafine with a characteristic size ranging from a few to a few hundred nanometers and rich in carbon and contain a small amount of hydrogen and oxygen. Emissions of soot from combustion systems and fires have been known to pose serious health risks and play a significant role in climate forcing [3].

\* Corresponding author.

E-mail addresses: [fengshan.liu@nrc-cnrc.gc.ca](mailto:fengshan.liu@nrc-cnrc.gc.ca) (F. Liu), [jean-louis.consalvi@univ-amu.fr](mailto:jean-louis.consalvi@univ-amu.fr) (J.-L. Consalvi), [fatiha.nmira@edf.fr](mailto:fatiha.nmira@edf.fr) (F. Nmira).

**Nomenclature**

$a$	stretching factor
$A_v$	avogadro number, mol <sup>-1</sup>
$A_n$	PAH with $n$ rings
$C$	progress variable
$d$	diameter, m
$D$	diffusivity, m <sup>2</sup> /s
$f$	$k$ -distribution function
$f_s$	soot volume fraction
$F_i$	line-shape profile of line $i$ , 1/cm <sup>-1</sup>
$g_0$	quadrature point
$g$	cumulative $k$ -distribution
$G$	incident radiation, W/m <sup>2</sup>
$H$	heaviside function
$I$	radiative intensity, W/m <sup>2</sup> sr
$k$	absorption coefficient variable or absorptive index, m <sup>-1</sup> or (–)
$k_B$	Boltzmann constant, J/K
$L$	characteristic length scale, m
$m$	complex refractive index
$M_i$	molar mass of species $i$ , kg/mol
$n$	particle number density or refractive index, m <sup>-3</sup> or (–)
$N_s$	Soot number density, m <sup>-3</sup>
$N$	molecule number density, mol/m <sup>3</sup>
$p$	pressure, Pa
$P$	probability density function or Filtered density function
$\dot{q}_R''$	net radiative flux, W/m <sup>2</sup>
$Q_{net}$	total radiative heat loss, W
$S$	Soot specific surface area or spectra line strength, m <sup>-1</sup> or (–)
$S_i$	strength of the $i$ th spectral line, cm <sup>-1</sup> /mol m <sup>-2</sup>
$S_R$	radiative source term, W/m <sup>3</sup>
$t$	time, s
$T$	temperature, K
$T_p$	blackbody source temperature, K
$u_i$	$i$ th velocity component, m/s
$V_{T,i}$	$i$ th velocity thermophoresis component, m/s
$X_R$	enthalpy defect, J/kg
$x_i$	mole fraction of the species $i$
$Y_i$	mass fraction of the species $i$
$Z$	mixture fraction

**Greek symbols**

$\dot{\omega}_s$	Soot production rates, kg/m <sup>3</sup> /s
$\chi$	scalar dissipation rate, s <sup>-1</sup>
$\chi_R$	radiant fraction
$\Delta$	LES filter scale, m
$\epsilon$	emissivity, $\mu$ m
$\eta$	wavenumber, cm <sup>-1</sup>
$\kappa$	absorption coefficient, m <sup>-1</sup>
$\lambda$	wavelength, $\mu$ m
$\mu$	viscosity, kg/ms <sup>2</sup>
$\Omega$	solid angle, sr
$\omega$	subgrid intermittency
$\Phi$	scattering phase function
$\phi$	scalar or composition variable vector
$\rho$	density, kg/m <sup>3</sup>
$\sigma$	Stefan–Boltzmann constant or scattering coefficient, W/m <sup>2</sup> /K <sup>4</sup> or m <sup>-1</sup>
$\tau$	optical thickness

**Subscripts**

$abs$	absorption
$b$	blackbody
$emi$	emission
$g$	gas
$p$	Planck-mean value or particle
$s$	Soot
$\eta$	at wavenumber $\eta$
$0$	reference state

**Superscripts**

$fl$	flamelet
------	----------

**Operators**

$\langle \phi \rangle$	time averaged value of $\phi$
$\langle \phi \rangle_{\Delta}$	filtered value of $\phi$
$\langle A B \rangle$	conditional mean of A given B
$\phi'$	fluctuation of $\phi$
$\tilde{\phi}$	density-weighted filtered value of $\phi$
$\bar{\phi}$	Favre averaged value of $\phi$

**Acronyms**

CMC	conditional moment closure
DNS	direct numerical simulation
DOM	discrete ordinates method
PDF	filtered density function
FPV	flamelet progress variable
FS	full spectrum
FSK	full-spectrum $k$ -distribution
FVM	finite volume method
HACA	hydrogen-abstraction carbon-addition
HFPDF	hybrid flamelet transported PDF method
HFTFDF	hybrid flamelet transported FDF method
LBL	line by line
LES	large eddy simulation
MC	Monte Carlo
MOM	method of moment
NBCK	narrow-band correlated- $k$
OTA	optically-thin approximation
OTFA	optically-thin fluctuation approximation
PAH	polycyclic aromatic hydrocarbon
PDF	probability density function
PMC	photon Monte Carlo
RANS	Reynolds-averaged Navier–Stokes
RCFSK	rank-correlated full-spectrum $k$ -distribution
ReS	resolved-scale fluctuations
RHT	radiative heat transfer
RTE	radiative transfer equation
SGS	subgrid-scale fluctuations
SLF	steady laminar flamelet model
SLW	spectral line weighted-sum-of-gray-gases
SNB	statistical narrow-band
SNBCK	statistical narrow-band based correlated- $k$
TCI	turbulence/chemistry interaction
TPDF	transported PDF method
TRI	turbulence-radiation interaction
TSI	turbulence/soot interaction
WBCK	wide-band correlated- $k$
WSGG	weighted-sum-of-gray-gases

Significant research and development efforts have been devoted to design cleaner combustion devices without losing efficiency and to modify the fuel properties by blending with low-carbon fuels or additives. To achieve these goals, it is paramount to gain detailed understanding of the physicochemical mechanisms govern-

ing the soot formation processes and the kinetic pathways from fuel to soot. Although emission of soot from combustion systems and fires is undesirable, its formation is beneficial in certain applications, such as in furnaces and boilers to enhance radiation heat transfer from flames to the load and in carbon black production from hydrocarbons. It is hence important to develop capabilities of effectively controlling soot formation and oxidation.

Despite significant progress in the understanding of detailed mechanisms of soot formation in hydrocarbon combustion, soot formation remains one of the most formidable and unresolved problems in the field of combustion, especially the details of soot inception from gas-phase precursor species to condensed phase particles [4–7]. Like other combustion-generated pollutants, such as  $\text{NO}_x$ , CO, and UHC, the soot related processes, namely inception, surface growth, and oxidation, are kinetically controlled and highly sensitive to temperature. This means that accurate prediction of temperature is a prerequisite to accurate prediction of soot and other pollutants.

On the other hand, thermal radiation heat transfer is an important and often a dominant heat transfer mode in small-scale flames and large-scale combustion systems and fires, respectively. This is because the radiative heat transfer rate increases rapidly with increasing temperature due to the exponential dependence of the blackbody radiation intensity on temperature. The importance of radiation heat transfer depends on thermal conditions, such as temperature and concentrations of participating species (mainly CO,  $\text{CO}_2$ ,  $\text{H}_2\text{O}$ , and soot in gaseous fuel combustion, as well as particulates in solid fuel flames), and flow characteristics, such as pressure, length scale, and residence time, making it particularly important in sooting flames, high-pressure combustion systems, large-scale furnaces and boilers, fires, and flames in microgravity.

Well-controlled laminar flames, such as laminar coflow diffusion flames, have been frequently used as a preferred configuration to gain fundamental understanding of the effects of certain parameters on soot formation, such as pressure [8] and additives [9]. This is because such stable flames are closely related to practical jet diffusion flames, allow reproducible measurements using optical diagnostics, and have a fairly simple flow field to permit tractable numerical simulation using advanced physical and chemical models, e.g., [10–14]. In particular, several well-documented laminar coflow diffusion flames with well-defined burner inlet conditions have been selected as target flames at the International Sooting Flame Workshop [15]. Although radiation heat transfer in laminar coflow diffusion flames at atmospheric pressure is in general less important than in large-scale turbulent flames, it can still lower the peak flame temperature by about 100 K at normal gravity [16] and even more in the flame centerline region around the flame tip [16,17]. The effect of radiation heat transfer on flame temperature can become much more significant at microgravity due to enlarged flame size and longer residence time [17,18]. Such a large variation in temperature could have significant impact on the prediction of species that are highly sensitive to temperature, such as  $\text{NO}_x$ , PAHs, and soot. It is therefore critical to model radiative heat transfer accurately in both small-scale laminar flames and large-scale turbulent flames for model validation and prediction of soot and other pollutants. Radiative heat transfer is enhanced in sooting flames due to the presence of soot. Unlike gaseous radiating species, namely  $\text{CO}_2$ ,  $\text{H}_2\text{O}$ , CO, and hydrocarbons, which have distinct narrow bands consisting of a large number of spectral lines, soot absorbs and emits continuously over the entire spectral range of interest in combustion research from visible to mid infrared. Although the visible spectrum has negligible contributions to thermal radiation at typical flame temperatures, it is of great interest to optically based soot diagnostics.

Accurate modelling of radiative heat transfer in flames and combustion systems is challenging and time-consuming due to the strongly spatial, directional, and spectral dependence of radiative intensity. This is perhaps one of the main reasons for the often simplified treatment of radiative heat transfer modelling using the optically thin approximation (OTA) in many numerical studies of laminar and turbulent diffusion sooting flames [13,14,19,20], even though it is well-known that this approximation is questionable even in laminar diffusion flames [16,17]. Accurate modelling of thermal radiative heat transfer requires accurate solution to the radiative transfer equation (RTE) and an accurate representation of the spectral radiative properties of gaseous radiating species, mainly  $\text{CO}_2$  and  $\text{H}_2\text{O}$ , and particulates, such as soot, coal, biomass, and fly-ash particles. Various RTE solvers of different levels of accuracy and computational efficiency and radiative property models have been developed in the last three decades to model radiative heat transfer in a wide range of combustion applications, from laminar and turbulent flames to pulverized coal-fired furnaces and boilers [21]. Remarkable advances have also been made in the development of accurate yet computationally efficient gas radiation models in last two decades. In particular, global models, such as the weight-sum-of-gray gas (WSGG) model, the spectral-line based on weight-sum-of gray- gas (SLW) model, and full-spectrum correlated-k (FSCK) model, are now able to achieve solutions within few percents of line-by-line (LBL) accuracy with only a small fraction of the computational cost of LBL [22]. Accurate non-gray radiative property models have been increasingly employed for the simulations of lab-scale laminar flames and turbulent flames. However, incorporation of these radiation models into large-scale flame and fire modelling remains a challenge due to the excessive increase in computational effort. It is worth pointing out that the state-of-the-art radiative models are applicable not only to conventional fuel-air flames, but also to oxy-fuel flames and combustion applications with flue gas recirculation [23].

Due to the strong absorbing and emitting ability of soot over the entire spectrum, there is a strong coupling between soot formation and thermal radiation heat transfer, i.e., the presence of soot strongly enhances thermal radiation, which in turn significantly alters the soot related processes through affecting the temperature distribution. In general, thermal radiation reduces the peak temperatures in high-temperature regions but increases temperatures in low-temperature regions where there are appreciable concentrations of absorbing species, such as  $\text{CO}_2$ ,  $\text{H}_2\text{O}$  and particulates, i.e., it tends to smooth the temperature distribution.

In turbulent flames, besides dealing with the formidable issues of solving the RTE and modelling the highly non-linear turbulence and chemistry interaction, additional difficulties arise due to turbulence radiation interaction (TRI), which significantly increases the complexity of thermal radiation transfer modelling and becomes more important in turbulent sooting flames. Proper modelling of TRI incurs extra computational burden to the already computationally expensive turbulent combustion modelling. The importance of TRI in turbulent combustion modelling has drawn considerable research attention in the last two decades and the progress in TRI modelling has been reviewed by Coelho [24] and Modest and Hawthorth [23].

The importance of radiative heat transfer in flames, fires, and combustion systems has long been recognized and has been reviewed and discussed in several reviews and monographs [21,23–25]. These previous reviews provided a valuable overview and comprehensive summary of certain important aspects of radiative heat transfer in combustion science at the time of publication, such as in pulverized coal combustion systems [25], in turbulent flames [21,23,24], in radiation-induced flame extinction and laminar flame speed [21]. However, no comprehensive reviews of recent numerical studies of sooting flames of laboratory scale that emphasized

the importance of accurate prediction of non-gray thermal radiation or the coupling of soot and thermal radiation are currently available. Given the importance of accurate modelling of thermal radiation heat transfer in both laminar and turbulent sooting flames and the strong interest of developing capabilities of accurately modelling soot formation, we will review studies of modelling sooting flames fuelled with gaseous or vaporized liquid fuels, both laminar and turbulent diffusion flames. The objectives of this review are threefold: (1) to highlight the strong coupling between soot and radiation in both laminar and turbulent sooting flames and the importance of TRI in turbulent flames, (2) to show that it is in general necessary to use non-gray radiation models to accurately model thermal radiation heat transfer in both laminar and turbulent jet diffusion flames and the use of OTA should be used with caution, and (3) to demonstrate that it is feasible and practical to employ accurate global non-gray radiative models in sooting flame modelling. The term *accurate modelling* is employed throughout this article and needs to be quantified. For radiation modelling, it means that the predicted divergence of radiative flux (source term) and heat flux are within 10% of reference solutions, obtained with line-by-line and Monte Carlo solver of the RTE in decoupled flow/radiation calculations. For soot modelling, it refers to models that predict the peak soot volume fractions within about a factor of two compared to experimental data, which is quite ambitious considering the experimental uncertainties on soot measurements and the currently limited understanding of soot formation processes. The paper is organized as follows. In Section 2, the current understanding of soot formation mechanism and available soot models for laminar and turbulent flames are briefly reviewed with a focus on soot models. Section 3 is dedicated to modelling radiative heat transfer in laminar and turbulent flames, with emphases on the radiative properties of sooting flames, different methods to model these properties, theory and models of TRI, and coupling between radiation and soot in laminar and turbulent sooting diffusion flames. Finally, concluding remarks are provided in Section 4.

## 2. Soot formation modelling

A very large number of soot models have been proposed in the literature to describe soot formation and oxidation in different applications, including laminar flames, turbulent flames, in-cylinder engine combustion, fires, and pulverized coal combustion. Correspondingly, these soot models vary drastically in complexity and sophistication from fuel and smoke-point height based, acetylene based semi-empirical type models, to PAH based detailed soot models. The following discussion concerns only soot models developed and commonly used for modelling soot formation in laminar and laboratory-scale turbulent flames. Before discussing the soot models, it is useful to briefly review the current understanding of soot formation mechanisms since they form the core of soot model development.

### 2.1. Soot formation mechanisms

The mechanisms responsible for soot formation in hydrocarbon combustion have been extensively investigated and comprehensively reviewed recently by Wang [5], Wang and Chung [26], and Martin et al. [7]. The following physicochemical processes are involved in soot formation in flames fuelled with aliphatics [6]: (i) fuel pyrolysis and formation of radicals and intermediate hydrocarbon species, (ii) formation of benzene, (iii) formation and growth of PAHs, (iv) formation of incipient soot particles through coagulation and dimerization of PAHs, (v) formation of primary soot particles through coalescence, coagulation, and surface growth of incipient soot particles, (vi) formation of fractal-like soot aggregates through aggregation of primary soot particles in the presence of

surface reactions, and finally (vii) oxidation and oxidation-induced fragmentation of soot aggregates. Step (ii), formation of benzene, is the rate-limiting step in the overall process of soot formation for aliphatics. For soot formation in aromatic fuels Step (ii) will be bypassed and the formation of PAHs, i.e., Step (iii), becomes the rate-limiting step of soot formation process. These physicochemical processes can occur concurrently. For example, incipient soot particles can coagulate and coalesce and, at the same time, change in size through surface addition and oxidation reactions. The transition from gas-phase precursor species to condensed-phase incipient soot particles, i.e., Step (iv), is the critical step of soot formation but remains poorly understood [5,7].

It has been generally agreed that incipient soot particles have a characteristic diameter of about 1 to 3 nm and are likely liquid-like [5,27]. Soot inception plays a bottle-neck role in the subsequent soot growth even though it contributes negligibly to the mass of soot aggregates. This is because inception soot particles provide the initial soot surface for heterogeneous surface reactions and PAH adsorption and are much smaller than mature soot. Different soot inception mechanisms have been proposed and can be grouped into two types: (i) physical PAH clustering or dimerization held together by van der Waals forces and (ii) chemical inception mechanism in which smaller PAHs with aliphatic chains are chemically linked through bond formation. Moderately sized stable PAHs with four (pyrene, A4) to seven (coronene, A7) rings have been favored to be the precursor PAH species in the dimerization-based soot inception mechanism, since the concentrations of these PAHs in flames are of similar orders of magnitude as the number densities of soot nuclei [5]. To date, physical dimerization of moderately sized PAHs has been commonly assumed in formulating soot inception models in laminar flame modelling [28–31], though theoretical calculations have shown that it is thermodynamically unfavorable at flame temperatures [32,33]. Both the physical and chemical soot inception mechanisms suffer deficiencies [5]. To overcome the drawback of physical PAH dimerization in modelling incipient soot formed physically through reversible PAH clustering, hybrid PAH dimerization based soot inception models, which allow chemical bond formation in dimers formed by physical dimerization, have been proposed [34,35]. It is also worth noticing that recent research on soot inception has suggested that benzene and smaller PAHs are likely important precursor species for soot inception based on both numerical [34,36] and experimental [37] studies and clustering of hydrocarbons by radical-chain reactions (CHRCR) may be an important mechanism for PAH growth and soot inception [38]. These new developments are currently under evaluation, e.g., [39] and have not been extensively used in modelling sooting flames.

Once formed, the incipient soot particles provide initial surface for subsequent heterogeneous surface reactions with hydrocarbons and PAH adsorption and undergo coagulation, resulting in an increase in particle size and mass. It has been widely accepted that the hydrogen abstraction acetylene addition (HACA) reaction sequence [28,40] is the dominant mechanism for soot particle surface growth via heterogeneous surface reactions. In addition to the HACA surface growth pathway, PAH adsorption also plays an important role in soot particle surface growth.

Oxygen molecules and O and OH radicals have been considered the dominant contributor for soot oxidation in flames. Although soot oxidation by O radicals was explicitly taken into account in some studies [16,19,41,42], it has been neglected in some other studies, e.g., [28,43,44] and all numerical studies of soot formation in laminar flames using the CoFlame code [31]. The absence of explicit contribution of soot oxidation by O radicals in soot models may be based on the considerations that the collision efficiencies of O and OH with soot particles are subject to uncertainty and O and OH radicals nearly overlap spatially along the flame front.

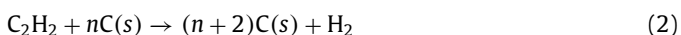
## 2.2. Soot models

Soot particles are fractal-like aggregates as a result of coagulation and aggregation of primary particles in the presence of inception and surface growth. Therefore, soot models consist of two aspects: one is the soot kinetics describing the processes of inception, surface growth, and oxidation, the other is the soot particle dynamics dealing with the particle morphology and size distribution. The two aspects may be modelled separately, similar to inception, surface growth, and oxidation in soot kinetics. In this section, we will summarize models commonly used in modelling soot formation in laminar and laboratory scale turbulent sooting flames.

### 2.2.1. Soot kinetic models

Soot inception modelling has drawn significant research attention, reflecting its bottle-neck role but largely unknown details in the overall soot formation processes. The general view of soot inception is that incipient soot particles appear when PAHs grow by physical and chemical processes to sufficiently large sizes. The majority of soot kinetics models developed in the literature differ mainly in the inception step and fall in one of the following two main types: semi-empirical models and detailed or PAH based models.

*Semi-empirical soot models* The acetylene based soot formation mechanism proposed by Leung et al. [45] was a relatively simple yet quite successful semi-empirical soot model. This model was developed based on the experimental observations that certain pyrolysis intermediates, rather than the parent fuel, in particular acetylene, are a good indicator for soot formation [46,47] in flames of aliphatic fuels. In acetylene based semi-empirical soot kinetics models, acetylene is assumed to be the only species that contributes to both soot inception and surface growth. Following Leung et al. [45], the soot inception and surface growth are modelled by the following irreversible and first-order reactions, respectively,



where  $\text{C}(s)$  denotes solid carbon. The soot inception and surface growth rates are given as

$$r_1 = k_1(T)[\text{C}_2\text{H}_2] \quad \text{in } [\text{kmol}/\text{m}^3/\text{s}] \quad (3)$$

$$r_2 = k_2(T)f(S)[\text{C}_2\text{H}_2] \quad (4)$$

where  $[\text{C}_2\text{H}_2]$  is the acetylene molar concentration,  $k_1$  and  $k_2$  are rate constants,  $S$  is the soot particle surface area per unit mixture volume and  $f(S)$  is a function of  $S$ , which has often been assumed to be equal to  $S$  [41,43,48] or the square root of  $S$  [16,45]. The square root dependence of soot surface growth rate on particle surface area was interpreted by qualitatively considering the effect of soot aging [45,49] in a simple way. Soot aging refers to the decrease in surface reactivity of soot particles as they grow larger due to the loss of active surface sites [50]. Although both expressions, i.e.,  $f(S) = S$  and  $f(S) = \sqrt{S}$ , can predict similar soot volume fractions, in both magnitude and distribution, in fuel/air diffusion flames of small hydrocarbons at atmospheric pressure when proper kinetic parameters were used, it has been shown that the use of  $f(S) = \sqrt{S}$  can better capture the effects of pressure [49] and oxygen concentration in the oxidizer [42] on soot formation in laminar coflow diffusion flames. Soot oxidation due to  $\text{O}_2$  and  $\text{O}$  and  $\text{OH}$  radicals is modelled by the following three irreversible reactions:



**Table 1**

Reaction rate constants of the semi-empirical soot model of Leung et al. [45] with  $k = AT^b \exp(-E/T)$  (in m, s, K).

$k_i$	$A$	$b$	$E$	Equation
1	$10^4$	0	21,100	3
2	6000	0	12,100	4
3	$10^4$	0.5	19,680	8
4	-	-	-	-
5	-	-	-	-

**Table 2**

Reaction rate constants of the semi-empirical soot model of Fairweather et al. [48] with  $k = AT^b \exp(-E/T)$  (in m, s, K).

$k_i$	$A$	$b$	$E$	Equation
1	$1.35 \times 10^6$	0	20,632	(3)
2	500	0	12,077	(4)
3	$1.78 \times 10^4$	0.5	19,625	(8)
4	-	-	-	-
5	-	-	-	-

**Table 3**

Reaction rate constants of the semi-empirical soot model of Liu et al. [16] with  $k = AT^b \exp(-E/T)$ .

$k_i$	$A$	$b$	$E$	Equation	Ref.
1	1000	0	16,103	(3)	[16]
2	1750	0	10,064	(4)	[16]
A	20	0	15,098	(9)	[52]
B	$4.46 \times 10^{-3}$	0	7650	(9)	[52]
T	$1.15 \times 10^5$	0	48,817	(9)	[52]
Z	21.3	0	-2063	(9)	[52]
4	$1.27 \times 10^3$	0	0	(10)	[52]
5	665.5	0	0	(11)	[53]



Two different expressions for the rate of soot oxidation by  $\text{O}_2$  have been used. One is the expression of Lee et al. [51] given below

$$r_3 = k_3(T)S[\text{O}_2] \quad (8)$$

where  $[\text{O}_2]$  is  $\text{O}_2$  molar concentration. The other is the Nagle-Strickland-Constable (NSC)  $\text{O}_2$  oxidation model given below (in  $\text{kg m}^{-2} \text{s}^{-1}$ ) [52]

$$r_3 = 120 \left[ \frac{k_A x_{\text{O}_2} \chi}{1 + k_Z x_{\text{O}_2}} + k_B x_{\text{O}_2} (1 - \chi) \right], \quad \chi = \left[ 1 + \frac{k_T}{k_B x_{\text{O}_2}} \right] \quad (9)$$

It should be pointed out that  $k_B$  in Eq. (9) is a reaction constant and not the Boltzmann constant. The rates of soot oxidation by  $\text{OH}$  and  $\text{O}$  radicals are expressed as

$$r_4 = \varphi_{\text{OH}} k_4(T) T^{-1/2} x_{\text{OH}} \quad (10)$$

$$r_5 = \varphi_{\text{O}} k_5(T) T^{-1/2} x_{\text{O}} \quad (11)$$

where  $x_i$  denotes the mole fraction of species  $i$  and  $\varphi_{\text{OH}}$  and  $\varphi_{\text{O}}$  are respectively the collision efficiency of  $\text{OH}$  and  $\text{O}$  radicals on soot surface. The rates of all three oxidation reactions shown above are for per unit soot particle surface. Different reaction rate constants in  $R_1$  to  $R_5$  have been proposed in the literature and the commonly used values are summarized in Tables 1–3.

It is noticed that soot oxidation by  $\text{OH}$  and  $\text{O}$  radicals was not considered in the studies of Leung et al. [45] and Fairweather et al. [48]. In more recent studies, Lindstedt and co-workers have incorporated soot oxidation by  $\text{O}$  and  $\text{OH}$  radicals in a series of numerical studies of turbulent diffusion flames [19,20,54] using refined

semi-empirical soot kinetic models. The model constants of Leung et al. [45] and Fairweather et al. [48] given in Tables 1 and 2 have nearly the same activation energies, but quite different prefactors  $A$ . This is because the model parameters of Leung et al. [45] were developed for  $f(S) = \sqrt{S}$ , while those of Fairweather et al. [48] for  $f(S) = S$ . Likewise, the model parameters listed in Table 3 were modified from those of Leung et al. [45] given in Table 1 and are also intended for  $f(S) = \sqrt{S}$ . The collision efficiency of OH and O on soot particle surface was assumed to be 0.1 [52] and 0.5 [53], respectively. However, the collision efficiency of both OH and O was assumed to be 0.2 in the study of Liu et al. [16].

The acetylene based soot models described above provide the rates for soot particle inception, surface growth, and oxidation and are given as

$$S_{incept} = \frac{2}{C_{min}} A_p r_1 \quad (12)$$

where  $C_{min}$  is the assumed number of carbon atoms in incipient soot particles and  $A_p$  is Avogadro's constant. Typical values of  $C_{min}$  are 100 [45], 700 [16], and 90,000 [48], giving the incipient soot particle diameter of about 1.2, 2.4, and 11.9 nm, respectively.

$$S_{sg} = 2r_2 M_s \quad (13)$$

where  $M_s$  is the carbon molar mass (12 g/mol).

$$S_{ox} = -(r_3 + r_4 + r_5) S M_s \quad (14)$$

Then the source terms in the transport equations for soot mass fraction  $S_{Y_s}$  and soot particle number density per unit mixture mass  $S_{N_s}$  are respectively expressed as

$$S_{Y_s} = 2r_1 M_s + 2r_2 M_s - (r_3 + r_4 + r_5) S M_s \quad (15)$$

$$S_{N_s} = \frac{2}{C_{min}} A_p r_1 - 2C_a d_p^{1/2} \sqrt{\frac{6k_B T}{\rho_s}} (\rho N_s)^2 \quad (16)$$

The second term on the right hand side of Eq. (16) represents particle coagulation and will be discussed in Section 2.2.2. The soot particle diameter  $d_p$  is related to  $Y_s$  and  $N_s$  as

$$d_p = \left( \frac{6}{\pi} \frac{\rho}{\rho_s} \frac{Y_s}{\rho N_s} \right)^{1/3} \quad (17)$$

The acetylene based semi-empirical soot models have been extensively used to model soot formation in diffusion flames of aliphatic fuels. These studies include laminar counterflow diffusion flames [45,55–57], laminar coflow diffusion flames [16,18,41,43,49,58–64], and turbulent jet diffusion flames [48,52,65,66] as an incomplete list. They have been also used for the simulations of high-pressure n-dodecane and heptane spray flames [67,67,68]. It is worth pointing out that Liu et al. [43] introduced temperature dependent factors to modify the soot oxidation rates by  $O_2$  and OH within the frame work of acetylene based semi-empirical soot model to predict the transition from non-smoking to smoking of a laminar coflow ethylene/air diffusion flame with increasing the fuel flow rate.

Since soot inception has been found to be associated with the formation of PAHs, the assumption that soot inception is directly linked to acetylene may cause significant error in the predicted location of soot inception in flames of heavier fuels than  $C_2$ , especially in aromatic fuels. Another drawback of acetylene based semi-empirical soot models is that they are unable to capture the chemical effects of reactive additives on soot formation, such as  $H_2$  [69]. To improve the acetylene based soot inception model, Lindstedt [70] proposed that both acetylene and benzene contribute to soot inception. In this improved semi-empirical soot model, soot inception is modelled by the following two reactions



**Table 4**

Reaction rate constants of the semi-empirical soot model of Lindstedt [70] with  $k = AT^b \exp(-E/T)$  (in m, s, K).

$k_i$	$A$	$b$	$E$	Equation
18	$0.63 \times 10^4$	0	21,000	(20)
19	$0.75 \times 10^5$	0	21,000	(21)
2	$0.75 \times 10^3$	0.0	12,100	(4)
3	$0.12 \times 10^6$	0.5	19,800	(8)



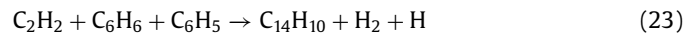
The corresponding reaction rates are given as

$$r_{18} = k_{18}(T)[C_2H_2] \quad \text{in [kmol/m}^3\text{/s]} \quad (20)$$

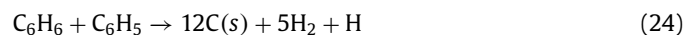
$$r_{19} = k_{19}(T)[C_6H_6] \quad \text{in [kmol/m}^3\text{/s]} \quad (21)$$

The rates of these two soot inception reactions, the surface growth by  $C_2H_2$  addition assuming  $f(S) = S$ , and oxidation by  $O_2$  using the Lee et al. model provided by Lindstedt [70] are summarized in Table 4. In this improved semi-empirical soot model, soot oxidation by OH and O radicals was again not considered.

Another improved semi-empirical soot model was developed by Hall et al. [71] which assumed that soot inception rate is related to the formation rate of two- and three-ringed aromatics ( $C_{10}H_7$  and  $C_{14}H_{10}$ ), which in turn are formed from the following two reactions



The formation rates of  $C_{10}H_7$  and  $C_{14}H_{10}$  are estimated by assuming that the intermediates are in steady-state and  $[H_2] \gg [C_2H_2]$ . The resultant soot inception rate can be found in [72,73,71]. Beltrame et al. [74] proposed to model soot inception by the following global reaction between benzene and phenyl



In these improved semi-empirical soot inception models, it is necessary to either employ a more detailed gas-phase reaction mechanism that includes reaction pathways leading to benzene and PAH formation or estimate the concentrations of precursor species using a simplified model, such as a global reaction as in Beltrame et al. [74], or assuming steady-state intermediates as in [71]. These improved semi-empirical soot models have been used to model soot formation in laminar diffusion flames [17,70,72,74] and turbulent jet diffusion flames [73,75,76].

Further efforts have also been made to improve semi-empirical soot kinetic models in both the soot inception and surface growth steps. Smooke et al. [77] modelled soot inception based on the formation rates of two- and three-ringed aromatics proposed by Hall et al. [71] and the surface growth by using the modified HACA mechanism of Colket and Hall [78] in their numerical study of soot formation in laminar coflow nitrogen-diluted ethylene diffusion flames. Lindstedt and Louloudi [19] used a refined semi-empirical soot model and a method of moment for soot aerosol dynamics to model two turbulent ethylene diffusion flames. In the soot kinetic model, soot inception was attributed to  $C_2H_2$  as in Leung et al. [45], while soot surface growth through  $C_2H_2$  addition was modelled based on the similarity between soot surface chemistry and that of naphthalene. Soot oxidation was modelled as surface reactions with  $O_2$  and OH and O radicals. The details of this soot kinetic model and rate constants are given in Lindstedt and Louloudi [19]. In a later study, Schiener and Lindstedt [54] assumed pyrene as incipient soot particles and it is formed through  $8C_2H_2$

→ C<sub>16</sub>H<sub>10</sub> + 3H<sub>2</sub>, i.e., soot nucleation was modelled as a global reaction step from acetylene to pyrene with the rate fitted using results from detailed chemistry, while soot surface growth and oxidation remained the same as those in Lindstedt and Louloudi [19]. These refined semi-empirical soot kinetic models were developed to incorporate the main features of experimentally observed soot inception and surface growth without invoking detailed PAH chemistry.

**Detailed soot models** Although the details of transition from gas-phase precursor species to condensed incipient soot particles remain unresolved, it has been widely accepted that PAHs are precursor species for soot inception in hydrocarbon flames [5,7,40]. Consequently, it is important to develop soot inception models using PAHs as building blocks, even though the dominant PAHs contributing to soot inception are still subject to debate and ongoing investigations.

Detailed soot models are mechanistic in nature and are developed to describe soot formation kinetics at elemental reaction level. These models have the following two features: (1) soot inception is modelled as physical and/or chemical interactions among PAH precursor species, and (2) the PAHs involved in soot inception are predicted from a detailed gas-phase reaction mechanism that incorporates known PAH formation pathways. The main differences between the semi-empirical and detailed soot kinetic models are twofold. First, in semi-empirical soot models the PAH soot precursors are either represented by a smaller stable species, typically C<sub>2</sub>H<sub>2</sub>, as surrogate of PAHs or modelled by some assumed global reactions. Second, the soot surface growth step in semi-empirical models is formulated based on C<sub>2</sub>H<sub>2</sub> addition only, i.e., without PAH adsorption, while detailed soot kinetic models typically account for both the HACA mechanism and PAH adsorption in the soot surface growth step. It is worth pointing out that there are currently large uncertainties in the formation and growth pathways of aromatics beyond benzene [7]. As such, the performance of a detailed soot model is influenced by the PAH formation sub-mechanism of the selected gas-phase chemistry model mainly through the soot inception step and the surface growth by PAH adsorption.

The majority of PAH based soot inception models used in flame modelling assume that incipient soot particles are formed as a result of physical dimerization of moderately sized PAHs. Soot inception due to irreversible dimerization or coagulation of two PAH molecules through collision and sticking is assumed to proceed as



Dimers are considered incipient soot particles that provide initial surface for subsequent growth and oxidation through surface reactions and PAH adsorption. Frenklach and Wang [79] and Blanquart and Pitsch [80] provided the general expression for the formation rate of dimers of two PAHs of any size based on the gas kinetic theory. In the particular case of homogeneous dimerization by two identical PAH molecules, the soot inception rate is calculated as

$$S_{\text{incept}} = 2.2\gamma \sqrt{\frac{4\pi k_B T}{C_{\text{mass}} N_{C,\text{PAH}}}} d_{\text{PAH}}^2 A_v^2 [\text{PAH}]^2 \quad (26)$$

where  $\gamma$  is the sticking efficiency to account for the short lifetime of dimers [80], 2.2 is the van der Waals enhancement factor,  $k_B$  is the Boltzmann constant,  $C_{\text{mass}}$  is the mass of a carbon atom,  $N_{C,\text{PAH}}$  is the number of carbon atoms in the PAH molecule,  $d_{\text{PAH}}$  is the average diameter of PAH molecule and is estimated as  $d_{\text{PAH}} = d_A \sqrt{2N_{C,\text{PAH}}/3}$  with  $d_A = 1.395\sqrt{3}$  Å being the size of a single aromatic ring [79], and  $[\text{PAH}]$  indicates the molar concentration of the PAH species involved. Pyrene has been the most widely assumed PAH species for soot inception through physical dimer-

**Table 5**

Reactions involved in the HACA mechanism for soot surface growth and oxidation [28] with  $k = AT^b \exp(-E/RT)$ .

No.	Reaction	A (cm <sup>3</sup> /mol/s)	n	E(kcal/mol)
S <sub>1</sub>	C <sub>s-H</sub> + H ↔ C <sub>s</sub> <sup>*</sup> + H <sub>2</sub>	4.2 × 10 <sup>13</sup>	0	13.0
S <sub>2</sub>	C <sub>s-H</sub> + OH ↔ C <sub>s</sub> <sup>*</sup> + H <sub>2</sub> O	1.0 × 10 <sup>10</sup>	0.734	1.43
S <sub>3</sub>	C <sub>s</sub> <sup>*</sup> + H → C <sub>s-H</sub>	2.0 × 10 <sup>13</sup>	0	0
S <sub>4</sub>	C <sub>s</sub> <sup>*</sup> + C <sub>2</sub> H <sub>2</sub> → C <sub>s+2-H</sub>	8.0 × 10 <sup>7</sup>	1.56	3.8
S <sub>5</sub>	C <sub>s</sub> <sup>*</sup> + O <sub>2</sub> → 2CO + product	2.2 × 10 <sup>12</sup>	0	7.5
S <sub>6</sub>	C <sub>s-H</sub> + OH → CO + products	φ <sub>OH</sub> = 0.13		

ization after the studies of Frenklach and Wang [50,79] and Appel et al. [28].

In detailed soot models, the growth of soot particle mass has been exclusively modelled by surface addition reactions with C<sub>2</sub>H<sub>2</sub> through the hydrogen abstraction acetylene addition (HACA) mechanism and adsorption of PAH species upon collisions between soot particles and the involved PAH molecules and the adsorption rate is modelled based on the collision rate between soot particles and the PAHs. Similar to the situation of modelling soot inception, there is currently also no consensus on what PAHs contribute to soot particle surface growth through adsorption, though all soot models make the assumption that the same PAHs involved in soot inception also contribute to soot surface adsorption. The HACA mechanism of surface reactions with small hydrocarbon molecules is an analogy to the HACA mechanism for PAH growth [40]. The reactions involved in the HACA mechanism for soot surface growth are listed in Table 5 following Appel et al. [28].

The HACA mechanism describes the soot surface as composed of aromatic basal planes and edges sites. The surface sites can be saturated as denoted by C<sub>s-H</sub> or dehydrogenated as denoted by C<sub>s</sub><sup>\*</sup>. Reactions S<sub>1</sub> and S<sub>2</sub> are the abstraction process through which the saturated surface sites are activated by H and OH radicals to form surface radicals, C<sub>s</sub><sup>\*</sup>, which can also be deactivated by combination with H radical through reaction S<sub>3</sub>. Reaction S<sub>4</sub> is the step of acetylene addition to the surface radicals through which soot particles gain mass. The last two reactions in Table 5, i.e., S<sub>5</sub> and S<sub>6</sub>, are actually soot oxidation reactions by O<sub>2</sub> and OH radicals. It is worth pointing out that modified HACA mechanisms in terms of abstraction reactions and rate constants have also been proposed. Colket and Hall [78] put forward a slightly different version of the HACA mechanism from that of Appel et al. [28]. Blanquart and Pitsch presented a modified version of the HACA surface growth mechanism by allowing S<sub>3</sub> to be reversible and providing different rate constants for reactions S<sub>1</sub> to S<sub>4</sub> [80].

The rate of soot particle mass gain by reaction S<sub>4</sub> can be evaluated as Frenklach and Wang [50], [81]

$$S_{\text{sg}} = 2C_{\text{mass}}k_4[\text{C}_2\text{H}_2] \frac{\alpha \chi_{\text{C}_s^*} A_s N_s}{A_v} \quad (27)$$

where  $\chi_{\text{C}_s^*}$  is the number of dehydrogenated sites per unit surface area,  $A_s$  is the particle surface area,  $N_s$  is the particle number density (m<sup>-3</sup>), and  $\alpha$ , the steric factor, is a parameter between 0 and 1 introduced to model the decrease in soot surface reactivity due to aging [28,50]. Table 6 summarizes the values and expressions reported in the literature for  $\alpha$ .

Assuming C<sub>s</sub><sup>\*</sup> is in steady-state,  $\chi_{\text{C}_s^*}$  can be evaluated as Frenklach and Wang [50]:

$$\chi_{\text{C}_s^*} = \frac{(k_1[\text{H}] + k_2[\text{OH}])\chi_{\text{C}_{s-H}}}{k_{-1}[\text{H}_2] + k_{-2}[\text{H}_2\text{O}] + k_3[\text{H}] + k_4[\text{C}_2\text{H}_2] + k_5[\text{O}_2]} \quad (28)$$

where  $\chi_{\text{C}_{s-H}}$  is the number of sites per unit soot particle surface area and takes the value of 2.3 × 10<sup>15</sup> sites/cm<sup>2</sup> [50]. The rates of soot oxidation by O<sub>2</sub> and OH radicals are evaluated as:

$$S_{\text{ox},\text{O}_2} = -2C_{\text{mass}}k_5[\text{O}_2] \frac{\alpha \chi_{\text{C}_s^*} A_s N_s}{A_v} \quad (29)$$

**Table 6**

Proposed values and/or functional forms for the steric factor  $\alpha$ .  $\mu_1$  is the first size moment of the soot particle distribution, and  $a = 12.56 - 0.00563T$  and  $b = 1.38 + 0.00068T$ .  $A_p$  represents the particle age and  $\theta$  is the critical age.  $C$  is a not a constant and varies with flame condition.  $d_p$  is the primary particle diameter and  $d_{p,0} = 8$  nm.  $T_a$  is thermal age defined as  $\int_s T dt$ , i.e., integration of temperature with respect to residence time along streamline.

Ref.	Functions
Frenklach and Wang [50]	0.1
Apple et al. [28]	$\tanh\left(\frac{a}{\log(\mu_1)} + b\right)$
El-Leathy et al. [82]	$0.0017\exp(12100/T)$
Guo et al. [69]	$0.0045\exp(9000/T)$
Singh et al. [83]	$\begin{cases} 1.0 & \text{for } A_p \leq \theta \\ 0.2 & \text{for } A_p > \theta \end{cases}$
Singh et al. [83]	$0.02 + 0.8\exp(-CA_p)$
Veshkini et al. [84]	$\frac{6974.6}{T_a} \exp\left(-\frac{88.06}{T_a}\right)$
Gu et al. [85]	$\exp(-1.2d_p/d_{p,0})$

$$S_{\alpha,OH} = -C_{mass}\varphi_{OH}[\text{OH}]\beta_{OH}A_v \quad (30)$$

where  $\beta_{OH}$  is the collision rate between OH and soot particles and can be calculated using the gas kinetic theory similar to collision rate between PAHs of different sizes [50,80].

The above detailed soot model consisting of pyrene dimerization for soot inception and surface growth by the HACA mechanism of Appel et al. [28] and pyrene adsorption has been coupled with different soot aerosol dynamics models to successfully investigate the effects of different factors on soot formation in laminar coflow diffusion flames, such as additives and fuel blends [69,86–91] and pressure [92,93]. It has been demonstrated in several studies that the detailed soot model is capable of reproducing the chemical effects of reactive additives and blend fuels on soot formation, at least qualitatively. However, the main issue of this detailed soot model has been known to severely underpredict the soot volume fraction in the centerline region of laminar coflow diffusion flames [94]. Although this issue can be partially attributed to the uncertainty in the PAH formation sub-mechanism [94], there are also likely deficiencies in the soot inception and surface growth models. For example, due to absence of H and OH radicals in the centerline region of laminar coflow diffusion flames, the HACA mechanism is not activated. Zhang et al. [95] proposed the Carbon Addition Hydrogen Migration (CAHM) reactions as an additional mechanism for soot surface growth. The CAHM mechanism has not been incorporated into soot formation models since the importance of CAHM reactions to soot surface growth is subject to debate [96]. Another potential improvement of the current HACA mechanism in soot surface growth is the additional H-abstraction reactions to activate the surface sites by hydrocarbon radicals, such as  $\text{CH}_3$ ,  $\text{C}_3\text{H}_3$ , and  $\text{C}_2\text{H}$ , suggested by Wang et al. [30]. This enhanced HACA mechanism has not been used in modelling soot formation in laminar coflow diffusion flames.

Among detailed soot models developed recently for modelling soot formation in flames, the focus has been placed on the soot inception step. Blanquart and Pitsch [80] modelled soot inception as the dimerization of eight PAH species ranging from naphthalene ( $\text{C}_{10}\text{H}_8$ ) to cyclo[cd]pyrene ( $\text{C}_{18}\text{H}_{10}$ ) through collision and sticking. Wang et al. [30] modelled soot inception by considering both homogeneous dimerization (by two same PAHs) and heterogeneous dimerization (by two different PAHs) among eight PAHs starting from pyrene up to coronene with a PAH size dependent collision efficiency model. In addition, Wang et al. [30] also used an enhanced HACA mechanism discussed above to model soot formation in counterflow diffusion flames of binary fuels. In the CoFlame code, soot inception is modelled as collision and sticking among three PAHs, namely benzo[a]pyrene (BAPYR), secondary benzo[a]pyrenyl (BAPYR\*S), and benzo(ghi)fluoranthene (BGHIF),

with a constant ad hoc collision efficiency of 0.0001 [31]. Zhang et al. [97] considered five PAHs from  $\text{A}_2$  to BGHIF as the inception and PAH adsorption species in the modelling of soot formation in laminar coflow doped  $\text{CH}_4/\text{air}$  diffusion flames with n-heptane and toluene mixtures. The results showed that the predicted soot inception location is earlier, i.e., closer to the burner exit, than experimental measurements when smaller PAHs than pyrene were assumed as soot inception species. The same observation has also been made by Xing and Groth [98], who evaluated the performance of a two-equation acetylene based semi-empirical soot model and several detailed soot models in the prediction of two laminar coflow diffusion flames. It is noticed that the predicted soot onset location in laminar coflow diffusion flames is a good global indicator of soot inception models. On the other hand, Eaves et al. [36], Kholghy et al. [34], and Gleason et al. [37] suggested that smaller aromatic species as small as benzene are more important in soot inception.

Other recent developments in soot kinetics modelling include all three aspects from inception, surface growth, and oxidation. In soot inception modelling, Eaves et al. [36,99] showed the importance of reversibility of soot inception and PAH adsorption, while Kholghy et al. [34,35] demonstrated the importance of chemical bond formation in dimers formed through collisions. Veshkini et al. [84] proposed a thermal age dependent steric parameter  $\alpha$  to better model the decrease in soot surface reactivity due to aging. Finally, Khosousi and Dworkin [44] proposed a thermal age dependent steric parameter for soot oxidation rate by  $\text{O}_2$  to predict the transition from non-smoking to smoking of laminar coflow ethylene/air diffusion flames with increasing the fuel flow rate.

**Soot maturity** After inception, soot particles undergo various physical and chemical processes as they are convected through the flame and their physical and chemical properties vary continuously as they evolve from incipient and young particles to mature and fractal-like aggregates. Soot maturity refers to the state of soot between incipient and mature particles and can be characterized by C/H ratio, density, and the wavelength dependence of soot absorption function (dispersion exponent) [6,100]. It has been shown in several studies that the soot absorption function and dispersion exponent vary spatially in laminar diffusion flames [101–103]. These findings have profound implications not only in optically based soot diagnostics but also in soot model development and validation since the existing experimental data sets of soot volume fraction reported in the literature were obtained using soot maturity independent optical constants. The maturity dependent optical properties of soot particles also affect the prediction of radiative heat transfer in sooting flames. It is therefore important to extend the current capabilities of soot formation modelling in flames to soot maturity. Some efforts in this direction have been made by Eaves et al. [36] and Kholghy et al. [104].

### 2.2.2. Soot aerosol dynamics models

In addition to surface growth and oxidation, incipient soot particles also undergo coagulation and coalescence and later agglomeration and aggregation to form polydisperse fractal-like aggregates formed by primary particles [105,106]. The goal of aerosol dynamics models is to adequately model the soot particle size distribution while taking into account the fractal structure of soot particles. Although prediction of soot formation is predominately affected by the soot kinetic model, the soot aerosol dynamics model also plays a fairly important role in the predicted soot volume fraction and size distribution. This is because the particle size distribution and morphology affect the particle surface area available for growth and oxidation. Proper modelling of the soot aerosol dynamics aspect governing the soot particle and aggregate size distributions requires the solution to the multi-dimensional integro-differential population balance equation (PBE), which governs the

evolution of particle number density distribution and is computationally expensive to solve. The PBE can be written as Sung et al. [107], Xing et al. [108]

$$\begin{aligned} \frac{\partial n(\vec{x}, t; \vec{\varepsilon})}{\partial t} + \frac{\partial}{\partial x_j} ((u_j + V_{T_j})n(\vec{x}, t; \vec{\varepsilon})) - \frac{\partial}{\partial x_j} \left( D_s \frac{\partial n(\vec{x}, t; \vec{\varepsilon})}{\partial x_j} \right) \\ = \left. \frac{dn(\vec{x}, t; \vec{\varepsilon})}{dt} \right|_{\text{incep+agg+sg+adsorp+\alpha}} \end{aligned} \quad (31)$$

where  $n(\vec{x}, t; \vec{\varepsilon})$  is the soot particle number density,  $\vec{x}$  is spatial variable,  $t$  is time,  $\vec{\varepsilon}$  is internal parameters for describing particles such as particle volume, particle surface area,  $u_j$  is flow velocity,  $V_{T_j}$  is soot particle thermophoretic velocity,  $D_s$  is soot diffusion coefficient. The term on the right hand side of Eq. (31) represents the source terms due to inception, agglomeration, surface growth through the HACA mechanism, PAH adsorption, and oxidation.

Models developed for soot aerosol dynamics in flame modelling have recently been reviewed by Rigopoulos [109] and summarized and evaluated by Xing et al. [108]. The discussion here is limited to the aerosol dynamics models commonly used in sooting flame modelling.

*Models assuming monodisperse spherical particles* The simplest method to deal with the aerosol dynamics aspect of soot particles is to assume that soot particles are monodisperse spherical particles, which is equivalent to assume that the particle size distribution is a  $\delta$ -Dirac function. Consequently, with the help of a particle coagulation model the soot aerosol can be fully described by only two variables: soot mass or volume fraction and soot particle number density, which are obtained by solving their transport equations. The particle diameter can be simply related to the volume fraction and number density [45]. This forms the basis for the two-equation implementation of different soot kinetic models. Particle coagulation has been modelled based on the gas kinetic theory and the coagulation rate is expressed as Leung et al. [45]

$$R_{\text{coagu}} = 2C_a d_p^{1/2} \sqrt{\frac{6k_B T}{\rho_s}} (\rho N_s)^2 \quad (32)$$

where  $C_a$  is a coagulation parameter,  $d_p$  is the soot particle diameter,  $k_B$  is the Boltzmann constant,  $\rho_s$  is the bulk density of soot and has a value of about 1.9 g/cm<sup>3</sup>,  $\rho$  is the gas mixture density, and  $N_s$  is the soot particle number density per unit mixture mass. It is noticed that  $R_{\text{coagu}}$  is a sink term in the transport equation of soot particle number density  $N_s$  since coagulation reduces the particle number density. The value of  $C_a$  has typically been set to 3 [48] or 9 [45]. The consequences of allowing particle coagulation into larger spherical particles are reduced particle number density and particle surface area at a given volume fraction, which in turn reduces the overall soot surface growth rate. It is worth pointing out that Liu et al. [16] neglected soot coagulation by setting  $C_a = 0$  based on previous experimental observations that primary soot particle number density remains almost constant in the growth region. In fact, neglect of primary soot particle coagulation is a better way to represent the particle surface area based on the consideration that agglomeration/aggregation of primary soot particles has a much smaller influence on particle surface area than assuming coagulated particles are spherical. The sensitivity of soot prediction using semi-empirical soot models and assuming monodisperse spherical particles to various model parameters in turbulent non-premixed ethylene/air jet flames has been systematically investigated by Ma et al. [66].

Although the two-equation implementation of soot models has typically been coupled with various semi-empirical soot kinetic models [16,17,41,43,45,48,52,61], it can also be coupled with a detailed soot model as in the studies of Guo et al. [69] and Trottier et al. [110].

#### Methods of moment

Moment methods do not seek to solve for the particle number density distribution, but to obtain the moments of the distribution by solving their transport equations with the help of a closure scheme. The transport equations of moments are obtained by integrating the PBE after multiplying it by the desired power of the internal parameters. The two lowest order moments, zeroth-order and first-order, have the significance of particle number density and particle volume fraction. A large number of methods of moment have been developed using different closure techniques [29,108,109,111]. These moment methods can be grouped into univariate methods and bivariate methods. The former methods consider the particle number density distribution in terms of particle volume only, i.e., assuming soot particles are polydisperse spherical particles, and deal with moments of particle volume, while in the latter methods the particle number density is a function of two internal parameters that are needed to describe soot fractal aggregates formed by monodisperse primary particles in terms of particle volume and particle surface area [29], total particle mass and number of primary particles [112], or particle volume and number of primary particles [108]. Therefore, the bivariate methods allow for a more realistic representation of polydisperse fractal-like soot particles, albeit they are more complex and computationally intensive since mixed moments have to be considered. In addition, bivariate moment methods rely on the approximation that primary particles within aggregates are monodisperse, which is reasonable for flames at atmospheric pressure [113] given the fairly narrow primary particle size distributions; however, it becomes questionable for flames at elevated pressures where the primary particle size distributions are quite broad [114–116]. In general, only few moments are sufficient to represent soot particle size distribution.

Xing et al. [108] applied two univariate (6-moment quadrature method of moment, QMOM, and 5-moment QMON-Radau) and two bivariate methods of moment (8-moment conditional quadrature method of moment, CQMOM, and 7-moment CQMOM-Radau) coupled with a soot kinetic model to predict soot formation in laminar coflow methane-ethanol/air diffusion flames at elevated pressures. The soot kinetic model assumes soot inception from acetylene, surface growth by the modified HACA mechanism of Blanquart and Pitsch [80], and oxidation by O<sub>2</sub> and O and OH radicals. Their results showed that the peak soot volume fractions at all three pressures (2, 4, and 6 atm) predicted by the two univariate methods, QMOM and QMON-Radau, are about 50% lower than those predicted by the two bivariate methods, i.e., CQMOM and CQMOM-Radau. In addition, implementing the same soot kinetic model into the two-equation approach resulted in peak soot volume fractions about 20% lower at all three pressures. These results are consistent with the notion that assuming soot aggregates as spherical particles significantly reduces the available area for surface growth and the neglect of primary particle coagulation in the two-equation soot model formulation is a better approximation as far as predicting soot volume fraction is concerned. In fact, the two-equation implementation of a soot kinetic model can be viewed as the simplest univariate method of moment where only the two lowest order moments are considered. The findings of Xing et al. [108] indicate that it is important to account for the aggregate morphology of soot particles in modelling soot formation and validation of soot kinetic models.

#### Sectional models

Sectional models represent the continuous particle number density  $n(\vec{x}, t; \vec{\varepsilon})$  by a discrete one. Assuming all soot particles are uniform in mass density, regardless of their size, and primary particles are spherical, the volume of a particle (aggregate) can be represented by its mass. In sectional methods, the entire range of particle mass from incipient particles at the lower end to a sufficiently large value at the upper end (larger than the mass of the heaviest particles in the system of interest) is discretized into a num-

ber of sections,  $N_{\text{sec}}$ , or mass bins. For fixed boundary mass values between sections, the methods are called fixed sectional methods, which are simpler and less computationally demanding. Only fixed sectional methods are discussed here. The range of particle mass is typically discretized in such a way that the mass ratio of two consecutive sections is a constant value, which is called the sectional spacing factor. Similar to the methods of moment, sectional methods can also be univariate or bivariate. Univariate sectional methods assume that the soot particles are spherical and one transport equation for the particle number density is solved in each section. In bivariate sectional methods, soot particles are treated as fractal-like aggregates formed by monodisperse primary particles and the soot particles in each section are described by aggregate number density and primary particle number density. Consequently, two transport equations in each section have to be solved: one for the aggregate number density and the other is for the primary particle number density. A detailed description of the sectional method implemented in the CoFlame code can be in Zhang et al. [11], [60], [117]. To resolve the heaviest soot particles in moderately sooting flames, about 30 sections have typically been used in numerical studies, making bivariate sectional methods computationally intensive.

Compared to the methods of moment, the main advantage of the sectional methods is that they can predict soot particle size distribution as well as the degree of particle aggregation. However, this advantage is gained at significantly more computational expense. This is because a quite large number of transport equations have to be solved to resolve the aggregate and primary particle number density in each section. In almost all the numerical studies using the CoFlame code, the particle mass was discretized into 35 sections, resulting in 70 transport equations to model the soot aerosol dynamics. In contrast, less than 10 transport equations are solved in the methods of moment [98,108]. So far, sectional methods have been mainly used to model soot aerosol dynamics in laminar flames due to their large computational cost, though univariate sectional methods have also been used to model soot aerosol dynamics in turbulent flames [20,54,118,119]. Soot formation modelling in laminar diffusion flames using the CoFlame code or its earlier variants has all been conducted with the bivariate sectional method for soot aerosol dynamics. Smooke and co-workers dealt with soot aerosol dynamics using a univariate sectional method in their numerical studies of soot formation in laminar coflow diffusion flames [10,77]. In recognition of the importance of soot aggregate structure to the determination of soot particle surface area, Lindstedt and co-workers have introduced approximations to account for soot aggregates in both the univariate moment method [19] and univariate sectional method [120]. Both bivariate methods of moment and bivariate sectional methods are able to provide much more realistic representation of soot aggregate surface area than their univariate counterparts at a higher computational cost, especially for the bivariate sectional methods. Therefore, similar results of soot prediction are expected from both the bivariate sectional methods and bivariate methods of moment when all other sub-models, such as gas-phase chemistry, soot kinetic model, and radiation model, remain the same.

### 2.3. Turbulence-soot interaction

The modelling of soot production in turbulent flames introduced additional difficulties related to turbulent mixing and turbulence/chemistry/soot production interactions. The main objective of this section is to review how these interactions are modelled in conjunction with the state-of-the-art turbulent combustion models. This literature review will be restricted to the modelling of well-documented canonical laboratory-scale turbulent flames, as those investigated in the ISF workshops [15], in which most of the

modelling developments have been assessed. This review is also limited to studies published from the beginning of the century and to non-premixed flames as they represent the vast majority of numerical studies devoted to soot production in turbulent flows. A specific review on the modelling of soot aerosol dynamics in turbulent flows was recently published and completes the present description [109].

The simultaneous developments of, on one hand, Direct Numerical Simulation (DNS) of canonical scenarios [121–126] and, on the other hand, temporally and spatially resolved soot measurement techniques [127–130], have greatly contributed to the understanding of how turbulence and soot production processes interact. These interactions were found to be mainly governed by the very low diffusivity of soot, i.e., it is transported differentially compared to gaseous species, and by the slow soot (and also PAHs) chemistry that results in time scales significantly longer than those of typical combustion processes. The main consequences are that: i) soot is confined to very thin structures with the soot field exhibiting a high spatially and temporally intermittent behaviour, ii) soot (and also PAHs) cannot be parameterized by local mixture fraction and scalar dissipation rate [121–124], iii) the differential diffusion governs the drift of soot in the mixture fraction space and determines the proximity of the soot to the flame which, in turn, influences soot reaction rates and radiative emission [121–123], iv) the local concentration of PAH is very sensitive to scalar dissipation rate with PAH and soot growth being favoured in regions of low dissipation rate and inhibited in regions of high dissipation rate [124]. In addition, it was found that soot is rapidly oxidized in the vicinity of the stoichiometric surface and soot leakage across the flame occurs due to local extinction events [125,126].

Table 7 summarizes the main numerical studies related to the simulations of well-documented lab-scale sooting turbulent non-premixed flames. These studies are ranked in chronological order which highlights the increasing level of sophistication over time with LES becoming the standard for the modelling of the flow field and with the use of PAH-based soot models and discretized PBE models for the modelling of soot chemistry and soot particle dynamics respectively. These later particle dynamics models allow a direct representation of the soot particle size distribution. LES accounts the intermittent nature of soot [119,131–134]. However, the soot formation/oxidation processes occur at the unresolved sub-grid scales and their interaction with turbulence must be modelled irrespective of the treatment of the flow field. This modelling is mainly dictated by the turbulent combustion model and Table 7 shows that four models were mainly considered, including the flamelet-based combustion models (SLF or FPV), transported PDF (TPDF) methods, hybrid-flamelet transported PDF (HFT-PDF) methods, and Conditional Moment Closure (CMC) approach. The soot production rates,  $\dot{\omega}_s(\phi_g, \phi_s)$ , depend on gas-phase related quantities,  $\phi_g$ , and soot-related quantities,  $\phi_s$ , such as soot mass fraction, number density, and particle size.  $\dot{\omega}_s(\phi_g, \phi_s)$  are highly non-linear functions of  $\phi_g$  and  $\phi_s$ , such as its Reynolds-averaged value in RANS,  $\langle \dot{\omega}_s \rangle$ , or its filtered value in LES,  $\langle \dot{\omega}_s \rangle_\Delta$ , cannot be directly related to mean or filtered values of  $\phi_g$  and  $\phi_s$ :

$$\langle \dot{\omega}_s(x, t) \rangle = \langle \rho \rangle \iint \frac{\dot{\omega}_s(\phi_g, \phi_s)}{\rho(\phi_g)} \tilde{P}(\phi_g, \phi_s) d\phi_g d\phi_s \neq \dot{\omega}_s(\tilde{\phi}_g, \tilde{\phi}_s) \quad (33)$$

$$\langle \dot{\omega}_s(x, t) \rangle_\Delta = \langle \rho \rangle_\Delta \iint \frac{\dot{\omega}_s(\phi_g, \phi_s)}{\rho(\phi_g)} \hat{P}_\Delta(\phi_g, \phi_s) d\phi_g d\phi_s \neq \dot{\omega}_s(\hat{\phi}_g, \hat{\phi}_s) \quad (34)$$

where the notations  $\tilde{\phi}$  and  $\hat{\phi}$  refer to density-weighted mean and filtered values of  $\phi$ , respectively.  $\Delta$  represents the LES filter width.

**Table 7**

Main modelling features of the RANS simulations and LES of turbulent non-premixed sooting flames. The abbreviations Nucl., SG, Cond., 2 Eq., MoM, SM, MC, and PMC refer to nucleation, surface growth, condensation, two-equation, Method of Moments, Sectional Methods, Monte Carlo and Photon Monte Carlo, respectively. Em. TRI and Abs. TRI indicate that emission TRI and absorption TRI in RANS and SGS emission TRI and SGI absorption TRI in LES are considered. OTFA indicates that absorption TRI in RANS or SGS absorption TRI in LES is neglected.

Ref. and year	Flame	Turb. model	Combustion	Mech.	Soot kinetic	Soot dynamics	RTE solver	Rad. property	TRI
Kronenburg et al. [137]	CH <sub>4</sub> jet 1–3 atm [153]	RANS	CMC	GRImech [154]	Nucl: C <sub>2</sub> H <sub>2</sub> SG: C <sub>2</sub> H <sub>2</sub>	2 Eq.	–	OTA	No
Brookes and Moss [65]	CH <sub>4</sub> jet 1–3 atm [153]	RANS	SLF		Nucl: C <sub>2</sub> H <sub>2</sub> SG: C <sub>2</sub> H <sub>2</sub>	2 Eq.	–	OTA	Emi. TRI
Pitsch et al. [139]	C <sub>2</sub> H <sub>4</sub> jet [156]	RANS	Unsteady flamelet	[155]	Nucl: PAH SG: HACA Cond. PAH	MoM		OTA	No
Lindstedt and Louloudi [19]	C <sub>2</sub> H <sub>4</sub> jet [156,157]	RANS	TPDF	Reduced	Nucl: C <sub>2</sub> H <sub>2</sub> SG: HACA	MoM		OTA	No
Wang et al. [158]	C <sub>3</sub> H <sub>8</sub> jet [159]	RANS	Eddy breakup	Grimech 3.0 [154] + Wang [160]	Nucl: PAH (A <sub>4</sub> ) SG: HACA Cond. PAH	MoM	P <sub>1</sub>	gray & FSCK	No
Aksit and Moss [149]	CH <sub>4</sub> jet 1–3 atm [153]	RANS	HFTPDF	Grimech [154]	Nucl: C <sub>2</sub> H <sub>2</sub> SG: C <sub>2</sub> H <sub>2</sub>	2 Eq.	–	OTA	No
Yunardi et al. [152]	C <sub>2</sub> H <sub>4</sub> jet [156]	RANS	CMC	Qin et al. [161]	Nucl: C <sub>2</sub> H <sub>2</sub> SG: C <sub>2</sub> H <sub>2</sub>	2 Eq.	–	OTA	Em TRI
Mehta et al. [145,162]	C <sub>2</sub> H <sub>4</sub> /CH <sub>4</sub> jets [159]	RANS	TPDF	Reduced Qin et al. [161]	Nucl: C <sub>2</sub> H <sub>2</sub> SG: HACA	MoM	PMC	LBL	Em. TRI Abs. TRI
Mueller et al. [131]	Delft III [165]	LES	RFPV	[163,164]	Nucl: PAH (A <sub>2</sub> ) SG: HACA + cond. PAH	MoM	–	OTA	No
Ref. Navarro-Martinez and Rigopoulos [132]	Flame CH <sub>4</sub> jet 1 atm [153]	Turb. model LES	Combustion CMC-RCCE	Mech. Lindstedt et al. [166]	Soot kinetic C <sub>2</sub> H <sub>2</sub>	Soot dynamics 2 Eq.	RTE solver –	Rad. property OTA	TRI or SGS TRI No
Gupta et al. [167]	Scaled-up flame D	LES	TPDF	Skeletal CH <sub>4</sub> /air [168]	State relationship	–	PMC	LBL	Em. TRI Abs. TRI
Donde et al. [135]	Delft III [165]	LES	HFTPDF	[163,164]	Nucl: PAH SG: HACA Cond. PAH	MoM	–	OTA	No
Xuan & Blanquart [144]	C <sub>2</sub> H <sub>4</sub> jet [138]	LES	RFPV	[163,164]	Nucl: PAH SG: HACA Cond. PAH	MoM	–	OTA	No
Pal et al. [169]	Scaled-up flame D	RANS	TPDF	Skeletal [168]	State relationship	–	PMC P <sub>1</sub> , P <sub>3</sub> FVM	LBL OTA FSCK	Emi. TRI Abs. TRI
Consalvi et al. [75,150]	C1-C3 jets	RANS	HFTPF	Qin et al. [161]	Nucl: C <sub>2</sub> H <sub>2</sub> /A <sub>1</sub> SG: C <sub>2</sub> H <sub>2</sub>	2 Eq.	FVM	WBCK	Emi. TRI OTFA
Rodrigues et al. [119,170]	C <sub>2</sub> H <sub>4</sub> /N <sub>2</sub> jet [138]	LES	FPV	KM2 [171]	Nucl: PAH SG: HACA Cond. PAH	SM	– [119] MC [170]	OTA [119] NBCK [170]	No [119] No [170]
Sewerin & Rigopoulos [172]	Delft III [165]	LES	TDFD	GRimech 1.2 [154]	Nucl: C <sub>2</sub> H <sub>2</sub> SG: C <sub>2</sub> H <sub>2</sub>	PBE	–	OTA	No
Jain and Xuan [136]	C <sub>2</sub> H <sub>4</sub> Jet [138]	LES	FPV	[173]	Nucl: PAH SG: HACA Cond. PAH	MoM	–	OTA	–
Yang et al. [133]	C <sub>2</sub> H <sub>4</sub> /H <sub>2</sub> /N <sub>2</sub> jet [128]	LES	FPV	[163,164]	Nucl: PAH SG: HACA Cond. PAH	MoM	–	OTA	No
Schiener and Lindstedt [54,146]	C <sub>2</sub> H <sub>4</sub> /N <sub>2</sub> [174] [174,175] Delft III [165]	RANS	TPDF	Reduced [19]	Nucl: C <sub>2</sub> H <sub>2</sub> SG: HACA	SM	–	OTA	No
Grader et al. [177]	C <sub>2</sub> H <sub>4</sub> jet [178–180]	LES	Pres. PDF	Reduced [176] + Sectional PAH	Nucl: PAH SG: C <sub>2</sub> H <sub>2</sub>	SM	–	OTA	No
Wu et al. [181]	C <sub>7</sub> H <sub>16</sub> pool fire [182]	DNS		Reduced [176]	Nucl: C <sub>2</sub> H <sub>2</sub> SG: C <sub>2</sub> H <sub>4</sub>	2 Eq.	PMC	LBL	–
Tian et al. [20]	C <sub>2</sub> H <sub>4</sub> /N <sub>2</sub> jet [138]	RANS	TPDF	Reduced [19]	Nucl: C <sub>2</sub> H <sub>2</sub> SG: HACA	SM	–	OTA	–
Huo et al. [147]	Delft III [165]	LES	TPDF	[183]	Nucl: PAH SG: HACA Cond. PAH	SM	–	OTA	No
Nmira et al. [134]	C <sub>2</sub> H <sub>4</sub> buoyant flame [184]	LES	SLF	Qin et al. [161]	Nucl: C <sub>2</sub> H <sub>2</sub> /A <sub>1</sub> SG: C <sub>2</sub> H <sub>2</sub>	2 Eq.	FVM	RCFSK	Emi. TRI OTFA

$\tilde{P}$  and  $\hat{P}_\Delta$  represent the joint density-weighted PDF and FDF, respectively.

*Flamelet-based models* The steady flamelet-based models, such as the steady laminar flamelet model (SLF) and the flamelet progress variable (FPV), assume that chemistry responds infinitely fast to perturbations from the turbulent flow field. Consequently, the gas-phase related quantities are described by a reduced set of

parameters, including the mixture fraction,  $Z$ , the scalar dissipation rate,  $\chi$ , in SLF, or a progress variable,  $C$ , in FPV and an enthalpy-related parameter,  $X_R$ , to account for the effects of radiative loss on the flamelet structure. The steady state flamelet equations are solved a priori to provide the state relationships for species mass fraction, temperature, and other thermochemical properties. These state relationships are stored in a flamelet library that results in

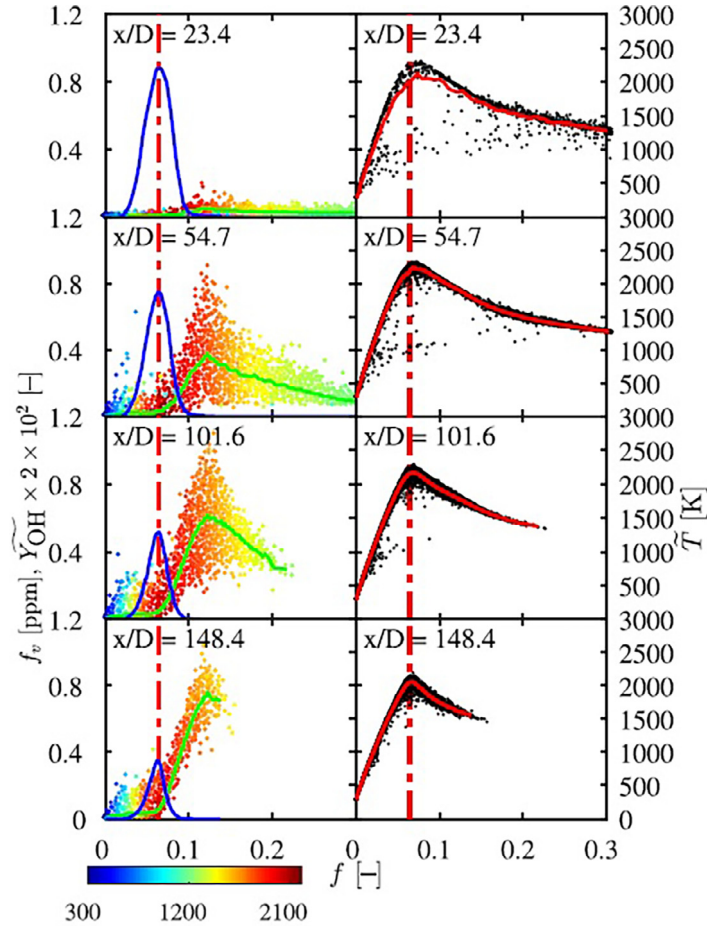


**Fig. 1.** Scatter plots of soot volume fraction,  $f_s$ , coloured by particle  $T$  (considered at the gas temperature) (left) and  $T$  (right) along with conditional means of  $f_s$  (green line), OH mass fraction (left) (black line) and  $T$  (right) (red line) at different axial locations. The vertical line represents the stoichiometric mixture fraction  $Z_{st} = 0.064$ . Taken from Tian et al. [20] (with permission). (For interpretation of the references to colour in this figure legend, the reader is referred to the web version of this article.)

a very computationally efficient method. The mean in RANS or filtered quantities in LES are then obtained from convolution of the state relationships with a presumed PDF or FDF, respectively. As discussed previously, the PAH and soot chemistry is slow and cannot be accurately parameterized by  $Z$  and  $\chi$  (or  $C$ ). As a result, specific transport equations are solved for these quantities [65,131,133,135,136]. The main modelling issue is then related to the closure of the production rates in these transport equations. In particular, this requires the formulation of a joint-presumed PDF of  $\phi_g = \{Z, \chi \text{ or } C, X_R\}$  and  $\phi_s$ . In the RANS context, Brookes and Moss proposed to express the joint PDF in Eqs. 33 by assuming the statistical independence of the variables [65]. In their simulations of methane jet non-premixed flames at 1 and 3 atm, the scalar dissipation rate was fixed to a single value. They assumed further that the marginal PDF of  $X_R$ , and  $\phi_s$  is  $\delta$ -Dirac functions whereas that of  $Z$  follows a  $\beta$  distribution:

$$\tilde{P} = \beta(Z)\delta(X_R - \tilde{X}_R)\delta(\phi_s - \tilde{\phi}_s) \quad (35)$$

This “uncorrelated” formulation was found to underestimate significantly the measured soot volume fraction. They attributed the discrepancies to a strong overestimation of the soot oxidation. The origin of this overestimation was explained by Kronenburg et al. [137] and can be understood by considering Fig. 1 which represents the scatter plots of soot volume fraction and temperature along with conditional means of soot volume fraction, OH mass fraction and temperature. These results were predicted by Tian et al. [20] with a RANS/transported PDF simulation of the Sandia flame [138]. This figure shows that, owing to fast oxidation,

there is little overlap between oxidizer species and soot profiles in mixture fraction space which suggests limited coexistence of oxidizer and soot. Therefore, soot quantities are strongly correlated with oxidative species. As a result, it can be stated that soot is correlated with the mixture fraction only in the oxidation region, but not in other regions. Clearly, the correlation between soot and mixture fraction in the soot oxidation region cannot be captured by Eq. (35). Brookes and Moss obtained a much better agreement with experimental data with an *ad hoc* revised formulation taking into account the correlation between mixture fraction and soot mass fraction [65]. On the other hand, it should be pointed out that the unsteady flamelet model does not suffer from this drawback as it takes into account the correlation between mixture fraction and soot quantities by solving the transport equation for soot quantities in the mixture fraction space [139].

Flamelet presumed FDF approaches were also developed in the context of LES [131,133,140]. The joint presumed FDF was re-expressed as  $\hat{P}(\phi_g, \phi_s) = \hat{P}(\phi_s|\phi_g)\hat{P}(\phi_g)$ . A first modelling strategy assumed that the conditional FDF can simply be modelled as the marginal FDF of the soot scalars since PAH and soot chemistry is characterized by long time scales compared to the main heat-releasing chemistry described by  $\phi_g$  [140]. The marginal FDF of soot quantities was designed to account for the very high spatial intermittency by introducing a sooting and a non-sooting mode [140]:

$$\hat{P}(\phi_s|\phi_g) = \omega\delta(\phi_s) + (1 - \omega)\delta(\phi_s - \phi_s^*) \quad (36)$$

However, Eq. (36) neglects the correlation between mixture fraction and soot quantities which leads to an overestimation of soot oxidation as discussed previously (see also Ref. [133] for a detailed analysis). In order to limit the overlap between soot quantities and oxidative species and improve the prediction of the soot oxidation rates, Yang et al. [133] updated Eq. (36) by introducing a threshold on mixture fraction:

$$\hat{P}(\phi_s|\phi_g) = [\omega\delta(\phi_s) + (1 - \omega)\delta(\phi_s - \phi_s^*)]H(Z - Z_s) \quad (37)$$

Yang et al. [133] determined  $Z_s$  as the location in the mixture fraction space where soot oxidation becomes faster than surface growth. Nmira et al. [134] used a different definition for  $Z_s$  in their simulations of buoyant ethylene diffusion flames under normal and reduced oxygen concentrations, assuming that it corresponds to the location where soot ceases to be produced. In both studies, this new subgrid-scale soot production model was found to improve the predictions as compared to Eq. (36). Berger et al. [141] have further updated Eq. (37) by introducing a log-normal distribution to model the sooting mode instead of a  $\delta$ -Dirac function. This modification was assessed in an a priori analysis based on DNS data and was found to improve model predictions for the coagulation source term.

PAH chemistry, as that of soot, does not adjust quickly to change in the turbulent flow field and, consequently, the PAH mass fractions cannot be accurately described by steady flamelet equations. To model the unsteady effects, Mueller and Pitsch [131] developed a spatially filtered transport equation for a lumped PAH mass fraction, similar to that developed for NO [142]. The molecular diffusivity of the lumped PAH is assumed to be that of the PAH with the larger mass fraction when the lumped PAH is composed of PAHs of different size. The lumped PAH reaction rates are modelled as:

$$\begin{aligned} \langle \dot{\omega}_{PAH} \rangle_{\Delta} &= \langle \dot{\omega}_+ \rangle_{\Delta} + \left\langle \left( \frac{\dot{\omega}_-}{Y_{PAH}} \right) Y_{PAH} \right\rangle_{\Delta} + \left\langle \left( \frac{\dot{\omega}_D}{Y_{PAH}^2} \right) Y_{PAH}^2 \right\rangle_{\Delta} \\ &\approx \langle \dot{\omega}_+^{fl} \rangle_{\Delta} + \langle \dot{\omega}_-^{fl} \rangle_{\Delta} \left( \frac{\widehat{Y}_{PAH}}{\widehat{Y}_{PAH}^{fl}} \right) + \langle \dot{\omega}_D^{fl} \rangle_{\Delta} \left( \frac{\widehat{Y}_{PAH}}{\widehat{Y}_{PAH}^{fl}} \right)^2 \end{aligned} \quad (38)$$

where  $\dot{\omega}_+$ ,  $\dot{\omega}_-$  and  $\dot{\omega}_D$  represent the chemical production term, the chemical consumption term and the additional consumption term due to the dimerization process. The superscript *fl* indicates that these quantities are extracted from the flamelet library. The method assumes that the chemical production rate,  $\dot{\omega}_+$ , as well as the terms in parenthesis on the right hand side of the first line are in steady state and can then be directly taken from the flamelet library. As discussed by Xuan and Blanquart [143], large PAHs are formed from smaller aromatic species, which themselves exhibit substantial transient effects. As a result, the assumption of steady state for  $\dot{\omega}_+$  is questionable. They proposed another strategy for the transport of PAH. It consists in solving a separate transport equations for benzene,  $A_1$ , and every PAH species considered to nucleate soot, denoted to as  $A_n$  hereafter. The benzene production rate is assumed to be in steady state whereas for the other transported PAH the relaxation scheme given by Eq. (38) is revised to account for the unsteadiness of the production term:

$$\langle \dot{\omega}_{A_1} \rangle_{\Delta} = \langle \dot{\omega}_{A_1}^{fl} \rangle_{\Delta} \quad (39)$$

$$\langle \dot{\omega}_{A_n} \rangle_{\Delta} = \langle \dot{\omega}_{A_n,+}^{fl} \rangle_{\Delta} \left( \frac{\widehat{Y}_{A_{n-1}}}{\widehat{Y}_{A_{n-1}}^{fl}} \right) + \langle \dot{\omega}_{A_n,-}^{fl} \rangle_{\Delta} \left( \frac{\widehat{Y}_{A_n}}{\widehat{Y}_{A_n}^{fl}} \right) + \langle \dot{\omega}_{A_n,D}^{fl} \rangle_{\Delta} \left( \frac{\widehat{Y}_{A_n}}{\widehat{Y}_{A_n}^{fl}} \right)^2 \quad (40)$$

This PAH modelling strategy was first applied to LES of ethylene flames by considering naphthalene as soot precursor [144]. It was

later extended to consider 6 PAHs ranging from naphthalene to cyclopenta[cd]pyrene in two turbulent non-premixed sooting jet flames using ethylene and JP-8 surrogate as fuels [136].

*Transported PDF and hybrid flamelet/transported PDF methods* These methods give direct access to the joint PDF or FDF and provide an exact closure of the soot formation and oxidation terms. Full transported PDF methods include species mass fraction, enthalpy and soot quantities as composition variables [19,20,145–147] and can be applied to all combustion regimes [148]. The set of gas-phase related variables is reduced to  $Z$ ,  $\chi$  or  $C$ , and  $X_R$  in hybrid flamelet/transported PDF methods in conjunction with tabulated chemistry [75,135,149,150]. However, the resulting significant gain in computational efficiency is accompanied by a loss of generality. The trade-off for avoiding the closure problem of the source terms is that the micro-mixing due to molecular diffusion, both for soot and for the gas-phase species, becomes an unclosed term that requires modelling. Soot differential diffusion was found to influence the solutions due to the low diffusivity of soot particles [20] and this process was mainly taken into account by neglecting soot diffusion [20,75,150]. Recent DNS analysis confirmed the relevance of this modelling option [151]. This study also showed that differential diffusion of gaseous species should be considered to achieve accurate predictions [151]. The PDF transport equation was solved by stochastic methods including Lagrangian particle methods [19,135,145,146,149] or Stochastic Eulerian Field [75,150]. It should be pointed out that stochastic Lagrangian particle methods in RANS provide realizations of the turbulent flow and should be able to capture soot intermittency. However, to the authors' best knowledge this point was never discussed in the literature.

*Conditional moment closure (CMC)* The CMC was used in both RANS [137,152] and LES [132]. Transport equations were solved for the conditional mean of gas phase and soot related quantities,  $\langle \phi_g|Z \rangle$  and  $\langle \phi_s|Z \rangle$ , respectively, and the unconditional means are obtained by integrating over a PDF of mixture fraction assuming a presumed  $\beta$  PDF [132,137,152]:

$$\langle \phi_g \rangle = \int_0^1 \langle \phi_g|Z \rangle \beta(Z) dZ \quad \text{and} \quad \langle \phi_s \rangle = \int_0^1 \langle \phi_s|Z \rangle \beta(Z) dZ \quad (41)$$

The conditionally averaged soot production source terms were solved by applying a first order CMC closure [132,137,152]:

$$\langle \dot{\omega}_s(\phi_g, \phi_s)|Z \rangle \approx \dot{\omega}_s(\langle \phi_g|Z \rangle, \langle \phi_s|Z \rangle) \quad (42)$$

This approximation lies on the assumption that fluctuations around the conditional mean are relatively small. Figure 1 shows that conditional fluctuations of soot mass fraction are large. It is then questionable if first order CMC closures for the soot model are appropriate or if second order CMC should be then preferred [132]. Soot volume fraction predictions in RANS/CMC [137,152] showed that a significantly better accordance with data when soot differential diffusion was accounted for. Similar conclusions were drawn in LES/CMC of a methane non-premixed jet flame where soot distributions were found to be much more intermittent and the predicted values were closer to experimental data when soot differential diffusion was considered [132].

#### 2.4. New trends in modelling soot formation

This section aims to review recent works that apply machine learning (ML) in the modelling of soot production. These works follow a rapidly growing trend in the simulation of reactive flows that resort to ML methods to reduce both computing cost and memory requirements [185].

Dworkin and co-workers proposed a soot concentration estimator [186–189]. The main idea behind the method is to estimate the soot volume fraction from time-integrated histories along pathlines

of certain physical and chemical quantities affecting  $f_s$ , such as temperature and species concentration (denoted as  $X_h$  in generic form hereafter) [186,187]:

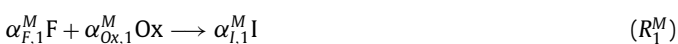
$$f_s(t) = f(X_h(t)) \quad \text{with} \quad X_h = \int_{\text{pathline}} X(t) dt \quad (43)$$

Such relationship can be derived from numerical results of some target laminar coflow diffusion flames using detailed gas-phase chemistry and soot models and then applied to estimate soot volume fraction in other flames while avoiding the complexity and the high-computational resources and cost required by detailed soot modelling. To reduce the memory requirements and computational costs associated with Eq. (43), Jadidi et al. [188] proposed first a supervised Artificial Neural Network (ANN) technique with eight input parameters, namely temperature history ( $T_h$ ), mixture fraction history ( $Z_h$ ), and mass fraction histories of oxygen ( $O_{2,h}$ ), carbon monoxide ( $CO_h$ ), carbon dioxide ( $CO_{2,h}$ ), hydrogen ( $H_{2,h}$ ), hydroxide ( $OH_h$ ), and acetylene ( $C_2H_{2,h}$ ), and the soot volume fraction as output from the ANN. The ANN was build to model soot concentration fields in laminar axisymmetric coflow ethylene diffusion flames. It was trained over eight different flames and validated by considering two other flames. The average and maximum relative errors over the eight flames used for the training were found to be 21.48% and 39.92% for the peak soot volume fraction and 8.08% and 31.64% for the integrated soot volume fraction, respectively. For the two other flames, the relative errors were 19.64% and 52.79 % for the peak soot volume fraction and 4.66% and 63.43% for the integrated soot volume fraction. In a second article [189], they developed a long short-term memory (LSTM) neural network, with six input variables ( $T_h$ ,  $H_{2,h}$ ,  $C_2H_{4,h}$ ,  $O_{2,h}$ ,  $OH_h$ , and  $C_2H_{2,h}$ ) to estimate the soot volume fraction in a time-varying laminar ethylene/air coflow diffusion flame.

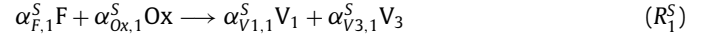
Di Liddo et al. [190] developed a Polycyclic Aromatic Compounds (PAC)-based ML soot nucleation model with the following procedure. CoFlame [31] was used to provide temperature and the concentrations of small key gaseous species to the SNapS2 code [191]. The SNapS2 code simulated PAH growth and provided PAC molecular properties and their temporal rates of change to the ML module that returns the soot inception rate. This method was trained by using experimentally-derived soot inception rates from three atmospheric pressure laminar premixed ethylene/air flames and its predictions were found to outperform, on one hand, the predictions of CoFlame and, on the other hand, the predictions of a ML model which used only the input data from CoFlame (temperature and small species concentrations). The authors concluded then that detailed PAC properties are important to be considered in soot inception modelling.

Seltz et al. [192] trained a combination of ANNs and convolution neural networks (CNNs) from a hybrid stochastic-fixed sectional approach to solve for the PBE. The inputs of the ANN were the thermochemical parameters controlling the soot kinetics and the increment in time whereas the input of the CNN was the shape of the particle size distribution (PSD) discretized into sections. The output of the network was the PSD shape for the subsequent time step or a source term for the Eulerian transport of the PSD.

The concept of virtual chemistry has recently emerged in the literature and consists of virtual species and reactions whose thermo-chemical properties are optimized by ML algorithms [193]. The range of application of the virtual mechanism is dictated by the operating conditions and flame configurations covered in the learning database [194]. Maldonado Colmán et al. proposed a virtual chemistry model for soot production in ethylene/air flames [195,196]. The virtual chemistry model was composed of a main mechanism to capture heat release and temperature [195]:



and a sub mechanism to model soot production:



where F, Ox, I,  $P_k$ ,  $V_1$ ,  $V_2$  and  $V_3$  correspond to the fuel, oxidizer and virtual species, respectively. The virtual species S corresponds to soot and  $R_1^S$ ,  $R_2^S$  and  $R_4^S$  represent the nucleation, surface growth and coagulation, and oxidation of soot particles. The virtual main and soot mechanisms were optimized to target an ensemble of reference flame solutions computed using the detailed CRECK mechanism [197]. The main mechanism was optimized with a learning database consisting of 26 premixed flames with equivalence ratios ranging from 0.5 to 3 whereas the soot sub-mechanism was optimized on a different database consisting of 11 premixed flames with equivalence ratios ranging from 1.8 to 2.8 and 6 non-premixed flames of strain rates ranging from 6 to 90  $s^{-1}$ . The virtual soot chemistry was found to reproduce with fidelity the soot volume fraction computed by detailed chemistry simulations in both premixed and non-premixed laminar flames [195] and was applied to simulate an ethylene/air non-premixed turbulent flame [196].

### 3. Radiation modelling in flames

#### 3.1. Background

The spectral radiative transfer equation (RTE) is written as Modest and Mazumder [22], Modest and Haworth [23]:

$$\begin{aligned} \mathbf{s} \cdot \nabla I_\eta(\mathbf{r}, \mathbf{s}) + (\kappa_\eta + \sigma_\eta) I_\eta(\mathbf{r}, \mathbf{s}) \\ = \kappa_\eta I_{b,\eta}(T) + \frac{\sigma_\eta}{4\pi} \int_{4\pi} \Phi(\mathbf{s}, \mathbf{s}') I_\eta(\mathbf{r}, \mathbf{s}') d\Omega' \end{aligned} \quad (44)$$

where  $I_\eta(\mathbf{r}, \mathbf{s})$  represents the radiative intensity at wavenumber  $\eta$  along the direction of travel  $\mathbf{s}$ .  $I_{b,\eta}$  is the blackbody intensity.  $\kappa_\eta$ ,  $\sigma_\eta$  and  $\Phi$  are the radiative properties of the medium, namely the absorption coefficient, the scattering coefficient and the scattering phase function. Eq. (44) is subjected to the following boundary conditions at a wall:

$$I_{w,\eta} = \epsilon_w I_{b,\eta}(T_w) + \frac{1 - \epsilon_w}{\pi} \int_{\mathbf{n} \cdot \mathbf{s} < 0} I_\eta |\mathbf{n} \cdot \mathbf{s}| d\Omega \quad (45)$$

where  $\epsilon_w$  and  $\mathbf{n}$  are the wall emissivity and the unit surface normal pointing away from surface into the medium, respectively.

The radiative source term,  $S_R = -\nabla \cdot \mathbf{q}_R''$ , that appears in the energy equation, is then expressed as:

$$S_R = \int_{\eta=0}^{\infty} \kappa_\eta \int_{4\pi} I_\eta d\Omega d\eta - 4\pi \kappa_p I_b(T) \quad (46)$$

where  $\kappa_p = \int_{\eta} \kappa_\eta I_{b,\eta}(T) d\eta / I_b(T)$  is the Planck-mean absorption coefficient. The first term on the right hand side of Eq. (46) represents the absorption term, while the second term is the emission term. Radiative heat transfer interacts with combustion soot formation through the radiative source term in the energy conservation equation.

The solution of a radiative transfer problem in turbulent flames consists of the following three tasks:

- *Resolution of the RTE.* The spectral RTE is a six-variable (three spatial,  $\mathbf{r}$ , two angular,  $\mathbf{s}$ , and one spectral,  $\eta$ ) integro-differential equation and its solution requires a specific solver [22].
- *The determination of radiative properties.* In absence of particles other than soot (droplets, coal, char, ash,...), the main contributors to radiative heat transfer are the radiating gaseous combustion products ( $\text{CO}_2$ ,  $\text{H}_2\text{O}$ ,  $\text{CO}$ , hydrocarbon fuels) and soot particles. The resolution of Eq. (44) requires then first a detailed knowledge of  $\kappa_\eta$ ,  $\sigma_\eta$ , and  $\Phi$  in gas/soot mixtures.
- *Turbulence-radiation interaction.* The absorption,  $\kappa_\eta I_\eta$ , and emission,  $\kappa_\eta I_{b,\eta}$ , terms are highly non-linear. A consequence is that, similar to the chemical source terms, the mean (in RANS) and the filtered (in LES) absorption and emission terms cannot be expressed simply in terms of the mean or filtered properties [21–24].

In laminar flames, the last issue is absent. With the exception of optically thin flames, all the three tasks have a strong influence on the overall accuracy of RHT modelling.

### 3.2. Radiative transfer equation solver

Various RTE solution methods have been developed in the last several decades with different accuracy, computational efficiency, and for different applications. The most commonly used RTE solution methods include the Monte Carlo (MC), the spherical harmonics ( $P_N$ ), discrete-ordinates (DOM), and finite volume (FVM). These methods have been discussed in detail in textbooks and review papers [21,22] and will not be repeated here. This section will discuss briefly the methods often used in the simulations of laminar and turbulent sooting flames.

In modelling radiative heat transfer in laminar flames of gaseous and vaporized liquid fuels where radiation scattering is negligible, the DOM and FVM have been preferred due to their good accuracy and computational efficiency [198]. The details of DOM/FVM in Cartesian coordinates are provided in Ref. [22] and can be found in Refs. [198,199] (for DOM) and Ref. [200] (for FVM) in axisymmetric cylindrical coordinates. The DOM has been extensively used in numerical studies of laminar coflow diffusion flames, such as those using the CoFlame code [31] or its variants [16,41,43,88,94,117,201–203] and also in Refs. [61,62,98,108]. On the other hand, the FVM method has been used by Consalvi and co-workers in modelling both laminar [17] and turbulent diffusion flames [75,204,205]. The Monte Carlo method [21,22] is generally recognized as the most powerful technique to solve radiative transfer problems, allowing the simulation of problems in complex geometries, bounded by surfaces with directionally and spectrally dependent radiative properties, and containing non-gray emitting, absorbing and anisotropically scattering media. The solutions obtained by the MC method are generally considered as a reference, and used for benchmark purposes. Nevertheless, applications of MC methods in coupled flow/combustion/soot/radiation simulations of turbulent flames were reported in the literature [145,167,170,181,206] with an increasing trend over the recent years. These MC simulations have benefited from improved computational efficiency with the development of the Photon Monte Carlo (PMC) method [207] or the quasi-MC methods [208,209]. Pal et al. [169] have conducted a comprehensive comparison study of the accuracy and computational efficiency of the  $P_1$ ,  $P_3$  and FVM with  $16 \times 4$  control angles coupled to different radiative property models in RANS simulations of the Sandia flame D and two other optically thicker flames designed from the Sandia flame D by scaling up the burner diameter by a factor of 4 with or without soot. The results of  $P_1$ ,  $P_3$ , and DOM/FVM methods were compared to the benchmark solution obtained by a stochastic

PMC solver coupled with the line-by-line (LBL) model for radiative properties [207]. They found that all three RTE solvers have similar accuracy for the optically-thin Sandia flame D. For the optically thicker flames, the  $P_3$  and FVM were found to provide predictions comparable with those of the PMC with the  $P_3$  being significantly more computationally efficient.

### 3.3. Radiative property modelling of sooting flames

#### 3.3.1. Radiative properties of sooting flames

The radiatively participating species in sooting flames are, on the one hand, the gaseous radiating combustion products, including carbon dioxide, water vapour, carbon monoxide and the hydrocarbon fuels and intermediates and, on the other hand, the soot particles. The radiative contribution of hydrocarbon fuels and intermediates is commonly neglected. However, it may play a significant role in some specific configurations such as pool fires where fuel vapour affects noticeably the radiative feedback toward the condensed fuel surface [210–212].

The spectral absorption coefficient of radiating gases in the infrared is characterized by millions of discrete spectral lines that form the vibration–rotation bands. These lines result from the quantum nature of the vibrational and/or rotational energies of gas molecules [22]. Each spectral line is characterized by its spectral location,  $\eta_i$ , its line strength,  $S_i$ , and a line profile,  $F_i(\eta - \eta_i)$ , which accounts for line broadening [21,22]. The Lorentz line profile is a reasonable approximation for most of the combustion applications. These line parameters have been compiled in high-resolution spectroscopic databases [213,214]. In particular, HITEMP 2010 [214], developed specifically for high temperatures representative of combustion systems, contains the locations, strengths, and widths of spectral lines of  $\text{CO}_2$ ,  $\text{H}_2\text{O}$ ,  $\text{CO}$  and  $\text{CH}_4$  up to 4000 K. The absorption coefficient of a radiating gas at a given wavenumber  $\eta$  is the sum of the contributions of all the spectral lines:

$$\kappa_{\eta,g} = N \sum_{\text{lines}} S_i(T) F_i(\eta - \eta_i) \quad (47)$$

where  $N$ ,  $S_i$  and  $F$  are the molecule number density of the radiating species under consideration, the line intensity of the  $i$ th transition line and the line shape profile, respectively.

Increasing temperature has a strong influence on gas spectra with the appearance of the so called “hot lines”. These lines are imperceptible at ambient temperature but become of increasing importance as the temperature increases. As such, temperature affects strongly the number of lines to be considered for accurate predictions of radiative heat transfer (RHT) [215]. Pressure also affects gas radiation through, on one hand, the increase in gas density ( $N$  in Eq. (47)) and, on the other hand, the broadening of spectral lines with increasing pressure [216,217]. Numerical simulations showed that the first mechanism is predominant in combustion applications whereas the second one has a much weaker influence on gas radiation heat transfer [216,217]. RHT calculations at the resolution of a spectral line are called line-by-line (LBL) calculations and require a spectral resolution of the order of  $0.01 \text{ cm}^{-1}$ , leading to solve more than  $10^6$  RTEs to cover the entire thermal radiation spectrum.

Contrary to radiating gases, soot particles emit and absorb continuously over the entire spectrum, from ultraviolet to infrared. Absorption and scattering of soot particles is characterized by small size parameters ( $x = \pi D_s/\lambda \ll 1$  where  $D_s$  and  $\lambda = 1/\eta$  represent a characteristic soot primary particle size and wavelength, respectively) over the spectral region of interest to RHT in combustion applications. A consequence is that the Rayleigh theory can be applied to calculate the absorption cross section of soot particles based on primary particle size, since the aggregate structure of soot particles has no influence on the particle total absorp-

tion cross section based on the Rayleigh-Debye-Gans (RDG) theory for fractal aggregates [218]. In addition, the scattering contribution is usually neglected in Eq. (44). The assumption of negligible scattering for RHT calculations is supported by simulations involving more sophisticated soot radiative property models such as the RDG theory for fractal aggregates (RDG-FA) or the integral equation formulation for scattering (IEFS) [206,219,220]. Although soot scattering becomes important in the visible and UV spectra, these spectral regions have only a marginal contribution to the spectrally-integrated radiative source term and radiative heat fluxes [220] and therefore can be neglected. The soot absorption coefficient is then expressed as Modest and Mazumder [22]:

$$\kappa_{\lambda,s} = -\text{Im} \left[ \frac{m^2 - 1}{m^2 + 2} \right] \frac{6\pi f_s}{\lambda} = \frac{36\pi nk}{(n^2 - k^2 + 2)^2 + 4n^2k^2} \frac{f_s}{\lambda} \quad (48)$$

where  $\text{Im}(x)$  denotes the imaginary part of a complex function  $x$  and  $m = n + ki$  is the soot complex refractive index. It is convenient to re-write Eq. (48) as

$$\kappa_{\lambda,s} = E(m) \frac{6\pi f_s}{\lambda}, \quad E(m) = -\text{Im} \left[ \frac{m^2 - 1}{m^2 + 2} \right] \quad (49)$$

where  $E(m)$  has often been termed soot absorption function and has a nearly constant value of about 0.35 in the visible and near infrared spectral regions for mature soot [221]. It is worth pointing out that the knowledge of soot refractive index in the near to mid infrared spectral region is of great importance to the accuracy of RHT modelling in sooting flames. Unfortunately, it is subject to uncertainties due to the dependence of soot maturity and internal nanostructure on fuel and flame conditions as characterized by H/C ratio, e.g., [222,223]. Nevertheless, there have been less efforts to determine the soot refractive index in the infrared relative to those in the visible spectrum. The most commonly used refractive index model for soot in prediction of RHT in sooting flames is that proposed by Chang and Charalampopoulos [224] given as

$$n = 1.811 + 0.1263 \ln \lambda + 0.027 (\ln \lambda)^2 + 0.0417 (\ln \lambda)^3 \quad (50)$$

$$k = 0.5821 + 0.1213 \ln \lambda + 0.2309 (\ln \lambda)^2 - 0.01 (\ln \lambda)^3 \quad (51)$$

where the wavelength  $\lambda$  is in  $\mu\text{m}$  and the model is applicable for  $0.4 \leq \lambda \leq 30 \mu\text{m}$ . It is worth pointing out that the  $E(m)$  value of soot refractive index of Chang and Charalampopoulos displays a fairly gradual variation with wavelength in the spectral region of 1 to 15  $\mu\text{m}$  with an average value of  $E(m) = 0.233$ : it first increases nearly linearly from 0.219 at 1  $\mu\text{m}$  to 0.285 at 4  $\mu\text{m}$  and then decreases nearly linearly to 0.168 at 15  $\mu\text{m}$ .

LBL calculations have to solve more than one million RTEs, making this method prohibitive in modelling flames, especially in multidimensions. However, the LBL method has often been used to provide reference solutions in decoupled radiation calculations, where the concentrations and temperature of radiating species (including soot) are prescribed, for evaluation of approximate radiative property models [225–229]. On the other hand, Modest and co-workers proposed the PMC-LBL radiation model. This model is based on the fact that the random-number relation for the emission wavenumber will favor the wavenumbers with substantial emission, requiring then fewer wavenumbers to achieve accuracy comparable to the one obtained from standard LBL spectral integration. This method was found to be applicable in fully coupled flow/combustion/soot/radiation simulations of statistically stationary turbulent non-premixed sooting flames in the contexts of RANS [145,169], LES [167] and DNS [181]. However, such computations remain too computationally demanding for engineering calculations and approximate models have to be considered.

### 3.3.2. Approximate models

Approximate gas radiative property models can be classified based on their spectral resolution. The narrow band models include the traditional Statistical Narrow Band and Narrow Band Correlated-k [230]. These models, and also their degraded versions such as the Wide Band Correlated-k (WBCK) [231], are very accurate and were applied to the simulations of both laminar and turbulent sooting flames in conjunction with state-of-the-art combustion and soot production models [31,75,150,170]. However, they are also probably too computationally-demanding to be applied in broader coupled flow/ combustion/ soot/ radiation simulations. As a consequence, this brief literature review is limited to the gas radiative property models readily implementable and applicable for state-of-the-art modelling of sooting flames and the readers interested in the above-mentioned narrow-band models can refer to radiative heat transfer text books [22]. Accordingly, the following discussion focuses mainly on the simplest radiation model, i.e., OTA, and global radiative property models, such as the weighted-sum-of-gray-gases model (WSGG) [232], the spectral-line weighted-sum-of-gray-gases models (SLW) [233–235] and full-spectrum  $k$ -distribution models (FSK) [236].

*The optically-thin approximation (OTA)* The optical thickness, defined as  $\tau = \int_0^L \kappa ds$ , measures the ratio between a characteristic length scale of the medium,  $L$ , and the distance travelled by a photon before being absorbed. If  $\tau \ll 1$  absorption is negligible and Eq. (46) reduces then to the emission term only that can be easily computed from the Planck-mean absorption coefficients of radiating gas and soot and the local temperature. This approximation, referred to as OTA, is attractive as it avoids the complications related to the resolution of the spectral RTE (Eq. (44)). However, its validity is limited to small-scale 1D and non-smoking axisymmetric laminar coflow diffusion flames at atmospheric pressure and normal gravity [21]. Although OTA has often been used to simplify RHT calculations in numerical studies of laminar diffusion flames where detailed gas-phase chemistry was employed [237] and even with sophisticated soot kinetic models [12,14,77,238], several numerical studies showed that it becomes questionable for laminar coflow diffusion flames at the smoke-point limit [43], for high-pressure laminar hydrogen diffusion flames [239] and microgravity laminar diffusion flames [240,241]. In addition, radiation absorption can also become important in laminar coflow diffusion flames and turbulent jet diffusion flames at elevated pressures and/or under oxy-fuel flame conditions due to significantly higher soot loading or higher  $\text{CO}_2$  concentrations. Research of laminar diffusion flames under these non-conventional conditions is necessary to examine the validity range of gas-phase reaction mechanisms and soot formation models. The consequences of using OTA in modelling laminar diffusion flames will be further discussed in Section 3.4.

On the other hand, Table 7 shows that the OTA was widely applied to the simulations of lab-scale sooting turbulent non-premixed jet flames in both RANS and LES frameworks to reduce the computational cost on RHT and thus allow the implementation of state-of-the-art combustion and soot production models. The spectral radiative structure of these flames was analyzed in details [162,170], showing that: (i) soot and gas radiations weakly interact with a very small part of gas radiation absorbed by soot and vice versa, (ii) gas radiation self-absorption is significant. It represents for example more than 50% in the ethylene non-premixed turbulent flame investigated experimentally at SANDIA [170], (iii) soot self-absorption is typically less than 10%. These results suggest that the OTA (and also the gray approximation) may be reasonably applicable for soot radiation but is highly inaccurate for gas radiation that is usually dominant in these flames. These latter conclusions were also found to hold for lab-scale methane non-premixed flames up to 4 atm [242]. Nevertheless, it is important to draw at-

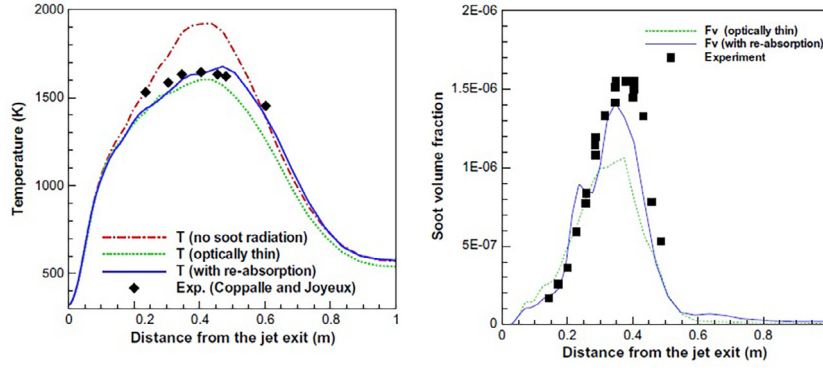


Fig. 2. Axial evolution of the temperature and soot volume fraction. Adapted from Mehta et al. [145] (with permission).

tention that the OTA or gray approximation for soot radiation becomes hardly justifiable in larger sooting flames representative of industrial or fire safety applications, where soot self-absorption can reach as high as 75% as observed by Mehta et al. [162] while simulating a large-scale ethylene turbulent non-premixed jet flame. The radiating shielding observed in large-scale pool fires due to cold soot escaping the flame is another example of the growing importance of soot self-absorption with the flame size [243].

More specifically, the discrepancies introduced by the OTA in lab-scale sooting non-premixed turbulent flames were quantified, showing underestimation and overestimation of the mean and fluctuating temperature, respectively [75,170]. In addition, the peaks of mean and fluctuating soot volume fraction were found to be substantially underestimated [75,145,170]. These differences are illustrated in Fig. 2 adapted from Ref. [145]. The simulations of the ethylene turbulent non-premixed flame investigated by Coppalle and Joyeux [157] were performed in the RANS context. The transported PDF method was used to model turbulence/chemistry interaction with a systematically reduced 33-species reaction mechanism containing 205 elementary reactions. The soot kinetics was based on acetylene as precursor for nucleation and the HACA as surface growth/oxidation mechanism. Soot dynamics was modelled by a univariate method of moments with interpolative closure and 6 moments were considered. The RTE was solved by the PMC-LBL. Figure 2 shows that the peak soot volume fraction is underestimated by about 50% when the OTA is applied. The OTA tends to overestimate the radiative loss and then to underpredict the temperature. In these coupled simulations, these effects are somewhat compensated by the reduction in soot emission, which explains the rather limited discrepancies on temperature.

**Weighted-sum-of-gray-gases** The WSGG model is probably the most popular global gas radiation model for combustion simulations due to its simplicity and ease of implementation. The WSGG model consists in assuming that the total emissivity along an homogeneous path,  $\epsilon(T, L) = \int_0^\infty (1 - e^{-\kappa_\eta L}) I_{b,\eta}(T) d\eta / I_b(T)$ , can be approximated by a weighted sum of  $N$  gray gases, with  $N$  being typically about 3 and 4 [22]:

$$\epsilon(T, L) = \sum_{i=0}^N a_i(T) [1 - e^{-k_i L}] \quad \text{with} \quad \sum_{i=0}^N a_i(T) = 1 \quad (52)$$

$i = 0$  corresponds to the transparent window (clear gas) with an associated gray gas absorption coefficient of  $k_0 = 0$ . The WSGG parameters, namely  $k_i$  and  $a_i(T)$ , are obtained by fitting the total emissivity over a wide range of path-length,  $L$ , and temperature,  $T$ , and usually a constant molar ratio of  $H_2O$  and  $CO_2$  is assumed although approaches to accommodate varying molar ratios were reported in the literature [244,245]. The WSGG RTE and the total ra-

diative intensity,  $I$ , can be expressed as:

$$\frac{dI_i}{ds} = k_i a_i(T) I_b(T) - k_i I_i; \quad i = 0, N \quad \text{and} \quad I = \sum_{i=0}^N I_i \quad (53)$$

The more recent WSGG model parameters were obtained by using HITEMP 2010 to conduct LBL calculations of the target emissivities for the fitting process and these versions were found to provide reasonably accurate engineering predictions for situations representative of combustion applications [244,246]. However, the reader has to keep in mind that the WSGG suffers from inherent limitations due to its formulation. The first limitation is that the gray-gas absorption coefficients do not depend on temperature. The second limitation is related to the difficulty to handle the addition of a third non-gray radiating species without significantly complicating the model or introducing loss in its computational efficiency. Two approaches were mainly proposed to include soot [247]. In the first, soot is considered as gray and the soot Planck-mean absorption coefficient,  $\kappa_{p,s}$ , is then added to the absorption coefficient of each gray gas,  $k_i$ . However, it should be kept in mind that, as discussed previously, the gray assumption for soot is expected to result in a loss of accuracy in large-scale or highly sooting combustion systems. In the second approach, the WSGG parameters for non-gray soot ( $k_{s,i_s}$  and  $a_{s,i_s}$ ,  $i_s = 1, N_s$ ) are derived independently and a superimposition scheme is used to obtain the absorption coefficient,  $k_i$ , and the weight function,  $a_i$ , of the gas/soot mixture [226]:

$$k_i = k_{g,i_g} + k_{s,i_s}; \quad 0 \leq i_g \leq N_g; \quad 1 \leq i_s \leq N_s \quad (54)$$

$$a_i = a_{g,i_g} \times a_{s,i_s}; \quad 0 \leq i_g \leq N_g; \quad 1 \leq i_s \leq N_s \quad (55)$$

where  $N_g$  and  $N_s$  are the number of gray gases for the gas mixture and soot, respectively. This approach results in a significant loss in simplicity and computational efficiency since the number of RTE to be solved increases drastically to reach to  $(1 + N_g) \times N_s$  [248].

**Global  $k$ -distribution based models** The spectral-line based weighted-sum-of-gray gases (SLW) and the full-spectrum  $k$ -distribution (FSK) models are closely related and based on the same concept of  $k$ -distribution [249]. Therefore, the discussion of the concepts and governing equations will be made from a FSK point of view for conciseness and a detailed presentation of the SLW can be found in Ref. [250]. The FSK methods introduce a Planck-function-weighted  $k$ -distribution,  $f(k, \phi, T_p)$ , and its cumulative,  $g(k, \phi, T_p) = \int_0^k f(k', \phi, T_p) dk'$  [236,251]:

$$f(k, \phi, T_p) = \frac{1}{I_b(T_p)} \int_0^\infty \delta[k - \kappa_\eta(\phi)] I_{b,\eta}(T_p) d\eta \quad (56)$$

$$g(k, \phi, T_p) = \frac{1}{I_b(T_p)} \int_0^\infty H[k - \kappa_\eta(\phi)] I_{b,\eta}(T_p) d\eta \quad (57)$$

where  $\delta$  and  $H$  are the delta-Dirac and Heaviside functions, respectively, and  $\phi = \{x_i, f_s, T, p\}$  is an array of thermophysical variables affecting the absorption coefficient.  $g$  represents the fraction of the spectrum-integrated Planck function with an absorption coefficient  $\kappa_\eta < k$ .  $g$  is a smooth and monotonically increasing function of  $k$  and its introduction for spectral integration instead of the wavenumber reduces drastically the number of integration points from about  $10^6$  in LBL calculation to about 10. In other words, the number of RTE in FSK/SLW methods to be solved is of about 10 as compared to  $10^6$  in LBL. The FSK RTE has a similar form as the WSGG RTE (Eq. (53)) [236,251]:

$$\frac{dI_{g_0}}{ds} = k^*(g_0)a(g_0)I_b(T) - k^*(g_0)I_{g_0} \quad \text{and} \quad I = \int_0^1 I_{g_0} dg_0 \quad (58)$$

where the subscript 0 refers to the reference state that can be defined, for example, by volume averaged species mole fractions and soot volume fraction and a blackbody emission-averaged temperature [22], though other definitions of the reference state were proposed [250,251].  $a(g_0)$  is computed as:

$$a(g_0) = \frac{\partial g(k_0, \phi_0, T)}{\partial g_0(k_0, \phi_0, T_0)} \quad (59)$$

The FSK/SLW methods provide solutions with the LBL accuracy for homogeneous and isothermal media. Their extension to inhomogeneous and/or non-isothermal media requires assuming that a functional (scaled) or statistical (correlated or comonotonic) relationship [250,252,253] exists between the spectral absorption coefficients at different thermophysical states, leading to the full-spectrum scaled  $k$ -distribution (FSSK) or the full spectrum correlated- $k$  distribution (FCCK) and the rank correlated full spectrum  $k$  distribution (RCFSK), respectively. Real gas spectra are neither truly scaled nor correlated and these assumptions introduce inevitably inaccuracy in these methods. As discussed in Ref [254], the scaled methods are still under development for multidimensional applications and are not recommended at this stage. On the other hand, several schemes were developed based on the correlated or comonotonic assumptions to determine  $k^*$  in Eq. (58). Among them, those that preserve emission, such the scheme proposed by Cai and Modest [255] or the RCFSK/RCSLW [256,257], generally give more accurate predictions [248,254]:

1. *The scheme of Cai and Modest* [255]. In this scheme,  $k^*$  is determined from the following three-step sequence: i) determine  $k_0$  from  $g(k_0, \phi_0, T_0) = g_0$  where  $g_0$  is a quadrature point, ii) interpolate the local value of  $g = g(k_0, \phi, T)$ , and iii) determine  $k^*$  from  $g(k^*, \phi, T) = g(k_0, \phi_0, T)$ .
2. *The RCFSK/RCSLW methods* [256,257].  $k^*$  is determined from  $g(k^*, \phi, T_p) = g_0$  and the stretching factor is determined as  $a(g_0) = \frac{\partial}{\partial g_0} g(k(g_0, \phi, T_p), \phi, T)$ .

In addition, it was demonstrated that the RCFSK/RCSLW solutions are almost insensitive to the choice of the Planck temperature,  $T_p$  [248,256,257].

The full-spectrum  $k-g$  distributions for gas/non-gray soot mixtures can be assembled directly from LBL data or from narrow-band  $k-g$  distributions of individual species following the methodology proposed by Modest and Riazzi [258]. In order to make the method applicable, these  $k-g$  distributions are stored in look-up tables for discrete values of pressure, mole fractions of the radiating gas,  $x_i$ , soot volume fraction,  $f_s$ , and gas and reference temperatures and interpolated during simulations [259–261]. A machine learning based full-spectrum correlated  $k$ -distribution model for inhomogeneous gas-soot mixtures was recently proposed, providing solutions as accurate as those obtained with look-up tables while reducing significantly the memory storage [262].

Both FSK and SLW methods do not suffer the deficiencies of the WSGG methods and provide generally better predictions within

few percent of LBL solutions in gas/soot mixtures [248,263]. These solutions are generally obtained with about ten quadrature points [248]. Recent conclusions obtained by Bagder et al. [264] in a propane flame under oxy-fuel combustion condition (in the absence of soot) suggest that accurate solutions can be obtained with only 3–5 gray gases when the RCSLW method is used. Nevertheless, this conclusion needs to be further confirmed in other combustion problems.

#### 3.4. Importance of thermal radiation in laminar diffusion flames

The effects of radiation on laminar flames have been discussed in several recent reviews [21,23,265]. Therefore, the discussion below will focus only on the effects of thermal radiation on the structure and soot formation of laminar diffusion flames and studies published in the last two decades. The importance of RHT and the relative importance of radiating gases and soot to RHT in laminar counterflow and coflow diffusion flames have been evaluated in a number of studies. It has been shown that thermal radiation can significantly affect both the overall and local properties of flames and the radiating gases and soot can have different influences on the flame properties due to their different spectral properties and spatial distributions in flame. The relevant studies conducted in the last two decades are summarized in Table 8.

Liu et al. [16] modelled a laminar coflow ethylene/air diffusion flame established on the Gülder burner (a slightly modified version of the Santoro laminar coflow diffusion flame burner) using an acetylene based two-equation semi-empirical soot model and GRI-Mech 3.0 reaction mechanism. The visible flame height and the peak soot volume fraction are about 64 mm and 8 ppm, respectively. To evaluate the importance of RHT and radiation absorption, the calculations were conducted using several different treatments of RHT: (1) no radiation, (2) OTA for thermal emissions from CO, CO<sub>2</sub>, H<sub>2</sub>O, and soot, (3) a full radiation model consisting of using DOM as the RTE solver coupled with a statistical narrow-band correlated- $k$  (SNBCK) based wide-band (WB) model for non-gray absorption coefficients of CO, CO<sub>2</sub>, H<sub>2</sub>O, and soot, (4) solving RTE without gas radiation (soot only), and (5) solving RTE without soot radiation (radiating gases only). The soot spectral absorption coefficient was assumed to be  $\kappa_{\lambda,s} = 5.5f_s/\lambda$ , which corresponds to a wavelength independent  $E(m)$  value of 0.292 and is consistent with the soot Planck mean absorption coefficient given in Modest and Mazumder [22]. The predicted temperature distributions using different radiation treatments are shown in Fig. 3 along with the measured temperature with the peak temperature in each case indicated. The underprediction of temperature in the centerline region, compare Fig. 3(c) and (b), was mainly attributed to the neglect of fuel preheating effect in the simulation. Although neglect of radiation absorption causes only about 5 K decrease in the peak temperature, it causes more than 50 K decrease in the centerline region around the flame tip around  $z = 6$  cm, which is mainly attributed to absorption by CO<sub>2</sub>. As shown in Fig. 4 below, the soot volume fractions in the flame centerline region are significantly underpredicted, which remains a challenge in soot formation modelling in laminar coflow diffusion flames using both semi-empirical and detailed soot models [16,94,98]. If the soot volume fractions in the centerline region were better predicted to levels comparable to measured values, the neglect of radiation absorption as in OTA would have led to an even greater decrease in temperatures in the centerline region. The importance of radiation absorption in laminar coflow diffusion flames should not be evaluated using the peak temperature, since the peak temperature occurs at the flame wing at the lower part of the flame around  $z = 2$  cm, where the high-temperature reaction zone is thin and emission dominated. The main effect of radiation absorption takes place in the flame centerline region where temperatures are relatively low and the

**Table 8**

Main sub-models used in numerical studies of the effects of thermal radiation on the structure and soot formation in laminar diffusion flames conducted in the last two decades. SNBCK denotes statistical narrow-band correlated-k, WB wide-band, SF soot formation, and SFO soot formation/oxidation.

Ref. and year	Flame	Gas-phase mech.	Soot model	RTE solver	Radiative prop. model	Pressure (atm)	Gravity (g)
Liu et al. [16]	Coflow C <sub>2</sub> H <sub>4</sub> diff. flame	GRI-Mech 3.0	A C <sub>2</sub> H <sub>2</sub> based 2-eq. model	DOM	- SNBCK based WB model - OTA - No radi.	1	1
Liu et al. [43]	Two coflow C <sub>2</sub> H <sub>4</sub> diff. flames	GRI-Mech 3.0	A C <sub>2</sub> H <sub>2</sub> based 2-eq. model	DOM	- SNBCK based WB model - OTA - No radi.	1	1
Liu et al. [55]	Counterflow SF C <sub>2</sub> H <sub>4</sub> diff. flames	GRI-Mech 3.0	A C <sub>2</sub> H <sub>2</sub> based 2-eq. model	DOM	- SNBCK based WB model - OTA - No radi.	1	1
Liu et al. [199]	Coflow CH <sub>4</sub> diff. flame	GRI-Mech 3.0	A C <sub>2</sub> H <sub>2</sub> based 2-eq. model	DOM	- SNBCK - SNBCK based WB model - OTA	1	1
Smooke et al. [77]	Coflow N <sub>2</sub> diluted C <sub>2</sub> H <sub>4</sub> diff. flames	A modified Sun et al. [266] mech.	A semi-detailed soot model	-	OTA	1	1
Mungekar and Atreya [267]	Partially premixed CH <sub>4</sub> counterflow flames	GRI-Mech 3.0	- (measured $f_s$ )	-	OTA	1	1
Guo and Smallwood [268]	Coflow C <sub>2</sub> H <sub>4</sub> diff. flame	A combined Qin et al. [161] & GRI-Mech 3.0 mechanism	An improved 2-eq. model	DOM	SNBCK-based WB model	1	1
Kong and Liu [18]	Coflow CH <sub>4</sub> diff. flames	GRI-Mech 3.0	A C <sub>2</sub> H <sub>2</sub> based 2-eq. model	DOM	SNBCK-based WB model	1	1 and 0
Katta et al. [269]	C <sub>2</sub> H <sub>4</sub> jet diff. flame	Wang and Frenklach [160]	A C <sub>2</sub> H <sub>2</sub> based 2-eq. model	-	- OTA - No radi.	1	1
Liu et al. [240]	Coflow C <sub>2</sub> H <sub>4</sub> diff. flames	GRI-Mech 3.0	A C <sub>2</sub> H <sub>2</sub> based 2-eq. model	DOM	- SNBCK based WB model - OTA	1	1 and 0
Charest et al. [270]	Coflow C <sub>2</sub> H <sub>4</sub> diff. flames	A skeletal mechanism [271]	A C <sub>2</sub> H <sub>2</sub> based 2-eq. model	DOM	- SNBCK based WB model	0.5–5	1 and 0
Blacha et al. [12]	Coflow C <sub>2</sub> H <sub>4</sub> & kerosene diff. flames	Slavinskaya mechanisms [176,272]	A sectional PAH and soot model	-	OTA	1	1
Demarco et al. [17]	21 NDFs of C <sub>1</sub> to C <sub>3</sub> fuels & 3 C <sub>2</sub> H <sub>4</sub> IDF	Qin et al. [161] mechanism	A C <sub>2</sub> H <sub>2</sub> & C <sub>6</sub> H <sub>6</sub> based 2-eq. model	FVM	- SNBCK - FSCK - OTA	1	1 and 0
Hernández et al. [57]	Counterflow SF C <sub>2</sub> H <sub>4</sub> diff. flames	Davis et al. mechanism [273]	A C <sub>2</sub> H <sub>2</sub> based 2-eq. model	DOM	- SNBCK - No radi.	1	1
Dobbins et al. [274]	Coflow N <sub>2</sub> diluted C <sub>2</sub> H <sub>4</sub> diff. flames	A modified Sun et al. mech [266].	A semi-detailed soot model	DOM	- Planck mean absor. coeff. - $\lambda$ -dependent absor. coeff.	1	1
Abdelgadir et al. [14]	Coflow C <sub>2</sub> H <sub>4</sub> diff. flames	- NBP [164] - KM2 [171]	A detailed model	-	- OTA - No radi.	1, 2, 4 and 8	1
Pejpichestakul et al. [275]	Counterflow SF & SFO C <sub>2</sub> H <sub>4</sub> diff. flames	A detailed mech. consisting of ~ 300 species	A discrete sectional PAH & soot model	-	- OTA - No radi.	1	1
Zheng et al. [276]	Coflow C <sub>2</sub> H <sub>4</sub> diff. flames	ABF [28] mechanism	A detailed soot model	DOM	SNBCK	1	1
Dobbins et al. [277]	Coflow C <sub>2</sub> H <sub>4</sub> diff. flames	A modified Sun et al. mech [266].	A semi-detailed soot model	Photon MC in decoupled calculations	OTA in coupled calculations	1	1 and 0

concentrations of radiating species are high. Neglect of the individual effect of gas and soot radiation results in a similar increase in the peak temperature of about 30 K and 25 K, respectively, Fig. 3(d) and (e). However, the temperatures in the centerline region around the flame tip are overpredicted by more than 80 K and 200 K when gas and soot radiation are neglected, respectively, suggesting that both gas and soot radiation are important and soot is more important than radiating gases in this moderately sooting laminar coflow ethylene/air diffusion flame. If RHT is not taken into account, Fig. 3(f), the predicted temperatures are erroneous since the peak temperature and the temperatures in the centerline region around the flame tip are 123 K and more than 400 K overpredicted using the result of DOM/SNBCK based WB model shown in Fig. 3(b) as the reference.

The predicted soot volume fraction distributions using different radiation treatments are compared with the measured distribution in Fig. 4. As pointed out above, the soot model significantly underpredicted soot along the flame centerline, even though the peak soot volume fraction was well predicted. The effects of radiation treatments mainly lie in the predicted visible flame height, but not in the peak soot volume fraction, which occurs in the flame wing where radiation absorption is fairly weak. Overestimation of radiation heat loss as in OTA leads to a slightly taller visible flame due to reduced soot oxidation rate. Conversely, underestimation of radiation heat loss as in Fig. 4(d)–(f) results in shorter visible flame due to enhanced soot oxidation. The peak soot volume fraction also occurs earlier, i.e., at a lower height along the flame wing due to higher flame temperatures. Therefore, underprediction of thermal

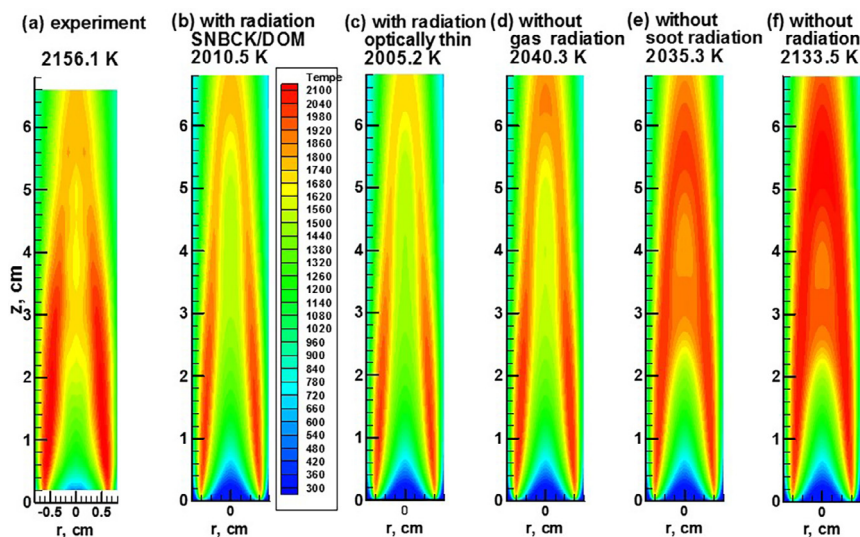


Fig. 3. Comparison of measured and predicted temperature distributions using different models for radiative heat transfer in the laminar coflow  $C_2H_4$ /air diffusion flame. Taken from Liu et al. [16] (with permission).

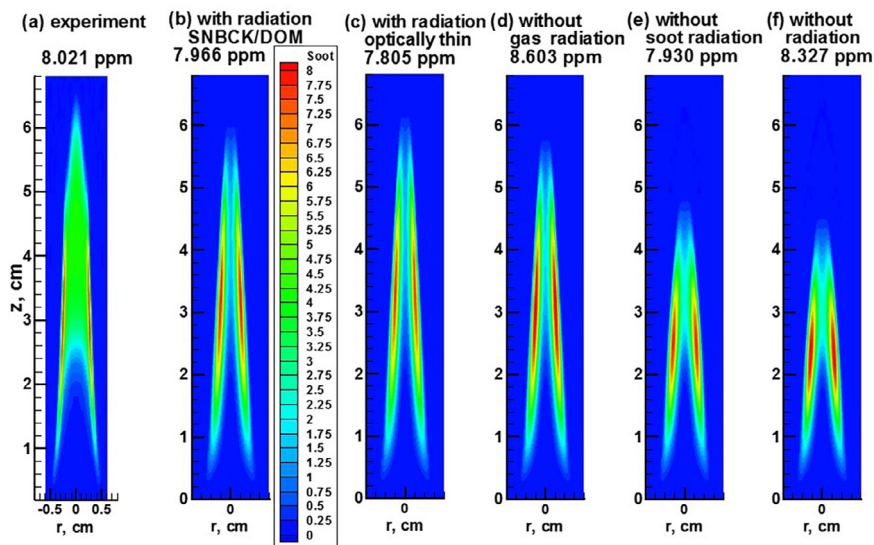


Fig. 4. Comparison of measured and predicted soot volume fraction distributions using different models for radiative heat transfer in the laminar coflow  $C_2H_4$ /air diffusion flame. Taken from Liu et al. [16] (with permission).

radiation loss enhances both soot formation and oxidation, though the latter is more strongly prompted due to the significantly higher temperatures in the upper part of the flame where soot oxidation dominates. Neglect of soot radiation has a strong influence on the visible flame height than neglect of gas radiation in this flame. It is also clear from Fig. 4 that radiation models have essentially negligible impact on the soot inception process in the lower part of the flame wings.

Liu et al. [43] modelled two laminar coflow  $C_2H_4$ /air diffusion flames of different fuel flow rates investigated experimentally by Santoro et al. [278]: one is non-smoking and the other is smoking. The overall model is similar to that used in Liu et al. [16] but with a modified soot oxidation sub-model. Thermal radiation transfer was modelled using DOM coupled a SNBCK based WB model and OTA. They showed that neglect of radiation absorption only weakly lowers the flame temperature on the centerline in the non-smoking flame (by up to about 30 K); however, it strongly lowers the post-flame temperatures on the centerline in the smoking flame by about 150 K. Correspondingly, the use of OTA only

weakly affects the flame cross section integrated soot volume fraction along the height in the non-smoking flame, but results in almost twice the amount of emitted soot in the smoking flame, compared to the amount predicted using the full radiation model, due to reduced soot oxidation rate associated with the lower temperatures in the post-flame region.

The effects of gas and soot radiation on the modelling of laminar counterflow soot formation (SF) ethylene diffusion flames of different oxygen mole fractions in the oxidizer (20, 24, and 28%) at a stretch rate of  $21 \text{ s}^{-1}$  were investigated by Liu et al. [55] using essentially the same soot model and gas-phase chemistry as in Liu et al. [16]. Their results showed that thermal radiation lowered the peak flame temperature by 30, 39, and 50 K, respectively, for 20, 24, and 28% oxygen in the oxidizer and radiation absorption is negligible in all the three flames investigated. In addition, gas radiation plays a larger role than soot radiation in these SF counterflow diffusion flames, since the high concentrations of radiating gases are present in the peak temperature region while the peak soot volume fraction occurs at a fairly low-temperature region around

1100 K on the fuel side. The study of Liu et al. [55] indicates that it is necessary to consider RHT in counterflow diffusion flames and OTA is applicable to produce sufficiently accurate results, i.e., radiation absorption in such counterflow SF diffusion flames can be neglected. More recently, Hernández et al. [57] modelled the same SF counterflow  $C_2H_4$  diffusion flames to those in Liu et al. [55] using the mechanism of Davis et al. [273],  $C_2H_2$  based two-equation soot models, and DOM/SNBCK method for RHT. Although the results of Hernández et al. are qualitatively similar to those of Liu et al., their results display a higher sensitivity to the oxygen mole fraction in the oxidizer. For example, they showed that RHT reduced the peak flame temperature by 20, 25, and 120 K (vs. 30, 39, and 50 K in Liu et al. [55]) when the oxygen mole fraction in oxidizer was 0.2, 0.24, and 0.28, respectively.

The effects of using several approximate SNBCK models in the modelling of a lightly sooting laminar coflow  $CH_4$ /air diffusion flame experimentally investigated by McEnally and Pfeffele [279] were investigated by Liu et al. [199] using the same gas-phase chemistry and soot model as in Liu et al. [16]. In this lightly sooting diffusion flame (visible flame height of about 4 cm and the peak soot volume fraction of about 0.6 ppm), radiation absorption only lowers the predicted peak flame temperature on the centerline region around the flame tip by about 17 K and the predicted soot loading by about 6%, suggesting that the use of OTA is justified in this lightly sooting and fairly small-sized laminar coflow  $CH_4$ /air diffusion flame.

The effects of radiation and radiation absorption on the prediction of three laminar coflow  $N_2$ -diluted  $C_2H_4$ /air diffusion flames were studied by Smooke et al. [77] using a detailed gas-phase reaction mechanism and an improved two-equation soot model. RHT was calculated using OTA and the discrete transfer method coupled with the RADCAL narrow-band model. Their results showed that radiation absorption in the 60% ethylene flame increases the centerline temperatures in the early soot formation zone by up to 40 K, which in turn leads to about 15% increase in the predicted peak soot levels. The results considering radiation absorption consistently display improved distributions of predicted soot volume fraction for the flames studied. In addition, the results of Smooke et al. [77] also showed that neglect of radiation loss led to a shortened visible flame height by 15%, overprediction of the peak centerline temperature by more than 300 K, and significantly higher concentrations of  $C_2H_2$  and benzene. These findings are consistent with those reported in Liu et al. [16].

Mungekar and Atreya [267] reported a combined experimental and numerical study of low stretch-rate ( $< 20 s^{-1}$ ) partially premixed counterflow flames. The effects of gas and soot radiation were investigated using the OPPDIF code, the GRI-Mech 3.0 mechanism, the measured profiles of soot volume fraction, and OTA. Their results of radiation source term display two peaks due to soot radiation at relatively lower temperatures on the fuel side and gas radiation at the peak flame temperature region, regardless of the level of partial premixing. Such radiation structure of partially premixed counterflow flames is qualitatively similar to that of counterflow diffusion flames predicted in the study of Liu et al. [55]. Under their experimental conditions, soot radiation and the radiant fraction due to soot radiation first decreased and then increased with increasing the partial premixing of the fuel stream by oxygen. Although gas radiation monotonically increased with the level of partial premixing, the radiant fraction due to gas radiation decreased due to the higher heat release rate. The net radiant fraction followed the same trend as that due to soot radiation, suggesting that soot radiation played a more important role than gas radiation in these partially premixed counterflow flames.

Guo and Smallwood [268] conducted a numerical study of the interactions between soot and NO formation in a laminar coflow  $C_2H_4$  diffusion flame using an improved two-equation soot

model consisting of  $C_6H_6$  reacting with  $C_6H_5$  as the inception step and HACA as the surface growth step, GRI-Mech 3.0, and the DOM/SNBCK based WB method for RHT modelling. They conducted three simulations to isolate the thermal and chemical effects of soot and NO formation: (i) the full simulation, i.e., with both soot and NO formation, (ii) a simulation without soot formation and at the same temperature distribution from (i), and (iii) a full simulation, except without soot formation. The differences between the results of (i) and (ii) and between (ii) and (iii) are ascribed to the chemical and thermal effect, respectively. In this moderately sooting diffusion flame, their results showed that the formation of NO has almost no influence on soot formation. However, the formation of soot significantly reduces the formation of NO. The formation of soot lowers the peak NO concentration and NO emission index by 28 and 46%, respectively. The decrease in NO formation by soot formation is primarily caused by the thermal effect (more than 80%) since the formation of soot significantly reduces the temperatures in the upper part of the flame. The study of Guo and Smallwood [268] once again demonstrates that thermal radiation plays an important role in kinetically controlled processes.

The importance of RHT in laminar coflow  $CH_4$ /air [18] and  $C_2H_4$ /air [240] diffusion flames at microgravity was investigated using the same soot model, gas-phase chemistry, and full radiation model (DOM/SNBCK based WB) as in Liu et al. [16]. Kong and Liu [18] investigated the effects of RHT on the structure and soot formation of a laminar coflow  $CH_4$ /air diffusion flame at different coflow air velocities (77.6, 30, and 5 cm/s) and at three gravity levels (1, 0.5, and 0 g). Liu et al. [240] investigated the effects of gravity (at 1 and 0 g) and RHT on the structure and soot formation characteristics of the laminar coflow  $C_2H_4$  diffusion flame previously studied by Liu et al. [16], which is close to the smoke point. These studies showed that RHT becomes much more important at microgravity than at earth gravity due to the following two factors. First, at microgravity the radial diffusion becomes more important, leading to a wider flame and larger flame optical thickness. Second, the absence of buoyancy induced flow acceleration significantly increases the residence time, which prompts soot formation (except at the lowest coflow air velocity in Kong and Liu [18]) and hence radiation heat loss. Specifically, the flame centerline temperatures are more significantly reduced by RHT at microgravity with decreasing the coflow air velocity and can cause more than 800 K decrease in the peak temperature on flame centerline at the lowest coflow air velocity of 5 cm/s in the study of Kong and Liu [18]. Based on this predicted trend, Kong and Liu [18] conjectured that the laminar coflow  $CH_4$ /air diffusion flame may experience radiation-induced extinction along the centerline at a sufficiently low coflow air velocity, similar to the radiation-induced extinction of counterflow diffusion flames at low stretches [280], though their conjecture has yet to be validated experimentally. It is also interesting to notice that the non-smoking laminar coflow  $C_2H_4$ /air diffusion flame at 1 g becomes smoking at 0 g due to the drastic reduction of centerline temperatures by 1000 K in the upper part of the flame and hence much suppressed soot oxidation rates. To demonstrate the critical role of RHT in this transition from non-smoking to smoking flame with decreasing gravity, Liu et al. [240] conducted additional calculations without RHT and the results confirmed that the flame remains non-smoking at 0 g when RHT was not considered. These two studies [18,240] show that RHT in laminar coflow diffusion flames has a much stronger influence on the flame centerline temperatures and soot oxidation in the upper part of the flames at 0 g than their counterparts at 1 g. Although radiation absorption in lightly to moderately sooting laminar coflow diffusion flames at 1 g does not cause a large temperature difference, its importance has also been emphasized by Smooke et al. [10] and Blacha et al. [12] due to the strong temperature dependence of gas-phase and soot chemistry.

The role of soot radiation on the suppression of flicker of coflow diffusion flames at normal gravity and atmospheric pressure was investigated experimentally and numerically by Katta et al. [269]. Numerically, they modelled the laminar coflow flames of  $\text{CH}_4/\text{C}_2\text{H}_2$  mixtures using the Wang and Frenklach mechanism [160], a  $\text{C}_2\text{H}_2$  based two-equation soot model, and OTA for radiation loss. Their results showed that the magnitude of flame flicker can be suppressed to produce steady flames when a sufficient amount of  $\text{C}_2\text{H}_2$  is added to the fuel stream to prompt soot formation, which leads to enhanced radiation loss. They also showed numerically that a steady diffusion flame can become unsteady when soot radiation was turned off, confirming that soot radiation plays a stabilizing role in laminar coflow diffusion flames. Charest et al. [270] conducted a numerical study to investigate the effects of pressure and gravity on laminar coflow ethylene diffusion flames using the skeletal  $\text{C}_2$  mechanism of Law [271], a  $\text{C}_2\text{H}_2$  based two-equation soot model, and the DOM/SNBCK based WB method for modelling RHT. They showed that radiation loss is responsible for the lengthened flame height with increasing pressure at microgravity, significantly reduced temperatures along the flame centerline in microgravity, especially at elevated pressures, and reduced sensitivity of carbon conversion rate to pressure above 1 atm.

Demarco et al. [17] investigated the importance of RHT on soot prediction in a large number of laminar coflow diffusion flames, including 21 normal diffusion flames (NDFs) of  $\text{C}_1$ – $\text{C}_3$  fuels and 3 ethylene inverse diffusion flames (IDFs). Among the flames investigated, three NDFs and one IDF are at 0 g. These laminar flames covered a wide range of flame height defined by the stoichiometric mixture fraction on the flame centerline up to 13.92 cm, a wide range of residence time (from burner exit to the flame tip) up to 495 ms, and optical thickness (defined by the maximum integral of Planck mean absorption coefficients of  $\text{CO}_2$ ,  $\text{H}_2\text{O}$ , and soot along flame diameter) up to 0.081. Soot formation was modelled using a semi-empirical two-equation soot model consisting of  $\text{C}_2\text{H}_2$  and  $\text{C}_6\text{H}_6$  for inception [70],  $\text{C}_2\text{H}_2$  addition for surface growth, and oxidation by  $\text{O}_2$  and  $\text{OH}$  and  $\text{O}$  radicals. RHT was modelled using OTA, gray model based on the Planck mean absorption coefficients, and statistical narrow-band correlated-k (SNBCK) and full-spectrum correlated-k (FSCK) non-gray radiative property models. FVM was used as the RTE solver in the gray-model, SNBCK, and FSCK calculations. Their results indicate that RHT is important in all the flames and should always be considered. The importance of RHT is dependent on the soot loading and residence time. In general, RHT is more important in NDFs than in IDFs and is significantly enhanced at reduced gravity. Demarco et al. [17] concluded that OTA can be used for flames whose maximum radially integrated optical thickness based on the Planck mean coefficients of  $\text{CO}_2$ ,  $\text{H}_2\text{O}$ , and soot is less than 0.05, since under this condition the maximum deviation in temperature prediction is less than 20 K. Moreover, they found that the gray model based on the Planck mean absorption coefficient does not provide significant improvement over OTA and the FSCK offers similar accuracy as SNBCK with a substantial saving in computational time.

Dobbins et al. [274] conducted a detailed analysis of radiative emission and reabsorption in three laminar coflow nitrogen diluted ethylene diffusion flames without and with radiation absorption in RHT modelling by using OTA and solving RTE with DOM, respectively. The radiative property of radiating species including soot was the Planck mean absorption coefficient and the wavelength-dependent one extracted from RADCAL. It is noticed that the peak soot volume fraction in the most sooting flame investigated was less than 2 ppm and the visible flame height was about 65 mm. They found that radiation absorption is non-negligible and use of OTA can underpredict temperatures in the centerline region around the flame tip by up to 27 K in the flames investigated. Under the

conditions of their study,  $\text{CO}_2$  was found to play a dominant role in the emission and absorption of radiation.

Abdelgadir et al. [14] conducted a detailed numerical study of soot formation in laminar coflow  $\text{C}_2\text{H}_4$  diffusion flames at elevated pressures up to 8 atm using two detailed gas-phase mechanisms with PAH formation, a detailed soot model, and OTA. They discussed the effects of radiative heat loss on the predicted soot concentrations and temperatures based on their results and previous modelling results of laminar coflow and counterflow diffusion flames. Their results showed that neglect of radiation loss caused a decrease in the predicted peak soot volume fraction by 26, 21, 22, and 13% at 1, 2, 4, and 8 atm, respectively. They considered such levels of reduction of soot by radiation losses in line with previously reported results in Liu et al. [16], [55], Hernández et al. [57], though the latter studies were conducted at atmospheric pressure. Radiation losses lowered the flame temperatures along the centerline by about 100 K at 8 atm. This magnitude of temperature reduction by radiation loss is comparable with the results reported in Liu et al. [16], Charest et al. [270], in spite of different flame conditions.

The importance of radiative loss in modelling counterflow SF and SFO diffusion flames has been recently further investigated by Pejpichestakul et al. [275]. Counterflow  $\text{C}_2\text{H}_4$  diffusion flames were modelled using a detailed reaction mechanism with PAH formation up to pyrene, a discrete sectional approach for larger PAH and soot formation, and OTA. The SF flames are the same as those investigated previously by Liu et al. [55] and Hernández et al. [57], while the SFO flames were generated by modifying the compositions in both the fuel and oxidizer streams while keeping their velocities at 19.5 cm/s and a burner separation distance of 1.42 cm. The results of Pejpichestakul et al. showed that radiation losses reduce flame temperatures in the range of about 20 to 30 K and 50 to 60 K in SF and SFO flames, respectively. The somewhat larger temperature reduction in SFO flames is due to their higher flame temperatures. The reduction in SF flames is similar to but smaller than that (20 to 50 K) reported by Liu et al. [55].

$\text{CO}_2$ ,  $\text{H}_2\text{O}$ ,  $\text{CO}$ , and soot have been commonly considered as the radiating species in modelling RHT in both laminar and turbulent flames. Although the potential importance of radiation absorption by hydrocarbon fuel molecules has been shown in pool fires, e.g., in Consalvi and Liu [212], it has been rarely taken into account in laminar and turbulent flame modelling. A few efforts have been made in this regard. Dobbins et al. [274] considered the absorption of ethylene in their modelling of laminar coflow nitrogen diluted  $\text{C}_2\text{H}_4$ /air diffusion flames and found that absorption by ethylene had only little effect on the results. Recently, Zheng et al. [276] conducted a numerical study to investigate the importance of  $\text{C}_2\text{H}_2$  and  $\text{C}_2\text{H}_4$  absorption and emission on modelling soot formation in a laminar coflow  $\text{C}_2\text{H}_4$ /air diffusion flame at atmospheric pressure. The gas-phase chemistry was modelled using the ABF mechanism [28] and soot was modelled using a detailed model. They first generated the SNB model parameters of  $\text{C}_2\text{H}_2$  and  $\text{C}_2\text{H}_4$  from the HITRAN 2016 database and then included these two hydrocarbon species in the modelling of RHT using the DOM/SNBCK method. Under the flame conditions of their study, their results showed that inclusion of  $\text{C}_2\text{H}_2$  and  $\text{C}_2\text{H}_4$  in RHT results in somewhat lower predicted soot volume fractions by about 5 to 10%, depending on the flame height, and the peak soot volume fraction occurs at a somewhat higher location.

Very recently, Dobbins et al. [277] conducted a combined experimental and numerical study of soot formation in laminar coflow  $\text{C}_2\text{H}_4$ /air diffusion flames at microgravity. Two laminar diffusion flame burners were used in the study: the smaller ACME coflow burner with the inner and outer diameters of the fuel tube of 2.16 and 2.41 mm and the larger Yale burner with the inner and outer diameters of the fuel tube of 3.9 and 4.7 mm. The fuel and air flow

rates are such that the mean inlet velocities of both the fuel and air streams are 35 cm/s and the resultant visible heights of the Yale and ACME flames are about 68 and 16 mm at normal gravity, respectively. The chemical kinetics and soot model used in the modelling have been described in their earlier publications [77,274]. RHT was modelled using OTA described in Dobbins et al. [274]. To access the importance of radiation absorption, a Monte Carlo ray tracing method coupled with a line-by-line spectral database was used to solve RTE in a post-processing fashion, i.e., decoupled calculations using converged thermal fields. For the ACME flame, the numerical simulation overpredicted and underpredicted the soot volume fractions compared to measurements at 1 g and 0 g, respectively. Therefore, the flame model predicted a much weaker influence of gravity on soot formation than experiments. For the Yale flame, the predicted soot volume fractions are only about 60% of the measured values at 1 g and there was no experimental data at 0 g. The predicted peak soot volume fraction at 0 g was only about 50% higher than the 1 g value, showing a significantly weaker influence of gravity on soot formation compared to previous studies [18,240,270]. Both Kong and Liu [18], who modelled the gravity effect on soot formation of a laminar coflow CH<sub>4</sub>/air diffusion flame of about 63 mm visible height, and Charest et al. [270], who studied the influence of gravity on soot formation of a laminar coflow C<sub>2</sub>H<sub>4</sub>/air diffusion flame of about 8 mm visible height, predicted 100% increase in peak soot volume fraction at 0 g compared to the value at 1 g. In addition, the results of Dobbins et al. showed that both the ACME and Yale flames are lightly smoking at both 1 g and 0 g, though both the ACME and Yale flames are non-smoking (unclear for the Yale flame at 0 g due to absence of experiments). Their analysis of radiation losses indicated that thermal radiation caused 12.8 and 17.1% loss of heat release in the ACME flame and 27.5 and 47.5% loss in the Yale flame at 1 g and 0 g, respectively. Although they showed that radiation absorption is more important at 0 g for temperature-sensitive species, e.g., soot, they also suggested that OTA was adequate in the simulation of the two flames at both 1 g and 0 g. They pointed out that the increased radiation absorption at 0 g is mainly caused by the enhanced absorption by CO<sub>2</sub> rather than by soot. Clearly, there is a need to further investigate the effects of radiation and radiation absorption on soot formation in laminar coflow diffusion flames, especially at micro-gravity.

### 3.5. Turbulence/radiation interaction

The Reynolds-averaged spectral RTE and radiative source term in the energy equation are expressed as Modest and Haworth [23]:

$$\mathbf{s} \cdot \nabla \langle I_\eta \rangle + \langle \kappa_\eta(\phi) I_\eta \rangle = \langle \kappa_\eta I_{b,\eta}(T) \rangle \quad (60)$$

$$\langle S_R \rangle = \int_{\eta=0}^{\infty} \langle \kappa_\eta G_\eta \rangle d\eta - 4\pi \langle \kappa_p(\phi) I_b(T) \rangle \quad (61)$$

where  $G_\eta = \int_{4\pi} I_\eta d\Omega$ . Both absorption and emission terms are highly non-linear functions of temperature, composition,  $\phi$ , and spectral intensity. A consequence is that their mean value cannot be accurately evaluated from mean quantities [23,24]:

$$\langle \kappa_\eta(\phi) G_\eta \rangle \neq \kappa_\eta(\tilde{\phi}) \langle G_\eta \rangle \quad \text{or} \quad \langle \kappa_\eta(\phi) I_\eta \rangle \neq \kappa_\eta(\tilde{\phi}) \langle I_\eta \rangle \quad (62)$$

$$\langle \kappa_p(\phi) I_b(T) \rangle \neq \kappa_p(\tilde{\phi}) I_b(\tilde{T}) \quad \text{or} \quad \langle \kappa_\eta(\phi) I_{b,\eta}(T) \rangle \neq \kappa_\eta(\tilde{\phi}) I_{b,\eta}(\tilde{T}) \quad (63)$$

The differences are manifestation of the turbulence/radiation interaction in the RANS context.

Similarly, the filtered RTE and radiative source term (in LES) involve the highly non-linear filtered absorption and emission terms, such as:

$$\langle \kappa_\eta(\phi) G_\eta \rangle_\Delta \neq \kappa_\eta(\hat{\phi}) \langle G_\eta \rangle_\Delta \quad \text{or} \quad \langle \kappa_\eta(\phi) I_\eta \rangle_\Delta \neq \kappa_\eta(\hat{\phi}) \langle I_\eta \rangle_\Delta \quad (64)$$

$$\langle \kappa_p(\phi) I_b(T) \rangle_\Delta \neq \kappa_p(\hat{\phi}) I_b(\hat{T}) \quad \text{or} \quad \langle \kappa_\eta(\phi) I_{b,\eta}(T) \rangle_\Delta \neq \kappa_\eta(\hat{\phi}) I_{b,\eta}(\hat{T}) \quad (65)$$

The differences are manifestation of the turbulence/radiation interaction in the LES context.

Table 7 shows that TRI was usually neglected in RANS simulations of turbulent non-premixed sooting jet flames despite the experimental evidences of their strong effects on radiative loss [281–283]. Similarly SGS TRI was neglected in LES of such flames. The objective of the present section is to discuss the strategies to model TRI in both RANS and LES contexts and to highlight their specificity and importance for the modelling of sooting flames.

#### 3.5.1. Modelling absorption TRI

*RANS context* The Reynolds-averaged absorption term can be rewritten by introducing the correlation between the fluctuations of the absorption coefficient and the radiative intensity:

$$\langle \kappa_\eta I_\eta \rangle = \langle \kappa_\eta \rangle \langle I_\eta \rangle + \langle \kappa'_\eta I'_\eta \rangle \quad (66)$$

The evaluation of  $\langle \kappa'_\eta I'_\eta \rangle$  is difficult because the fluctuations of the local intensity are influenced by fluctuations that arise from spatial locations that can be anywhere in the medium. Modelling absorption TRI requires then a detailed knowledge of the instantaneous fields of temperature and composition, and solving the RTE over a significant amount of realizations of the flow [23,24]. Wang et al. proposed a particle PMC/TPDF method to model these complex interactions. This method relies on the fact that TPDF methods based on Monte Carlo scheme and an ensemble of Lagrangian notional particles provide actual realizations of the flow. A specific Monte Carlo method was developed to handle the interactions between the photons and the notional particles [207]. Metha et al. applied this model to simulate lab- and large-scale sooting jet flames in conjunction with an acetylene based soot production model and a method of moment to model soot particle dynamics [162]. They concluded that  $\langle \kappa'_\eta I'_\eta \rangle$  can be reasonably neglected even in large-scale highly sooting flames. This welcome conclusion was latter confirmed by Consalvi and Nmira [91]. The approximation of neglecting  $\langle \kappa'_\eta I'_\eta \rangle$  is usually referred to as the optically-thin fluctuation approximation (OTFA) in the literature and was first introduced by Kabashnikov and Myasnikova [284]. It was applied in most of the studies dealing with TRI (see for example Table 7).

*LES context* The filtered absorption term can be decomposed into the sum of a resolved and a subgrid fluctuation:

$$\langle \kappa_\eta I_\eta \rangle_\Delta = \underbrace{\kappa_\eta(\hat{\phi}) \langle I_\eta \rangle_\Delta}_{ReS} + \underbrace{[\langle \kappa_\eta I_\eta \rangle_\Delta - \kappa_\eta(\hat{\phi}) \langle I_\eta \rangle_\Delta]}_{SGS} \quad (67)$$

Only the SGS absorption TRI requires modelling. A consensus was established that SGS absorption TRI can be neglected in LES of both non-sooting and sooting flames [167,285,286].

#### 3.5.2. Modelling emission TRI

Emission TRI depends only on local scalars, such as temperature and composition, and its modelling is a closure problem similar to that encountered for chemical reaction rates or soot reaction rates (see Section 2.3) owing to turbulence/chemistry interaction (TCI) and turbulence/soot (TSI), respectively. Therefore, the modelling of emission TRI is closely related to the turbulent combustion model used in the simulations.

*RANS context* Moment-based closures of emission TRI were mainly used in conjunction with the eddy dissipation concept and

gray radiation models [287]. They consists in approximating the mean emission term by a Taylor series expansion and retaining only the lower-order moments:

$$\begin{aligned} \langle \kappa I_b \rangle &\propto \langle \kappa T^4 \rangle \\ &\approx \langle \kappa \rangle \langle T \rangle^4 \left[ 1 + 6C_{TRI_1} \frac{\langle T'^2 \rangle}{\langle T \rangle^2} + 4C_{TRI_2} \frac{\langle T'^2 \rangle}{\langle \kappa \rangle \langle T \rangle} \left( \frac{\partial \kappa}{\partial T} \right)_{(T)} \right] \end{aligned} \quad (68)$$

The last term on the right hand side is usually neglected and  $C_{TRI_1}$  is adjusted to match the experimental data [287].

Flamelet/presumed PDF approaches were mainly applied to model emission TRI in non-sooting flames by assuming  $\delta$ -Dirac functions for the scalar dissipation,  $\chi$ , and the enthalpy defect,  $X_R$ , and a  $\beta$ -function for mixture fraction [288–290]. The accuracy of the  $\beta$ -PDF to model mixture fraction statistics in the context of emission TRI was demonstrated by Deshmukh et al. from DNS [291]. Similarly to the TSI closure issue discussed in Section 2.3, the design of a joint presumed PDF of both gas-phase and soot related quantities is a difficult task and to the authors' best knowledge no attempt was reported to model TRI in sooting flames with this approach.

TPDF [145,162,292–294] and HFTPfDF methods [75,150,295], that provide an exact closure of emission TRI, were considered in both non-sooting and sooting turbulent flames. These studies had mainly aimed to improve the understanding of the processes responsible for TRI as well as their impact on the prediction of radiative outputs and flame structures. They will be discussed in details in the next sections.

Yunardi et al. [152] applied a first order CMC closure to model emission TRI in conjunction with the OTA in a turbulent non-premixed ethylene jet flames:

$$\langle \kappa_p I_b | Z \rangle \approx \kappa_p (\langle \phi | Z \rangle I_b (\langle \phi | Z \rangle)) \quad (69)$$

However, to the authors' best knowledge, no systematic investigation of the modelling of emission TRI with CMC was reported in the literature.

*LES context* The filtered emission term can be decomposed into a resolved and a SGS contribution:

$$\langle \kappa_p(\phi) I_b(T) \rangle_{\Delta} = \underbrace{\kappa_p(\hat{\phi}) I_b(\hat{T})}_{ReS} + \underbrace{[\langle \kappa_p(\phi) I_b(T) \rangle_{\Delta} - \kappa_p(\hat{\phi}) I_b(\hat{T})]}_{SGS} \quad (70)$$

Only the SGS emission TRI requires modelling. The relative contributions of resolved and SGS emission TRI depend on the filter size, with the SGS emission TRI increasing with the filter width (mesh size) [285,286]. Recent works related to turbulent non-luminous and luminous non-premixed flames [167] and medium and large scale non-luminous pool fires [205,296] showed that, for filter sizes that resolved more than 80% of turbulent fluctuations, the effects of SGS fluctuations on the filtered emission term have to be modelled and can even exceed those of resolved-scale fluctuations. These studies showed also that the contribution of SGS emission TRI increases with the SGS optical thickness.

On the other hand, few studies have considered SGS emission TRI in the simulations of flames. The moment-based approach described by Eq. (68) was extended to model SGS emission TRI in LES of n-heptane fire plumes [297,298] and the constant  $C_{TRI_1}$  was adjusted to match the experimental data. Few works applied flamelet/presumed FDF models to model SGS emission TRI in non-luminous non-premixed turbulent flames [205,296,299,300]. To the authors' best knowledge, the only work considering TPDF method was reported by Gupta et al. [167] to provide a detailed examination of TRI in LES of the baseline Sandia flame D and synthetic flames generated by scaling up the baseline flame with a factor of 4 and introducing soot from an empirical correlation.

### 3.5.3. Radiative structure of sooting turbulent non-premixed flames

Emission TRI is usually decomposed into the sum of three contributions, namely the Planck-mean absorption coefficient-temperature cross-correlation ( $C(\kappa_p, T)$ ), the Planck function or temperature self-correlation ( $C(T, T)$ ), and the Planck-mean absorption coefficient self-correlation ( $C(\kappa_p, \kappa_p)$ ) [23,24]:

$$\begin{aligned} \langle \kappa_p(\phi) I_b(T) \rangle &= \underbrace{\kappa_p(\tilde{\phi}) I_b(\tilde{T})}_{\text{No TRI}} + \underbrace{[\langle \kappa_p \rangle - \kappa_p(\tilde{\phi})] I_b(\tilde{T})}_{C(\kappa_p, \kappa_p)} \\ &+ \underbrace{\langle \kappa_p \rangle [I_b - I_b(\tilde{T})]}_{C(T, T)} + \underbrace{[\langle \kappa_p I_b \rangle - \langle \kappa_p \rangle \langle I_b(T) \rangle]}_{C(\kappa_p, T)} \end{aligned} \quad (71)$$

Local flame emission in sooting flames results from the additional contributions of gas and soot. Gas emission TRI in non-premixed flames was investigated theoretically by Coelho [301] and numerically by several other authors in canonical flames [134,289,292,293,302]. These studies showed that gas emission is systematically enhanced by TRI with the contributions of the temperature self-correlation and the absorption coefficient-Planck function correlation being dominant. A consequence is that TRI always enhanced the flame radiative loss, confirming the early experimental conclusions of Fisher et al. [303] and Faeth and co-workers [281,282,304–308]. The levels of enhancement were found to increase with the optical thickness [207,293,309,310]. Table 9 illustrates these conclusions through different examples and provides a quantification in the level of enhancement in different combustion scenarios.  $\dot{Q}_{net}$  represents the total radiative loss obtained by integrated the divergence of the radiative flux over the computational domain. Wang et al. [207] applied the PMC method combined with a TPDF method to investigate TRI effects in the SANDIA flame D [311] and two other artificial flames derived from it by scaling up the fame diameter by a factor of 2 and 4 while maintaining the Reynolds number constant. The enhancement of radiative loss due to TRI was found to increase with the optical thickness from 29% for the baseline SANDIA flame D to 34% for the largest flame (see Table 9). Nmira et al. [310] used a HFTPfDF method in conjunction with the NBCK and the FVM as RTE solver to simulate artificial  $H_2$  high-pressure non-premixed flames. The flames were designed from that investigated by Barlow and Carter [312] by applying a Froude scaling in order to preserve the flame geometry and the residence times while increasing the pressure and, in turn, the optical thickness. This allows isolating the effects of pressure on TRI. TRI effects were found to be enhanced with pressure as shown in Table 9, with an increase in  $\dot{Q}_{net}$  from 39% at 1 atm to about 49% at 30 atm. Fraga et al. [313] modelled the 50 cm-diameter ethanol pool fire investigated experimentally by Fisher et al. [303] by using the Fire Dynamics Simulator [314]. In accordance with the other investigations of TRI in medium and large-scale pool fires [205,289,296], they found that TRI contributes for the major part to flame radiative loss (about 75% as shown in Table 9). This feature is specific to pool fires that are characterized by a very-high intermittency resulting from the puffing process.

The understanding in the soot emission TRI in non-premixed flames has widely benefited from the development of temporally and spatially-resolved measurement techniques of soot and temperature initiated by Gore, Sivathanu and co-workers in the early 90's [315,316]. They developed a three-line optical probe consisting of laser extinction at 632 nm and two wavelength emission pyrometry at 900 nm and 1000 nm, respectively. Soot volume fraction was inferred from both extinction and emission measurements whereas the temperature was inferred from the emission measurements. They applied this technique to turbulent acetylene flames [315], highly buoyant turbulent acetylene/air and propylene/air flames [317], 30 cm toluene pool fires [318] and 6 m  $\times$  6 m JP8 pool fires [319]. Their technique was also applied by other au-

**Table 9**

Effects of TRI on flame radiative loss.  $\Delta TRI = \frac{(\dot{Q}_{net})_{TRI} - (\dot{Q}_{net})_{NoTRI}}{(\dot{Q}_{net})_{TRI}} \times 100$ .

Authors	Flame	Without TRI $\dot{Q}_{net}$ (kW)	With TRI $\dot{Q}_{net}$ (kW)	$\Delta TRI$ (%)
Wang et al. [207]	SANDIA D	0.50	0.645	29.0
	2 D	2.57	3.27	27.2
	4 D	8.48	11.37	34.1
Nmira et al. [310]	H <sub>2</sub> P = 1 atm	2.00	3.31	39.43
	P = 5 atm	8.91	14.17	37.16
	P = 10 atm	12.74	22.86	44.26
	P = 30 atm	22.05	47.56	49.43
Fraga et al. [313]	0.5 m CH <sub>3</sub> OH pool fire	3.40	13.5	74.9

thors to 2 m diameter JP8 fires [320] and 15 cm ethylene buoyant flames in oxygen depletion conditions [321]. These studies showed that soot volume fractions inferred from absorption measurements are significantly higher than those inferred from emission data, suggesting the presence of large quantities of relatively cold soot within the flames. They also observed that the correlation between soot volume fraction and temperature is highly negative in the soot emission region. This latter feature was confirmed by RANS simulations based on TPDF methods [204,295,322,323] and LES [170] of turbulent non-premixed jet flames. The two physical mechanisms responsible for this negative correlation were elucidated in Ref. [204]. The first can be explained from Fig. 1. This figure shows that the hot soot, responsible for radiative emission, is located in the region between the peak of conditional mean of soot volume fraction and the stoichiometry. In this region, which roughly corresponds to the region where soot oxidation occurs, soot volume fraction decreases whereas the temperature increases, explaining the negative correlation between  $f_s$  and  $T$ . This mechanism is then related to the non-premixed flame structure and, consequently, does not depend of the fuel sooting propensity as revealed in Ref. [204]. The second mechanism was found to be less significant and directly related to the fuel sooting propensity. It can be explained as follows: in the region of hot soot, a positive fluctuation in soot volume fraction results in an increase in radiative loss and then a decrease in temperature [204]. The negative correlation between the soot volume fraction and the temperature plays a major role on soot emission TRI. This can be highlighted by introducing the expressions of  $I_b = \sigma T^4/\pi$  and  $\kappa_{p,s} = C f_s T$ , where  $C$  is a constant, in the mean soot emission term and expanding it in Taylor series. Considering only the lowest order terms in the truncated series leads to Rodrigues et al. [170]:

$$\langle \kappa_{p,s} I_b \rangle = \underbrace{\frac{\sigma C}{\pi} \langle f_s \rangle \langle T \rangle^5}_{NoTRI} \left( 1 + 5 \frac{\langle f_s' T' \rangle}{\langle f_s \rangle \langle T \rangle} + 10 \frac{\langle T'^2 \rangle}{\langle T \rangle^2} \right) \quad (72)$$

Eq. (72) shows that the effects of TRI on mean soot emission results from a balance between an enhancement due to the contribution of the temperature self-correlation (last term in the parenthesis on the right hand side) and a reduction owing to the negative correlation between soot volume fraction and temperature (second term in the parenthesis on the right hand side) [170,323]. The effects of disregarding the cross-correlation between soot volume fraction and temperature was assessed in Ref. [295] from RANS simulations of the propane non-premixed jet flame burning in an 40% oxygen-enriched oxidizer investigated experimentally in Ref. [159]. These effects are illustrated in Fig. 5 which shows the axial profiles of the correlation between the soot volume fraction and the temperature,  $C(f_s, T) = \frac{\langle f_s' T' \rangle}{\sqrt{\langle f_s'^2 \rangle} \sqrt{\langle T'^2 \rangle}}$  and of the divergence of the radiative flux, temperature and soot volume fraction with and without considering the correlation. The simulations were performed with a HFTPDP method, a two-equation acetylene/benzene based soot model and the RTE was solved by the FVM with a

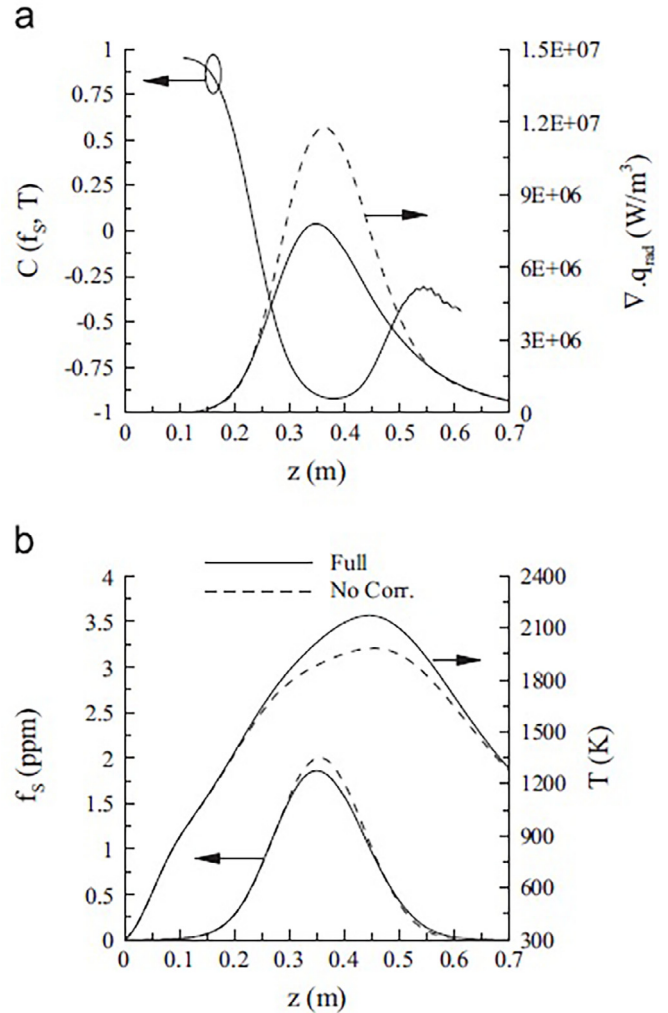


**Fig. 5.** Effects of the correlation between soot volume fraction and temperature. (a) Axial evolution of soot volume fraction-temperature correlation and divergence of the radiative flux. (b) Axial evolution of soot volume fraction and temperature. The solid lines refer to simulations considering the correlation whereas the dashed lines refer to simulations disregarding it. Taken from Consalvi and Nmira [295] (with permission).

WBCK as radiative property model. As expected from the previous discussion,  $C(f_s, T)$  becomes strongly negative in the soot region. Considering the correlation (Full) reduces substantially the radiative loss, leading to an increase in the peak temperature of about 150 K. Both soot surface growth and oxidation were found to be noticeably affected (not shown). However, these effects are balanced leading to relatively small overall effects on soot volume fraction.

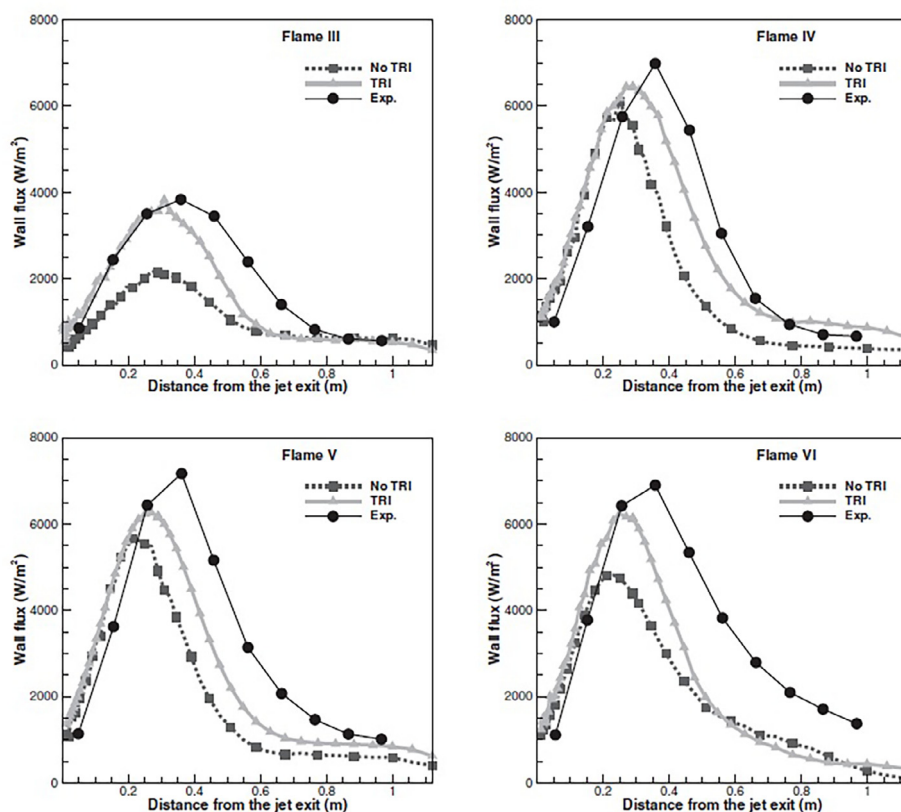


Fig. 6. Effects of TRI on incident radiative wall fluxes. Taken from Mehta et al. [162] (with permission).

Table 10

Resolved and subgrid-scale TRI contributions in the 4D flame + soot. Adapted from Gupta et al. [167] (with permission).

Name	Emission		Absorption		$\chi_R$ (-) 4D
	ReS	SGS	ReS	SGS	
TRI0	N	N	N	N	0.22
TRI1F	Y	N	N	N	0.327
TRI2F	Y	N	Y	N	0.308
TRI3F	Y	Y	Y	N	0.487
TRI4F	Y	Y	Y	Y	0.480

The previous discussion shows that complex competitive mechanisms govern the effects of TRI on radiative loss in sooting non-premixed flames. Enhancement mechanisms are due to gas emission TRI and temperature self-correlation effects on soot emission whereas inhibiting mechanisms results from the negative correlation between soot volume fraction and temperature [170,323]. A specific numerical study was performed in Ref. [323] by simulating turbulent lab-scale non-premixed jets ranging from the transitional to the momentum-driven regimes and fuelled by a weakly sooting fuel, methane, a moderately sooting fuel, ethylene, and a heavily sooting fuel, acetylene. It was found that enhancement mechanisms dominate in weakly sooting methane flames and taking TRI into account increases the radiant fraction. On the other hand, inhibiting mechanisms become of increasing importance in moderately and highly sooting fuels, with their importance increasing with both the fuel sooting propensity and the Reynolds number. For flames dominated by soot radiation, the inhibiting mechanisms were found to prevail and taking TRI into account reduces the radiative loss.

### 3.5.4. Effects of TRI on soot production and sooting flame radiative loss

This section illustrates how neglecting TRI can affect soot production and radiative heat transfer. In the RANS context, the simulations reported by Mehta et al. [162] are considered (see Table 7 for the modelling details). The oxygen-enhanced flames fuelled by a blend of 90% methane/10% ethylene of Wang et al. [261] were used as target flames. In these experiments, the fuel was injected through a 3-mm nozzle at a velocity of 35.4 m/s (Reynolds number of about 6700) and four oxygen concentrations in the oxidizer of 21% (Flame III), 30% (Flame IV), 40% (Flame V) and 55% (Flame VI) were investigated. In the four flames, gas radiation was found to strongly dominate the radiative heat transfer. In such conditions, TRI is expected to enhance radiative heat loss from the flame as expected from the discussion of the last Section 3.5.3. This is illustrated in Fig. 6 that shows that the wall incident radiative flux along the combustion chamber is significantly increased when TRI is considered. On the other hand, these enhancements in radiative loss are expected to result in lower temperature in the flames and, in turn, in a reduction in soot production. These effects are observed in Fig. 7 that shows the equivalent soot volume fraction defined as  $f_{s,EQ} = \frac{1}{D} \int_{-\infty}^{+\infty} f_s(r, z) dr$  where  $D$  is the nozzle diameter, along the height as a function of the height above the burner. Equivalent soot volume fractions are in closer agreement with experimental data and substantially lower when TRI is taken into account.

In the LES context, to the authors' best knowledge, the only study related to the relative importance of resolved and SGS TRI contributions in sooting flames was reported by Gupta et al. [167]. LES of the SANDIA flame D and artificial flames constructed by scaling up the dimensions of flame D by a factor of four were performed with advanced combustion and radiation models (see Table 7 for the modelling details). In their simulations, 84% of

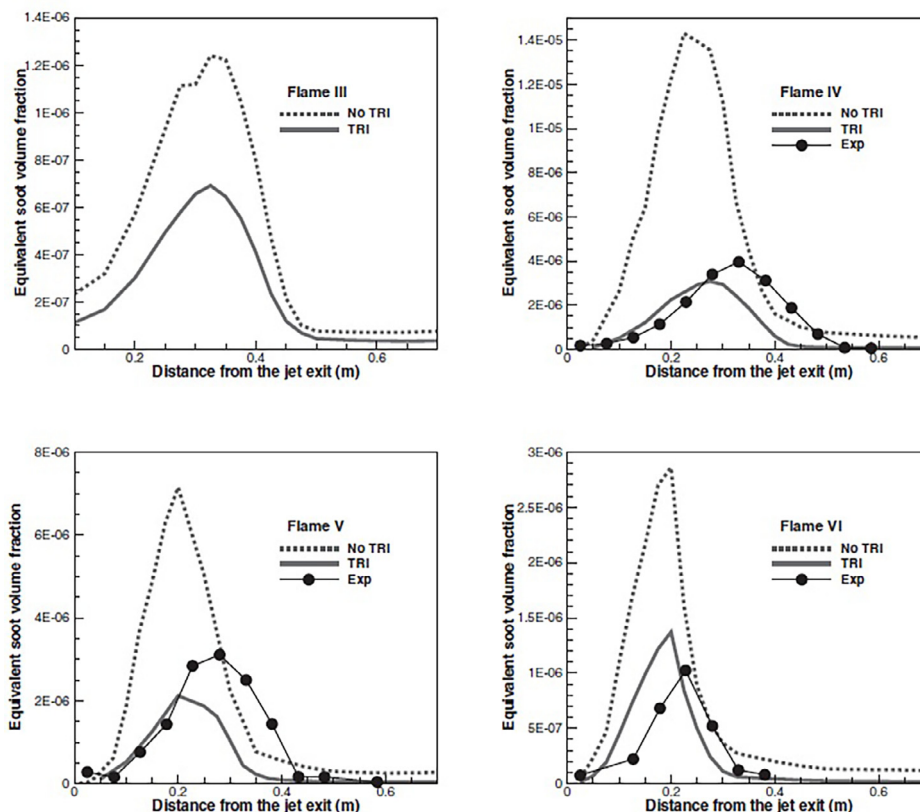


Fig. 7. Effects of TRI on equivalent soot volume fraction. Taken from Mehta et al. [162] (with permission).

turbulent kinetic energy was resolved. Nevertheless, it should be pointed out that soot was introduced by using an empirical correlation. Table 10 shows the radiant fractions for the 4D sooting flame. These radiant fractions were obtained using a frozen-field analysis (as indicated by the notation F). In this approach, all the statistics are derived from instantaneous data obtained from the FullTRI calculations (TRI4) once a statistically steady state is reached. The comparison of TRI1F and TRI0 quantifies the contribution of resolved emission TRI whereas the comparison of TRI3F and TRI2F quantifies that of SGS emission TRI. Results in Table 7 show that resolved emission TRI (TRI1F vs. TRI0) enhances  $\chi_R$  by 48.6% whereas SGS emission TRI (TRI3F vs. TRI2F) enhances  $\chi_R$  by 58.12%. As a consequence, both contributions appear to be significant with the contribution of SGS emission TRI exceeding that of resolved emission TRI. The contributions of resolved and SGS absorption TRI can be estimated from the comparison of TRI2F and TRI1F and TRI4F and TRI3F, respectively. Considering resolved absorption TRI (TRI2F vs. TRI1F) reduces  $\chi_R$  by about 6% whereas SGS absorption TRI (TRI4F vs. TRI3F) reduces  $\chi_R$  by about 1.5%. As expected, these results support the notion that absorption TRI can be reasonably ignored even in large-scale sooting flames whereas the contributions of SGS fluctuations to absorption TRI are negligible.

#### 4. Concluding remarks

Significant progress in soot formation modelling in laminar and turbulent jet diffusion flames has been made in the last three decades. The progress is made possible as a result of advances in all important aspects related to soot processes, such as gas-phase (including PAH) reaction mechanisms, soot kinetics (inception, surface growth, and oxidation), soot aerosol dynamics, non-gray radiation models, turbulence chemistry (including soot chemistry) interaction, and turbulence radiation interaction. Although the state-

of-the-art semi-empirical and detailed soot models are unable to predict the correct levels of soot volume fraction or the position of soot inception, these soot models are relatively robust as they can predict the qualitative soot distribution with the correct order-of-magnitude peak soot volume fraction. Accurate and efficient non-gray gas radiation models, such as the spectral-line based weight-sum-of-gray-gas models and the full-spectrum correlated-k models, can be readily coupled with the  $P_1$ ,  $P_3$ , and DOM/FVM solution methods to model radiative heat transfer, though uncertainty remains in the soot refractive index in the infrared spectrum.

Studies of soot formation modelling in laminar diffusion flames and laboratory scale turbulent jet diffusion flames of gaseous and vaporized liquid hydrocarbon fuels were reviewed with an emphasis on the importance of radiative heat transfer, radiation absorption, and turbulence radiation interaction in such important flames of fundamental interest and of close connection to the target diffusion flames of International Sooting Flame Workshop. Numerical studies of soot formation in laminar counterflow and coflow diffusion flames have concluded that radiation heat transfer is important and should always be taken into account and the simple optically thin approximation should be used with caution since it can potentially cause large error unless when the maximum flame optical thickness based on flame diameter integrated Planck mean absorption coefficient is sufficiently small ( $< 0.05$ ). Neglect radiation heat loss or radiation absorption has the largest influence on the predicted temperatures in the centerline region in the upper part of the flames and the predicted visible flame height mainly through its effect on soot oxidation. Turbulence radiation interaction in turbulent jet diffusion flames can significantly affect the predicted temperature and soot volume fraction and should therefore be properly modelled.

Although soot prediction is primarily affected by soot kinetic models, it can also be strongly influenced by soot aerosol dynamic

models and radiation heat transfer models when the flames are not sufficiently optically thin. It is therefore necessary to accurately model all important chemical and physical processes affecting soot prediction in hydrocarbon flames.

### Declaration of Competing Interest

The authors declare that they have no known competing financial interests or personal relationships that could have appeared to influence the work reported in this paper.

### References

- [1] International energy agency, key world energy statistics 2020 [online](2020).
- [2] J. Cinti, P. Holtberg, J. Diefenderfer, A. LaRose, J.T. Turnure, L. Westfall, International Energy Outlook 2016 with Projections to 2040, Technical Report, 2016.
- [3] T.C. Bond, S.J. Doherty, D.W. Fahey, P.M. Forster, T. Berntsen, et al., Bounding the role of black carbon in the climate system: a scientific assessment, *J. Geophys. Res.* 118 (2013) 5380–5552.
- [4] P. Desgroux, A. Faccinetto, X. Mercier, T. Mouton, D. Aubagnac, et al., Comparative study of the soot formation process in a “nucleation” and a “sooting” low pressure premixed methane flame, *Combust. Flame* 184 (2017) 153–166.
- [5] H. Wang, Formation of nascent soot and other condensed-phase materials in flames, *Proc. Combust. Inst.* 33 (2011) 41–67.
- [6] H.A. Michelsen, Probing soot formation, chemical and physical evolution, and oxidation: a review of in situ diagnostic techniques and needs, *Proc. Combust. Inst.* 37 (2017) 717–735.
- [7] J.W. Martin, M. Salamanca, M. Kraft, Soot inception: carbonaceous nanoparticle formation in flames, *Prog. Energy Combust. Sci.* 88 (2022) 100956.
- [8] A.E. Karataş, Ö.L. Gülder, Soot formation in high pressure laminar diffusion flames, *Prog. Energy Combust. Sci.* 38 (2012) 818–845.
- [9] K.P. Schug, Y. Mannheimer-Timnat, P. Yaccarino, I. Glassman, Sooting behavior of gaseous hydrocarbon diffusion flames and the influence of additives, *Combust. Sci. Technol.* 22 (1980) 235–250.
- [10] M.D. Smooke, M.B. Long, B.C. Connelly, M.B. Colket, R.J. Hall, Soot formation in laminar diffusion flames, *Combust. Flame* 143 (2005) 613–628.
- [11] Q. Zhang, H. Guo, F. Liu, G.J. Smallwood, M.J. Thomson, Modeling of soot aggregate formation and size distribution in a laminar ethylene/air coflow diffusion flame with detailed PAH chemistry and an advanced sectional aerosol dynamics model, *Proc. Combust. Inst.* 32 (2009) 761–768.
- [12] T. Blacha, M.D. Domenico, P. Gerlinger, M. Aigner, Soot predictions in premixed and non-premixed laminar flames using a sectional approach for PAHs and soot, *Combust. Flame* 159 (2012) 181–193.
- [13] A. Cuoci, A. Frassoldati, T. Faravelli, H. Jin, Y. Wang, K. Zhang, P. Glarborg, F. Qi, Experimental and detailed kinetic modeling study of PAH formation in laminar co-flow methane diffusion flames, *Proc. Combust. Inst.* 34 (2013) 1811–1818.
- [14] A. Abdelgadir, I.A. Rakha, S.A. Steinmetz, A. Attili, F. Bisetti, W.L. Roberts, Effects of hydrodynamics and mixing on soot formation and growth in laminar coflow diffusion flames at elevated pressures, *Combust. Flame* 181 (2017) 39–53.
- [15] International Sooting Flame (ISF) Workshop [online] (2019).
- [16] F. Liu, H. Guo, G.J. Smallwood, Ö.L. Gülder, Effects of gas and soot radiation on soot formation in a coflow laminar ethylene diffusion flame, *J. Quant. Spectrosc. Radiat. Transf.* 73 (2002) 409–421.
- [17] R. Demarco, F. Nmira, J.L. Consalvi, Influence of thermal radiation on soot production in laminar axisymmetric diffusion flames, *J. Quant. Spectrosc. Radiat. Transf.* 120 (2013) 52–69.
- [18] W. Kong, F. Liu, Numerical study of the effects of gravity on soot formation in laminar coflow methane/air diffusion flames under different air stream velocities, *Combust. Theory Model.* 13 (6) (2009) 993–1023.
- [19] R.P. Lindstedt, S.A. Louloudi, Joint-scalar transported PDF modeling of soot formation and oxidation, *Proc. Combust. Inst.* 30 (2005) 775–783.
- [20] L. Tian, M.A. Schiener, R.P. Lindstedt, Fully coupled sectional modelling of soot particle dynamics in a turbulent diffusion flame, *Proc. Combust. Inst.* 38 (2021) 1365–1373.
- [21] F. Liu, J.-L. Consalvi, P.J. Coelho, F. André, M. Gu, V. Solovjov, B.W. Webb, The impact of radiative heat transfer in combustion processes and its modeling - with a focus on turbulent flames, *Fuel* 281 (2020) 118555.
- [22] M.F. Modest, S. Mazumder, Radiative Heat Transfer, fourth ed., Academic Press, London, 2022.
- [23] M.F. Modest, D.C. Haworth, Radiative Heat Transfer in Turbulent Combustion Systems, Springer, Heidelberg, 2016.
- [24] P.J. Coelho, Numerical simulation of the interaction between turbulence and radiation in reactive flows, *Prog. Energy Combust. Sci.* 33 (2007) 311–383.
- [25] R. Viskanta, M.P. Mengüç, Radiation heat transfer in combustion systems, *Prog. Energy Combust. Sci.* 13 (1987) 97–160.
- [26] Y. Wang, S.H. Chung, Soot formation in laminar counterflow flames, *Prog. Energy Combust. Sci.* 74 (2019) 152–238.
- [27] A. D’Anna, Combustion-formed nanoparticles, *Proc. Combust. Inst.* 32 (2009) 593–613.
- [28] J. Appel, H. Bockhorn, M. Frenklach, Kinetic modeling of soot formation with detailed chemistry and physics: laminar premixed flames of C<sub>2</sub> hydrocarbons, *Combust. Flame* 121 (2000) 122–136.
- [29] M.E. Mueller, G. Blanquart, H. Pitsch, Hybrid method of moments for modeling soot formation and growth, *Combust. Flame* 156 (2009) 1143–1155.
- [30] Y. Wang, A. Raj, S.H. Chung, Soot modeling of counterflow diffusion flames of ethylene-based binary mixture fuels, *Combust. Flame* 162 (2015) 586–596.
- [31] N.A. Eaves, Q. Zhang, F. Liu, H. Guo, S.B. Dworkin, M.J. Thomson, Coflame: a refined and validated numerical algorithm for modeling sooting laminar coflow diffusion flames, *Comput. Phys. Commun.* 207 (2016) 464–477.
- [32] H. Sabbah, L. Biennier, S.J. Klippenstein, I.R. Sims, B.R. Rowe, Exploring the role of PAHs in the formation of soot: pyrene dimerization, *J. Phys. Chem. Lett.* 1 (19) (2010) 2962–2967.
- [33] Q. Mao, A.C.T. van Duin, K.H. Luo, Formation of incipient soot particles from polycyclic aromatic hydrocarbons: a ReaxFF molecular dynamics study, *Carbon* 121 (2017) 380–388.
- [34] M.R. Kholghy, G.A. Kelesidis, S.E. Pratsinis, Reactive polycyclic aromatic hydrocarbon dimerization drives soot nucleation, *Phys. Chem. Chem. Phys.* 20 (2018) 10926–10938.
- [35] M.R. Kholghy, N.A. Eaves, A. Veshkini, M.J. Thomson, The role of reactive PAH dimerization in reducing soot nucleation reversibility, *Proc. Combust. Inst.* 37 (2019) 1003–1011.
- [36] N.A. Eaves, S.B. Dworkin, M.J. Thomson, Assessing relative contributions of PAHs to soot mass by reversible heterogeneous nucleation and condensation, *Proc. Combust. Inst.* 36 (2017) 935–945.
- [37] K. Gleason, F. Carbone, A.J.S. B. D. Drollette, D.L. Plata, A. Gomez, Small aromatic hydrocarbons control the onset of soot nucleation, *Combust. flame* 223 (2021) 398–406.
- [38] K.O. Johansson, M.P. Head-Gordon, P.E. Schrader, K.R. Wilson, H.A. Michelsen, Resonance-stabilized hydrocarbon-radical chain reactions may explain soot inception and growth, *Science* 361 (2018) 997–1000.
- [39] Q. Mao, L. Cai, R. Langer, H. Pitsch, The role of resonance-stabilized radical chain reactions in polycyclic aromatic hydrocarbon growth: theoretical calculation and kinetic modeling, *Proc. Combust. Inst.* 38 (2021) 1459–1466.
- [40] M. Frenklach, Reaction mechanism of soot formation in flames, *Phys. Chem. Chem. Phys.* 4 (2002) 2028–2037.
- [41] H. Guo, F. Liu, G.J. Smallwood, Ö.L. Gülder, A numerical study of the influence of transport properties of inert diluents on soot formation in a coflow laminar ethylene/air diffusion flame, *Proc. Combust. Inst.* 29 (2002) 2359–2365.
- [42] J.P. Soussi, R. Demarco, J.-L. Consalvi, F. Liu, A. Fuentes, Influence of soot aging on soot production for laminar propane diffusion flames, *Fuel* 210 (2017) 472–481.
- [43] F. Liu, H. Guo, G.J. Smallwood, Ö.L. Gülder, Numerical modelling of soot formation and oxidation in laminar coflow non-smoking and smoking ethylene diffusion flames, *Combust. Theor. Model.* 7 (2003) 301–315.
- [44] A. Khosousi, S.B. Dworkin, Detailed modelling of soot oxidation by O<sub>2</sub> and OH in laminar diffusion flames, *Proc. Combust. Inst.* 35 (2015) 1903–1910.
- [45] K.M. Leung, R.P. Lindstedt, W.P. Jones, A simplified reaction mechanism for soot formation in nonpremixed flames, *Combust. Flame* 87 (1991) 289–305.
- [46] H.G. Wagner, Soot formation in combustion, *Proc. Combust. Inst.* 17 (1979) 3–19.
- [47] S.J. Harris, A.M. Weiner, Surface growth of soot particles in premixed ethylene/air flames, *Combust. Sci. Technol.* 31 (3–4) (1983) 155–167.
- [48] M. Fairweather, W.P. Jones, R.P. Lindstedt, Predictions of radiative transfer from a turbulent reacting jet in a cross-wind, *Combust. Flame* 89 (1992) 45–63.
- [49] F. Liu, K.A. Thomson, H. Guo, G.J. Smallwood, Numerical and experimental study of an axisymmetric coflow laminar methane-air diffusion flame at pressures between 5 and 40 atmospheres, *Combust. Flame* 146 (2006) 456–471.
- [50] M. Frenklach, H. Wang, Detailed modeling of soot particle nucleation and growth, *Proc. Combust. Inst.* 23 (1) (1990) 1559–1566.
- [51] K.B. Lee, M.W. Thring, J.M. Beér, On the rate of combustion of soot in a laminar soot flame, *Combust. Flame* 8 (1962) 437–443.
- [52] J.B. Moss, C.D. Stewart, K.J. Young, Modeling soot formation and burnout in a high temperature laminar diffusion flame burning under oxygen-enriched conditions, *Combust. Flame* 101 (1995) 491–500.
- [53] D. Bradley, G. Dixon-Lewis, S.E. Habik, E.M.J. Mushi, The oxidation of graphite power in flame reaction zones, *Proc. Combust. Inst.* 20 (1984) 931–940.
- [54] M.A. Schiener, R.P. Lindstedt, Joint-scalar transported PDF modelling of soot in a turbulent non-premixed natural gas flame, *Combust. Theor. Model.* 22 (2018) 1134–1175.
- [55] F. Liu, H. Guo, G.J. Smallwood, M.E. Hafi, Effects of gas and soot radiation on soot formation in counterflow ethylene diffusion flames, *J. Quant. Spectrosc. Radiat. Transf.* 84 (2004) 501–511.
- [56] H. Guo, F. Liu, G.J. Smallwood, Soot and NO formation in counterflow ethylene/oxygen/nitrogen diffusion flames, *Combust. Theor. Model.* 8 (2004) 475–489.
- [57] I. Hernández, G. Lecocq, D. Poitou, E. Riber, B. Cuenot, Computations of soot formation in ethylene/air counterflow diffusion flames and its interaction with radiation, *C. R. Mecanique* 341 (2013) 238–246.
- [58] I.M. Kennedy, C. Yam, D.C. Rapp, R.J. Santoro, Modeling and measurements of soot and species in a laminar diffusion flame, *Combust. Flame* 107 (1996) 368–382.

- [59] H. Guo, F. Liu, G.J. Smallwood, Ö.L. Gülder, The flame preheating effect on numerical modelling of soot formation in a two-dimensional laminar ethylene-air diffusion flame, *Combust. Theory Model.* 6 (2002) 173–187.
- [60] Q. Zhang, H. Guo, F. Liu, G.J. Smallwood, M.J. Thomson, Implementation of an advanced fixed sectional aerosol dynamics model with soot aggregate formation in a laminar methane/air coflow diffusion flame, *Combust. Theory Model.* 12 (4) (2008) 621–641.
- [61] M.R.J. Charest, H.I. Joo, Ö.L. Gülder, C.P.T. Groth, Experimental and numerical study of soot formation in laminar ethylene diffusion flames at elevated pressures from 10 to 35 atm, *Proc. Combust. Inst.* 33 (2011) 549–557.
- [62] M.R.J. Charest, Ö.L. Gülder, C.P.T. Groth, Numerical and experimental study of soot formation in laminar diffusion flames burning simulated biogas fuels at elevated pressures, *Combust. Flame* 161 (2014) 2678–2691.
- [63] P. Akridis, S. Rigopoulos, Modelling of soot formation in laminar diffusion flames using a comprehensive CFD-PBE model with detailed gas-phase chemistry, *Combust. Theory Model.* 21 (1) (2017) 35–48.
- [64] J.A.R. Sarr, C.P.T. Groth, J.C.T. Hu, A maximum entropy-inspired interpolative closure for the prediction of radiative heat transfer in laminar co-flow diffusion flames, *Combust. Sci. Technol.* 194 (1) (2022) 45–79.
- [65] S.J. Brookes, J.B. Moss, Predictions of soot and thermal radiation properties in confined turbulent jet diffusion flames, *Combust. Flame* 116 (1999) 486–503.
- [66] G. Ma, Z. Wen, M.F. Lightstone, M.J. Thomson, Optimization of soot modeling in turbulent nonpremixed ethylene/air jet flames, *Combust. Sci. Technol.* 177 (2005) 1567–1602.
- [67] M. Bolla, D. Farrace, Y.M. Wright, K. Boulouchos, E. Mastorakos, Influence of turbulence-chemistry interaction for n-heptane spray combustion under diesel engine conditions with emphasis on soot formation and oxidation, *Combust. Theory Model.* 18 (2014) 330–360.
- [68] S.F. Fernandez, C. Paul, A. Sircar, A. Imren, D.C. Haworth, S. Roy, M.F. Modest, Soot and spectral radiation modeling for high-pressure turbulent spray flames, *Combust. Flame* 190 (2018) 402–415.
- [69] H. Guo, F. Liu, G.J. Smallwood, Ö.L. Gülder, Numerical study on the influence of hydrogen addition on soot formation in a laminar ethylene-air diffusion flame, *Combust. Flame* 145 (2006) 324–338.
- [70] R.P. Lindstedt, Simplified soot nucleation and surface growth steps for non-premixed flames, in: H. Bockhorn (Ed.), *Soot Formation in Combustion*, vol. 59, Springer Ser. Chem. Phys. (1994), pp. 417–441.
- [71] R.J. Hall, M.D. Smooke, M.B. Colket, Predictions of soot dynamics in opposed jet diffusion flames, in: R.F. Sawyer, F.L. Dryer (Eds.), *Physical and Chemical Aspects of Combustion: A Tribute to Irvin Glassman*, Combustion Science and Technology Book Series, Gordon and Breach, Amsterdam (1997), pp. 189–230.
- [72] M.D. Smooke, C.S. McEnally, L.D. Pfefferle, R.J. Hall, M.B. Colket, Computational and experimental study of soot formation in a coflow, laminar diffusion flame, *Combust. Flame* 117 (1999) 117–139.
- [73] Z. Wen, S. Yun, M.J. Thomson, M.F. Lightstone, Modeling soot formation in turbulent kerosene/air jet diffusion flames, *Combust. Flame* 135 (2003) 323–340.
- [74] A. Beltrame, P. Porshnev, V. Merchan-Merchan, A. Saveliev, A. Fridman, L.A. Kennedy, O. Petrova, S. Zhdanok, F. Amouri, O. Charon, Soot and NO formation in methane-oxygen enriched diffusion flames, *Combust. Flame* 124 (2001) 295–310.
- [75] J.-L. Consalvi, F. Nmira, D. Burot, Simulations of sooting turbulent jet flames using a hybrid flamelet/stochastic Eulerian field method, *Combust. Theory Model.* 20 (2016) 221–257.
- [76] M.R. Busupally, A. De, Numerical modeling of soot formation in a turbulent C<sub>2</sub>H<sub>4</sub>/air diffusion flame, *Int. J. Spray Combust. Dyn.* 8 (2) (2016) 67–85.
- [77] M.D. Smooke, R.J. Hall, M.B. Colket, J. Fielding, M.B. Long, C.S. McEnally, L.D. Pfefferle, Investigation of the transition from lightly sooting towards heavily sooting co-flow ethylene diffusion flames, *Combust. Theory Model.* 8 (2004) 593–606.
- [78] M.B. Colket, R.J. Hall, Successes and uncertainties in modeling soot formation in laminar, premixed flames, in: H. Bockhorn (Ed.), *Soot Formation in Combustion*, vol. 59, Springer Ser. Chem. Phys. (1994), pp. 442–468.
- [79] M. Frenklach, H. Wang, Detailed mechanism and modeling of soot particle formation, in: H. Bockhorn (Ed.), *Soot Formation in Combustion*, vol. 59, Springer Ser. Chem. Phys. (1994), pp. 165–192.
- [80] G. Blanquart, H. Pitsch, A joint volume-surface-hydrogen multi-variate model for soot formation, in: H. Bockhorn, A. D'Anna, A.F. Sarofim, H. Wang (Eds.), *Combustion Generated Fine Carbonaceous Particles*, Springer-Verlag, KIT Scientific Publishing (2009), pp. 437–464.
- [81] Q. Zhang, Detailed Modeling of Soot Formation/Oxidation in Laminar Coflow Diffusion Flames, University of Toronto, 2009 Ph.D. thesis.
- [82] A.M. El-Leathy, C.H. Kim, G.M. Faeth, Soot surface reactions in high-temperature laminar diffusion flames, *AIAA J.* 42 (2004) 988–996.
- [83] J. Singh, M. Balthasar, M. Kraft, W. Wagner, Stochastic modeling of soot particle size and age distributions in laminar premixed flames, *Proc. Combust. Inst.* 30 (2005) 1457–1465.
- [84] A. Veshkini, S.B. Dworkin, M.J. Thomson, A soot particle surface reactivity model applied to a wide range of laminar ethylene/air flames, *Combust. Flame* 161 (2014) 3191–3200.
- [85] M. Gu, F. Liu, J.L. Consalvi, Ö.L. Gülder, Effects of pressure on soot formation in laminar coflow methane/air diffusion flames doped with n-heptane and toluene between 2 and 8 atm, *Proc. Combust. Inst.* 38 (2021) 1403–1412.
- [86] F. Liu, X. He, X. Ma, Q. Zhang, M.J. Thomson, H. Guo, G.J. Smallwood, S. Shuai, J. Wang, An experimental and numerical study of the effects of dimethyl ether addition to fuel on polycyclic aromatic hydrocarbon and soot formation in laminar coflow ethylene/air diffusion flames, *Combust. Flame* 158 (2011) 547–563.
- [87] M. Gu, H. Chu, F. Liu, Effects of simultaneous hydrogen enrichment and carbon dioxide dilution of fuel on soot formation in an axisymmetric coflow laminar ethylene/air diffusion flame, *Combust. Flame* 166 (2016) 216–228.
- [88] F. Liu, J.-L. Consalvi, A. Fuentes, Effects of water vapor addition to the air stream on soot formation and flame properties in a laminar coflow ethylene/air diffusion flame, *Combust. Flame* 161 (2014) 1724–1734.
- [89] F. Liu, Y. Ai, W. Kong, Effect of hydrogen and helium addition to fuel on soot formation in an axisymmetric coflow laminar methane/air diffusion flame, *Int. J. Hydrogen Energy* 39 (2014) 3936–3946.
- [90] J.-L. Consalvi, F. Liu, J. Contreras, M. Kashif, G. Legros, Numerical study of soot formation in laminar coflow diffusion flames of methane doped with primary reference fuels, *Combust. Flame* 162 (2015) 1153–1163.
- [91] J.-L. Consalvi, F. Nmira, Absorption turbulence-radiation interactions in sooting turbulent jet flames, *J. Quant. Spectrosc. Radiat. Transf.* 201 (2017) 1–9.
- [92] F. Liu, A.E. Karataş, Ö.L. Gülder, M. Gu, Numerical and experimental study of the influence of CO<sub>2</sub> and N<sub>2</sub> dilution on soot formation in laminar coflow C<sub>2</sub>H<sub>4</sub>/air diffusion flames at pressures between 5 and 20 atm, *Combust. Flame* 162 (2015) 2231–2247.
- [93] J.-L. Consalvi, F. Liu, M. Kashif, G. Legros, Numerical study of soot formation in laminar coflow methane/air diffusion flames doped by n-heptane/toluene and iso-octane/toluene blends, *Combust. Flame* 180 (2017) 167–174.
- [94] S.B. Dworkin, Q. Zhang, M.J. Thomson, N.A. Slavinskaya, U. Riedel, Application of an enhanced PAH growth model to soot formation in a laminar coflow ethylene/air diffusion flame, *Combust. Flame* 158 (2011) 1682–1695.
- [95] H.B. Zhang, D. Hou, C.K. Law, X. You, The role of carbon-addition and hydrogen-migration reactions in soot surface growth, *J. Phys. Chem. A* 120 (5) (2016) 683–689.
- [96] M. Frenklach, R.I. Singh, A.M. Mebel, On the low-temperature limit of HACA, *Proc. Combust. Inst.* 37 (2019) 969–976.
- [97] C. Zhang, L. Chen, S. Ding, H. Xu, G. Li, J.-L. Consalvi, F. Liu, Effects of soot inception and condensation PAH species and fuel preheating on soot formation modeling in laminar coflow CH<sub>4</sub>/air diffusion flames doped with n-heptane/toluene mixtures, *Fuel* 253 (2019) 1371–1377.
- [98] J.Y. Xing, C.P.T. Groth, Assessment of PAH-based precursor models using a seven-moment quadrature-based closure for soot formation prediction in non-premixed laminar flames, *AIAA SCITECH Forum AIAA 2022–2253*.
- [99] N.A. Eaves, S.B. Dworkin, M.J. Thomson, The importance of reversibility in modeling soot nucleation and condensation processes, *Proc. Combust. Inst.* 35 (2015) 1787–1794.
- [100] H.A. Michelsen, M.B. Colket, P.E. Bengtsson, A. D'Anna, P. Desgroux, et al., A review of terminology used to describe soot formation and evolution under combustion and pyrolytic conditions, *ACS Nano* 14 (2020) 12470–12490.
- [101] X. López-Yglesias, P.E. Schrader, H.A. Michelsen, Soot maturity and absorption cross sections, *J. Aerosol Sci.* 75 (2014) 43–64.
- [102] M. Mannazhi, S. Török, J. Gao, P.E. Bengtsson, Soot maturity studies in methane-air diffusion flames at elevated pressures using laser-induced incandescence, *Proc. Combust. Inst.* 38 (2021) 1217–1224.
- [103] J. Yon, J.J. Cruz, F. Escudero, J. Morán, F. Liu, A. Fuentes, Revealing soot maturity based on multi-wavelength absorption/emission measurements in laminar axisymmetric coflow ethylene diffusion flames, *Combust. Flame* 227 (2021) 147–161.
- [104] M.R. Kholghy, A. Veshkini, M.J. Thomson, The core-shell internal nanostructure of soot—A criterion to model soot maturity, *Carbon* 100 (2016) 508–536.
- [105] G.A. Kelesidis, E. Goudeli, S.E. Pratsinis, Morphology and mobility diameter of carbonaceous aerosols during agglomeration and surface growth, *Carbon* 121 (2017) 527–535.
- [106] J. Morán, A. Poux, J. Yon, Impact of the competition between aggregation and surface growth on the morphology of soot particles formed in an ethylene laminar premixed flame, *J. Aerosol Sci.* 152 (2021) 105690.
- [107] Y. Sung, V. Raman, H. Koo, M. Metha, R.O. Fox, Large-eddy simulation modeling of turbulent flame synthesis of Titania nanoparticles using a bivariate particle description, *AIChE J.* 60 (2) (2014) 459–472.
- [108] J.Y. Xing, C.P.T. Groth, J.C.T. Hu, On the use of fractional-order quadrature-based moment closures for predicting soot formation in laminar flames, *Combust. Sci. Technol.* 194 (1) (2022) 22–44.
- [109] S. Rigopoulos, Modelling of soot aerosol dynamics in turbulent flow, *Flow, Turbul. Combust.* 103 (2019) 565–604.
- [110] S. Trottier, H. Guo, G.J. Smallwood, M.R. Johnson, Measurement and modeling of the sooting propensity of binary fuel mixtures, *Proc. Combust. Inst.* 31 (2007) 611–619.
- [111] M. Frenklach, Method of moments with interpolative closure, *Chem. Eng. Sci.* 57 (12) (2002) 2229–2239.
- [112] A. Kazakov, M. Frenklach, Dynamic modelling of soot particle coagulation and aggregation: implementation with the method of moments and application to high-pressure laminar premixed flames, *Combust. Flame* 114 (1998) 484–501.
- [113] Ü.Ö. Köylü, G.M. Faeth, Structure of overfire soot in buoyant turbulent diffusion flames at long residence times, *Combust. Flame* 89 (1992) 140–156.
- [114] H.M.F. Amin, A. Bennett, W.L. Roberts, Determining fractal properties of soot aggregates and primary particle size distribution in counterflow flames up to 10 atm, *Proc. Combust. Inst.* 37 (2019) 1161–1168.
- [115] B. Gigone, A.E. Karataş, Ö.L. Gülder, Soot aggregate morphology in coflow laminar ethylene diffusion flames at elevated pressures, *Proc. Combust. Inst.* 37 (2019) 841–848.

- [116] A.E. Karataş, B. Gigone, Ö.L. Gülder, Soot aggregate morphology deduced from thermophoretic sampling in coflow laminar methane diffusion flames at pressures up to 30 atm, *Combust. Flame* 222 (2020) 411–422.
- [117] Q. Zhang, M.J. Thomson, H. Guo, F. Liu, G.J. Smallwood, A numerical study of soot aggregate formation in a laminar coflow diffusion flame, *Combust. Flame* 156 (2009) 697–705.
- [118] K. Netzell, H. Lehtiniemi, F. Mauss, Calculating the soot particle size distribution function in turbulent diffusion flames using a sectional method, *Proc. Combust. Inst.* 31 (2007) 667–674.
- [119] P. Rodrigues, B. Franzelli, R. Vicquelin, O.N. Darabiha, Coupling an LES approach and a soot sectional model for the study of sooting turbulent non-premixed flames, *Combust. Flame* 190 (2018) 477–499.
- [120] J.S. Bhatt, R.P. Lindstedt, Analysis of the impact of agglomeration and surface chemistry models on soot formation and oxidation, *Proc. Combust. Inst.* 32 (2009) 713–720.
- [121] D.O. Lignell, J.H. Chen, P.J. Smith, T. Lu, C.K. Law, The effect of flame structure on soot formation and transport in turbulent nonpremixed flames using direct numerical simulation, *Combust. Flame* 151 (2007) 2–28.
- [122] D.O. Lignell, J.H. Chen, P.J. Smith, Three-dimensional direct numerical simulation of soot formation and transport in a temporally evolving nonpremixed ethylene jet flame, *Combust. Flame* 155 (2008) 316–333.
- [123] F. Bisetti, G. Blanquart, M.E. Mueller, H. Pitsch, On the formation and early evolution of soot in turbulent nonpremixed flames, *Combust. Flame* 159 (2012) 317–335.
- [124] A. Attili, F. Bisetti, M.E. Mueller, H. Pitsch, Formation, growth, and transport of soot in a three-dimensional turbulent non-premixed jet flame, *Combust. Flame* 161 (2014) 1849–1865.
- [125] A. Attili, F. Bisetti, M.E. Mueller, H. Pitsch, Damköhler number effects on soot formation and growth in turbulent nonpremixed flames, *Proc. Combust. Inst.* 35 (2015) 1215–1223.
- [126] P. Narayanan, A. Trounev, Radiation-driven flame weakening effects in sooting turbulent diffusion flames, *Proc. Combust. Inst.* 32 (2009) 1481–1489.
- [127] S.Y. Lee, S.R. Turns, R.J. Santoro, Measurements of soot, OH, and PAH concentrations in turbulent ethylene/air jet flames, *Combust. Flame* 156 (2009) 2264–2275.
- [128] S.M. Mahmoud, G.J. Nathan, Z.T. Alwahabi, Z.W. Sun, P.R. Medwell, B.B. Dally, The effect of exit strain rate on soot volume fraction in turbulent non-premixed jet flames, *Proc. Combust. Inst.* 36 (2017) 889–897.
- [129] O. Park, R.A. Burns, O.R.H. Buxton, N.T. Clemens, Mixture fraction, soot volume fraction, and velocity imaging in the soot-inception region of a turbulent non-premixed jet flame, *Proc. Combust. Inst.* 36 (2017) 899–907.
- [130] S. Kruse, J. Ye, Z. Sun, A. Attili, B. Dally, P. Medwell, H. Pitsch, Experimental investigation of soot evolution in a turbulent non-premixed prevaporized toluene flame, *Proc. Combust. Inst.* 37 (2019) 849–857.
- [131] M.E. Mueller, H. Pitsch, LES model for sooting turbulent nonpremixed flames, *Combust. Flame* 159 (2012) 2166–2180.
- [132] S. Navarro-Martinez, S. Rigopoulos, Differential diffusion modelling in LES with RCCE-reduced chemistry, *Flow, Turbul. Combust.* 89 (2012) 311–328.
- [133] S. Yang, J.K. Lew, M.E. Mueller, Large eddy simulation of soot evolution in turbulent reacting flows: presumed subfilter PDF model for soot-turbulence-chemistry interactions, *Combust. Flame* 209 (2019) 200–213.
- [134] F. Nmira, A. Bouffard, J.-L. Consalvi, Y. Wang, Large-eddy simulation of lab-scale ethylene buoyant diffusion flames: effects of subgrid turbulence/soot production interaction and radiation models, *Proc. Combust. Inst.* 39 (2022) 1–8.
- [135] P. Donde, V. Raman, M.E. Mueller, H. Pitsch, LES/PDF based modeling of soot-turbulence interactions in turbulent flames, *Proc. Combust. Inst.* 34 (2013) 1183–1192.
- [136] A. Jain, D.D. Das, C.S. McEnally, L.D. Pfefferle, Y. Xuan, Experimental and numerical study of variable oxygen index effects on soot yield and distribution in laminar co-flow diffusion flames, *Proc. Combust. Inst.* 37 (2019) 859–867.
- [137] A. Kronenburg, R.W. Bilger, J.H. Kent, Modeling soot formation in turbulent methane-air jet diffusion flames, *Combust. Flame* 121 (2000) 24–40.
- [138] S.P. Kearney, D.R. Guildenbecher, C. Winters, P.A. Farias, T.W. Grasser, J.C. Hewson, Temperature, oxygen, and soot-volume-fraction measurements in a turbulent C<sub>2</sub>H<sub>4</sub>-fueled jet flame, Technical Report, In: SANDIA report Sand2015-7968, 2015.
- [139] H. Pitsch, E. Riesmeier, N. Peters, Unsteady flamelet modeling of soot in turbulent diffusion flames, *Combust. Sci. Technol.* 158 (2000) 389–406.
- [140] M.E. Mueller, H. Pitsch, Large eddy simulation subfilter modeling of soot-turbulence interactions, *Phys. Fluids* 23 (2011) 115104.
- [141] L. Berger, A. Wick, A. Attili, M.E. Mueller, H. Pitsch, Modeling subfilter soot-turbulence interactions in large eddy simulation: an a priori study, *Proc. Combust. Inst.* 38 (2021) 2783–2790.
- [142] M. Ihme, H. Pitsch, Modeling of radiation and nitric oxide formation in turbulent nonpremixed flames using a flamelet/progress variable formulation, *Phys. Fluids* 20 (2008) 055110.
- [143] Y. Xuan, G. Blanquart, A flamelet-based a priori analysis on the chemistry tabulation of polycyclic aromatic hydrocarbons in non-premixed flames, *Combust. Flame* 161 (2014) 1516–1525.
- [144] Y. Xuan, G. Blanquart, Effects of aromatic chemistry-turbulence interactions on soot formation in a turbulent non-premixed flame, *Proc. Combust. Inst.* 35 (2015) 1911–1919.
- [145] R.S. Mehta, D.C. Haworth, M.F. Modest, Composition PDF/photon Monte Carlo modeling of moderately sooting turbulent jet flames, *Combust. Flame* 157 (2010) 982–994.
- [146] M.A. Schiener, R.P. Lindstedt, Transported probability density function based modelling of soot particle size distributions in non-premixed turbulent jet flames, *Proc. Combust. Inst.* 37 (2019) 1049–1056.
- [147] Z. Huo, M.J. Cleary, A.R. Masri, M.E. Mueller, A coupled MMC-LES and sectional kinetic scheme for soot formation in a turbulent flame, *Combust. Flame* 241 (2022) 112089.
- [148] D.C. Haworth, Progress in probability density function methods for turbulent reacting flows, *Prog. Energy Combust. Sci.* 36 (2010) 168–259.
- [149] I.M. Aksit, J.B. Moss, A hybrid scalar model for sooting turbulent flames, *Combust. Flame* 145 (2006) 231–244.
- [150] J.-L. Consalvi, F. Nmira, Transported scalar PDF modeling of oxygen-enriched turbulent jet diffusion flames: soot production and radiative heat transfer, *Fuel* 178 (2016) 37–48.
- [151] H.Z. Zhou, T. Yang, E.R. Hawkes, Z. Ren, H. Wang, A. Wehrfritz, An evaluation of gas-phase micro-mixing models with differential mixing timescales in transported PDF simulations of sooting flame DNS, *Proc. Combust. Inst.* 38 (2021) 2731–2739.
- [152] Yunardi, R.M. Woolley, M. Fairweather, Conditional moment closure prediction of soot formation in turbulent, nonpremixed ethylene flames, *Combust. Flame* 152 (2008) 360–376.
- [153] S.J. Brookes, J.B. Moss, Measurements of soot production and thermal radiation from confined turbulent jet diffusion flames of methane, *Combust. Flame* 116 (1999) 49–61.
- [154] <http://combustion.berkeley.edu/gri-mech/releases.html> [online]
- [155] F. Mauss, Entwicklung eines Kinetischen Modells der Rubildung mit Schneller Polymerisation, RWTH Aachen, 1998 Ph.D. thesis.
- [156] J.H. Kent, D. Honnery, Modeling sooting turbulent jet flames using an extended flamelet technique, *Combust. Sci. Technol.* 54 (1987) 383–397.
- [157] A. Coppalle, D. Joyeux, Temperature and soot volume fraction in turbulent diffusion flames: measurements of mean and fluctuating values, *Combust. Flame* 96 (1994) 275–285.
- [158] L. Wang, D.C. Haworth, S.R. Turns, M.F. Modest, Interactions among soot, thermal radiation, and NO<sub>x</sub> emissions in oxygen-enriched turbulent nonpremixed flames: a computational fluid dynamics modeling study, *Combust. Flame* 141 (2005) 170–179.
- [159] L. Wang, N.E. Endrud, S.R. Turns, M.D. D'Agostini, A.G. Slavejkov, A study of the influence of oxygen index on soot radiation and emission characteristics of turbulent jet flames, *Combust. Sci. Technol.* 174 (2002) 45–72.
- [160] H. Wang, M. Frenklach, A detailed kinetic modeling study of aromatics formation in laminar premixed acetylene and ethylene flames, *Combust. Flame* 110 (1997) 173–221.
- [161] Z. Qin, V.V. Lissianski, H. Yang, W.C. Gardiner, S.G. Scott, H. Wang, Combustion chemistry of propane: a case study of detailed reaction mechanism optimization, *Proc. Combust. Inst.* 28 (2000) 1663–1669.
- [162] R.S. Mehta, M.F. Modest, D.C. Haworth, Radiation characteristics and turbulence-radiation interactions in sooting turbulent jet flames, *Combust. Theory Model.* 14 (2010) 105–124.
- [163] G. Blanquart, P. Peipot-Desjardins, H. Pitsch, Chemical mechanism for high temperature combustion of engine relevant fuels with emphasis on soot precursors, *Combust. Flame* 156 (2009) 588–607.
- [164] K. Narayanaswamy, G. Blanquart, H. Pitsch, A consistent chemical mechanism for oxidation of substituted aromatic species, *Combust. Flame* 157 (2010) 1879–1898.
- [165] N.H. Qamar, Z.T. Alwahabi, Q.N. Chan, G.J. Nathan, D. Roekaerts, K.D. King, Soot volume fraction in a piloted turbulent jet non-premixed flame of natural gas, *Combust. Flame* 156 (2009) 1339–1347.
- [166] V. Sick, F. Hildenbrand, R.P. Lindstedt, Quantitative laser-based measurements and detailed chemical kinetic modeling of nitric oxide concentrations in methane-air counterflow diffusion flames, *Proc. Combust. Inst.* 27 (1998) 1401–1409.
- [167] A. Gupta, D.C. Haworth, M.F. Modest, Turbulence-radiation interactions in large-eddy simulations of luminous and nonluminous nonpremixed flames, *Proc. Combust. Inst.* 34 (2013) 1281–1288.
- [168] S. James, M.S. Anand, M.K. Razdan, S.B. Pope, In situ detailed chemistry calculations in combustor flow analyses, *J. Eng. Gas Turbines Power* 132 (2001) 747–756.
- [169] G. Pal, A. Gupta, M.F. Modest, D.C. Haworth, Comparison of accuracy and computational expense if radiation models in simulation of non-remixed turbulent jet flames, *Combust. Flame* 162 (2015) 2487–2495.
- [170] P. Rodrigues, O. Gicquel, B. Franzelli, N. Darabiha, R. Vicquelin, Analysis of radiative transfer in a turbulent sooting jet flame using a Monte Carlo method coupled to a large eddy simulation, *J. Quant. Spectrosc. Radiat. Transf.* 235 (2019) 187–203.
- [171] Y. Wang, A. Raj, S.H. Chung, A PAH growth mechanism and synergistic effect on PAH formation in counterflow diffusion flames, *Combust. Flame* 160 (2013) 1667–1676.
- [172] F. Sewerin, S. Rigopoulos, An LES-PBE-PDF approach for predicting the soot particle size distribution in turbulent flames, *Combust. Flame* 189 (2018) 62–76.
- [173] G. Blanquart, <http://www.theforce.caltech.edu/caltechmech/> [online]
- [174] W. Boyette, S. Chowdhury, W. Roberts, Soot particle size distribution functions in a turbulent non-premixed ethylene-nitrogen flame, *Flow, Turbul. Combust.* 98 (2017) 1173–1186.
- [175] S. Chowdhury, W.R. Boyette, W.L. Roberts, Time-averaged probability density functions of soot nanoparticles along the centerline of a piloted turbulent

- diffusion flame using a scanning mobility particle sizer, *J. Aerosol Sci.* 106 (2017) 56–67.
- [176] N. Slavinskaya, P. Frank, A modelling study of aromatic soot precursors formation in laminar methane and ethene flames, *Combust. Flame* 156 (2009) 1705–1722.
- [177] M. Grader, C. Eberle, P. Gerlinger, Large-eddy simulation and analysis of a sooting lifted turbulent jet flame, *Combust. Flame* 215 (2020) 458–470.
- [178] M. Köhler, I. Boxx, K.P. Geigle, W. Meier, Simultaneous planar measurements of soot structure and velocity fields in a turbulent lifted jet flame at 3 kHz, *Appl. Phys. B* 103 (2011) 271–279.
- [179] M. Köhler, K.P. Geigle, W. Meier, B.M. Crosland, K.A. Thomson, G.J. Smallwood, Sooting turbulent jet flame: characterization and quantitative soot measurements, *Appl. Phys. B* 104 (2011) 409–442.
- [180] M. Köhler, K.P. Geigle, T. Blacha, P. Gerlinger, W. Meier, Experimental characterization and numerical simulation of a sooting lifted turbulent jet diffusion flame, *Combust. Flame* 159 (2012) 2620–2635.
- [181] B. Wu, S.P. Roy, X. Zhao, Detailed modeling of a small-scale turbulent pool fire, *Combust. Flame* 214 (2020) 224–237.
- [182] M. Klassen, Y.R. Sivathanu, J.P. Gore, Simultaneous emission absorption measurements in toluene-fueled pool flames: mean and RMS properties, *Combust. Flame* 90 (1992) 34–44.
- [183] Z. Huo, M.J.C.M. Sirignano, A.R. Masri, A sectional soot formation kinetics scheme with a new model for coagulation efficiency, *Combust. Flame* 221 (2021) 111444.
- [184] G. Xiong, D. Zeng, P.P. Panda, Y. Wang, Laser induced incandescence measurement of soot in ethylene buoyant turbulent diffusion flames under normal and reduced oxygen concentrations, *Combust. Flame* 230 (2021) 111456.
- [185] M. Ihme, W.T. Chung, A.A. Mishra, Combustion machine learning: principles, progress and prospects, *Prog. Energy Combust. Sci.* 91 (2022) 101010.
- [186] R. Alexander, S. Bozorgzadeh, A. Khosousi, S.B. Dworkin, Development and testing of a soot particle concentration estimator using Lagrangian post processing, *Eng. Appl. Comput. Fluid Dyn.* 12 (2018) 236–249.
- [187] L. Zimmer, S. Kostic, S.B. Dworkin, A novel soot concentration field estimator applied to sooting ethylene/air laminar flames, *Eng. Appl. Comput. Fluid Dyn.* 13 (2019) 470–481.
- [188] M. Jadidi, S. Kostic, L. Zimmer, S.B. Dworkin, An artificial neural network for the low-cost prediction of soot emissions, *Energies* 13 (2020) 4787.
- [189] M. Jadidi, L.D. Liddo, S.B. Dworkin, A long short-term memory neural network for the low-cost prediction of soot concentration in a time-dependent flame, *Energies* 14 (2021) 1394.
- [190] L.D. Liddo, J.C. Saldinger, M. Jadidi, P. Elvati, A. Violi, S.B. Dworkin, Exploring soot inception rate with stochastic modelling and machine learning, *Combust. Flame* (2023) 112375.
- [191] J.Y. Lai, P. Elvati, A. Violi, Stochastic atomistic simulation of polycyclic aromatic hydrocarbon growth in combustion, *Phys. Chem. Chem. Phys.* 16 (2014) 7969–7979.
- [192] A. Seltz, P. Domingo, Vervisch, Luc, Solving the population balance equation for non-inertial particles dynamics using probability density function and neural networks: application to a sooting flame, *Phys. Fluids* 33 (2021) 013311.
- [193] M. Cailler, N. Darabiha, D. Veynante, B. Fiorina, Building-up virtual optimized mechanism for flame modeling, *Proc. Combust. Inst.* 37 (2017) 1251–1258.
- [194] M. Cailler, N. Darabiha, B. Fiorina, Development of a virtual optimized chemistry method, application to hydrocarbon/air combustion, *Combust. Flame* 211 (2020) 281–302.
- [195] H.M. Colmán, A. Cuoci, N. Darabiha, B. Fiorina, A virtual chemistry model for soot prediction in flames including radiative heat transfer, *Combust. Flame* 238 (2022) 111879.
- [196] H.M. Colmán, N. Darabiha, D. Veynante, B. Fiorina, Turbulent combustion model for soot formation at the LES subgrid-scale using virtual chemistry approach, *Combust. Flame* 247 (2023) 112496.
- [197] C. Saggese, S. Ferrario, J. Camacho, A. Cuoci, A. Frassoldati, E. Ranzi, H. Wang, T. Faravelli, Kinetic modeling of particle size distribution of soot in a premixed burner-stabilized stagnation ethylene flame, *Combust. Flame* 162 (2015) 3356–3369.
- [198] P.J. Coelho, P. Perez, M.E. Hafi, Benchmark numerical solutions for radiative heat transfer in two-dimensional axisymmetric enclosures with nongray sooting media, *Numer. Heat Transf., Part B* 43 (5) (2003) 425–444.
- [199] F. Liu, H. Guo, G.J. Smallwood, Effects of radiation model on the modeling of a laminar coflow methane/air diffusion flame, *Combust. Flame* 138 (2004) 136–154.
- [200] E.H. Chui, G.D. Raithby, P.M.J. Hughes, Prediction of radiative transfer in cylindrical enclosures with the finite volume method, *J. Thermophys. Heat Transf.* 6 (1992) 605–611.
- [201] N.A. Eaves, A. Veshkini, C. Riese, Q. Zhang, S.B. Dworkin, M.J. Thomson, A numerical study of high pressure, laminar, sooting, ethane-air coflow diffusion flames, *Combust. Flame* 159 (2012) 3179–3190.
- [202] J.-L. Consalvi, F. Liu, Numerical study of the effects of pressure on soot formation in laminar coflow *n*-heptane/air diffusion flames between 1 and 10 atm, *Proc. Combust. Inst.* 35 (2015) 1727–1734.
- [203] F. Cepeda, A. Jerez, R. Demarco, F. Liu, A. Fuentes, Influence of water-vapor in oxidizer stream on the sooting behavior for laminar coflow ethylene diffusion flames, *Combust. Flame* 210 (2019) 114–125.
- [204] F. Nmira, D. Burot, J.L. Consalvi, Soot emission radiation-turbulence interactions in diffusion jet flames, *Combust. Sci. Technol.* 191 (2019) 126–136.
- [205] F. Nmira, L. Ma, J.L. Consalvi, Assessment of subfilter-scale turbulence-radiation interaction in non-luminous pool fires, *Proc. Combust. Inst.* 38 (2021) 4927–4934.
- [206] K. Torres-Monclard, O. Gicquel, R. Vicquelin, A quasi-Monte Carlo method to compute scattering effects in radiative heat transfer: application to a sooted jet flame, *Int. J. Heat Mass Transf.* 168 (2021) 120915.
- [207] A. Wang, M.F. Modest, D.C. Haworth, L. Wang, Monte Carlo simulation of radiative heat transfer and turbulence interactions in methane/air jet flames, *J. Quant. Spectrosc. Radiat. Transf.* 109 (2008) 269–279.
- [208] L. Palluotto, N. Dumont, P. Rodrigues, O. Gicquel, R. Vicquelin, Assessment of randomized quasi-Monte Carlo method efficiency in radiative heat transfer simulations, *J. Quant. Spectrosc. Radiat. Transf.* 236 (2019) 106570.
- [209] J. Farmer, S. Roy, A quasi-Monte Carlo solver for thermal radiation in participating media, *J. Quant. Spectrosc. Radiat. Transf.* 242 (2020) 106753.
- [210] J.M. Suo-Anttila, T.K. Blanchat, A.J. Ricks, A.L. Brown, Characterization of thermal radiation spectra in 2 m pool fires, *Proc. Combust. Inst.* 32 (2009) 2567–2574.
- [211] F. Jiang, J.L. de Ris, H. Qi, M.M. Khan, Radiation blockage in small scale PMMA combustion, *Proc. Combust. Inst.* 33 (2011) 2657–2664.
- [212] J.-L. Consalvi, F. Liu, Radiative heat transfer through the fuel-rich core of laboratory-scale pool fires, *Combust. Sci. Technol.* 186 (2014) 475–489.
- [213] L.S. Rothman, I.E. Gordon, A. Barbe, D.C. Benner, et al., The HITRAN 2008 molecular spectroscopic database, *J. Quant. Spectrosc. Radiat. Transf.* 110 (2009) 533–572.
- [214] L.S. Rothman, I.E. Gordon, R.J. Barber, H. Dothe, R.R. Gamache, A. Goldman, V. Perevalov, S.A. Tashkun, J. Tennyson, HITEMP, the high-temperature molecular spectroscopic database, *J. Quant. Spectrosc. Radiat. Transf.* 111 (2010) 2139–2150.
- [215] J.T. Pearson, B.W. Webb, V. Solovjov, J. Ma, Effect of total pressure on the absorption line blackbody distribution function and radiative transfer in H<sub>2</sub>O, CO<sub>2</sub>, and CO, *J. Quant. Spectrosc. Radiat. Transf.* 143 (2018) 100–110.
- [216] H. Chu, M. Gu, J.-L. Consalvi, F. Liu, H. Zhou, Effects of total pressure on non-grey gas radiation transfer in oxy-fuel combustion using the LBL, SNB, SNBCK, WSGG, and FSC methods, *J. Quant. Spectrosc. Radiat. Transf.* 172 (2016) 24–35.
- [217] H. Chu, J.-L. Consalvi, M. Gu, F. Liu, Calculations of radiative heat transfer in an axisymmetric jet diffusion flame at elevated pressures using different gas radiation models, *J. Quant. Spectrosc. Radiat. Transf.* 197 (2017) 12–25.
- [218] C.M. Sorensen, Light scattering by fractal aggregates: a review, *Aerosol Sci. Technol.* 35 (2001) 3648–3687.
- [219] T.L. Farias, M.G. Carvalho, Ü.Ö. Köylü, Radiative heat transfer in soot-containing combustion systems with aggregation, *Int. J. Heat Mass Transf.* 41 (1998) 2581–2587.
- [220] V. Eymet, A.M. Brasil, M.E. Hafi, T.L. Farias, P.J. Coelho, Numerical investigation of the effect of soot aggregation on the radiative properties in the infrared region and radiative heat transfer, *J. Quant. Spectrosc. Radiat. Transf.* 74 (2002) 697–718.
- [221] F. Liu, J. Yon, A. Fuentes, P. Lobo, et al., Review of recent literature on the light absorption properties of black carbon: refractive index, mass absorption cross section, and absorption function, *Aerosol Sci. Technol.* 54 (2020) 33–51.
- [222] W.H. Dalzell, A.F. Sarofim, Optical constants of soot and their application to heat-flux calculations, *ASME J. Heat Transf.* 91 (1) (1969) 100–104.
- [223] Z.G. Habib, P. Vervisch, On the refractive index of soot at flame temperature, *Combust. Sci. Tech.* 59 (1988) 261–274.
- [224] H. Chang, T. Charalampopoulos, Determination of the wavelength dependence of refractive indices of flame soot, *Proc. R. Soc.* 430 (1990) 577–591.
- [225] V.P. Solovjov, B.W. Webb, An efficient method for modeling radiative transfer in multicomponent gas mixtures with soot, *J. Heat Transf.* 123 (2011) 450–457.
- [226] F. Cassol, R. Brittes, F.H.R. França, O.A. Ezekoye, Application of the weighted-sum-of-gray-gases model for media composed of arbitrary concentrations of H<sub>2</sub>O, CO<sub>2</sub> and soot, *Int. J. Heat Mass Transf.* 79 (2014) 796–806.
- [227] J.-L. Consalvi, F. Liu, Radiative heat transfer in the core of axisymmetric pool fires—I: evaluation of approximate radiative property models, *Int. J. Therm. Sci.* 84 (2014) 104–117.
- [228] C. Wang, M.F. Modest, B. He, Full-spectrum *k*-distribution look-up table for nonhomogeneous gas-soot mixtures, *J. Quant. Spectrosc. Radiat. Transf.* 176 (2016) 129–136.
- [229] F.R. Centeno, R. Brittes, L.G.P. Rodrigues, F.R. Coelho, F.H.R. Franca, Evaluation of the WSGG model against line-by-line calculation of thermal radiation in a non-gray sooting medium representing an axisymmetric laminar jet flame, *Int. J. Heat Mass Transf.* 124 (2018) 475–483.
- [230] P. Rivière, A. Soufiani, Updated band model parameters for H<sub>2</sub>O, CO<sub>2</sub>, CH<sub>4</sub> and CO radiation at high temperature, *Int. J. Heat Mass Transf.* 55 (2012) 3349–3358.
- [231] V. Kez, J.-L. Consalvi, F. Liu, J. Ströhle, B. Epple, Assessment of several gas radiation models for radiative heat transfer calculations in a three-dimensional oxy-fuel furnace under coal-fired conditions, *Int. J. Heat Mass Transf.* 120 (2017) 289–302.
- [232] T. Kangwanpongpan, F.H.R. Franca, R.C. da Silva, P.S. Schneider, H.J. Krautz, New correlations for the weighted-sum-of-gray-gases model in oxy-fuel conditions based on HITEMP 2010 database, *Int. J. Heat Mass Transf.* 55 (2012) 7419–7433.
- [233] M.K. Denison, B.W. Webb, A spectral line based weighted-sum-of-gray-gases model for arbitrary RTE solvers, *J. Heat Transf.* 115 (1993) 1004–1012.

- [234] M.K. Denison, B.W. Webb, The spectral-line-based weighted-sum-of-gray-gases model in nonisothermal nonhomogeneous media, *J. Heat Transf.* 117 (1995) 359–365.
- [235] M.K. Denison, B.W. Webb, The spectral-line weighted-sum-of-gray-gases model for  $H_2O/CO_2$  mixtures, *J. Heat Transf.* 117 (1995) 788–792.
- [236] M.K. Denison, B.W. Webb, Narrow-band and full-spectrum  $k$ -distributions for radiative heat transfer correlated- $k$  vs. scaling approximation, *J. Heat Transf.* 76 (2003) 69–83.
- [237] A. Cuoci, A. Frassoldati, T. Faravelli, E. Ranzi, A computational tool for the detailed kinetic modeling of laminar flames: application to  $C_2H_4/CH_4$  coflow flames, *Combust. Flame* 160 (2013) 870–886.
- [238] B. Ma, S. Cao, D. Giassi, D.P. Stocker, F. Takahashi, B.A.V. Bennett, M.D. Smooke, M.B. Long, An experimental and computational study of soot formation in a coflow jet flame under microgravity and normal gravity, *Proc. Combust. Inst.* 35 (2015) 839–846.
- [239] J. Cai, S. Lei, A. Dasgupta, M.F. Modest, D.C. Haworth, High fidelity radiative heat transfer models for high-pressure laminar hydrogen-air diffusion flames, *Combust. Theor. Model.* 18 (2014) 606–627.
- [240] F. Liu, G.J. Smallwood, W. Kong, The importance of thermal radiation transfer in laminar diffusion flames at normal and microgravity, *J. Quant. Spectrosc. Radiat. Transf.* 112 (2011) 1241–1249.
- [241] J. Contreras, J.-L. Consalvi, A. Fuentes, Numerical simulations of microgravity ethylene/air laminar boundary layer diffusion flames, *Combust. Flame* 191 (2014) 99–108.
- [242] F. Nmira, Y. Liu, J.-L. Consalvi, F. André, F. Liu, Pressure effects on radiative heat transfer in sooting turbulent diffusion flames, *J. Quant. Spectrosc. Radiat. Transf.* 2345 (2020) 106906.
- [243] H. Koseki, Large scale pool fires: results of recent experiments, *Fire Saf. Sci.* 6 (2000) 115–132.
- [244] M.H. Bordbar, G. Weceel, T. Hypanen, A line by line based weighted sum of gray gases model for inhomogeneous  $CO_2-H_2O$  mixture in oxy-fired combustion, *Combust. Flame* 161 (2014) 2435–2445.
- [245] J. Guo, X. Li, X.H. Z. Liu, C. Zheng, A full spectrum  $k$ -distribution based weighted-sum-of-gray-gases model for oxy-fuel combustion, *Int. J. Heat Mass Transf.* 90 (2015) 218–226.
- [246] L.J. Dorigon, G. Duciak, R. Brittes, F. Cassol, M. Galarca, F.H.R. Franca, WSGG correlations based on HITEMP2010 for computation of thermal radiation in non-isothermal, non-homogeneous  $H_2O/CO_2$  mixtures, *Int. J. Heat Mass Transf.* 64 (2013) 863–873.
- [247] J. Guo, L. Shen, X. He, Z. Liu, H.G. Im, Assessment of weighted-sum-of-gray-gases models for gas-soot mixture in jet diffusion flames, *Int. J. Heat Mass Transf.* 181 (2021) 121907.
- [248] J.-L. Consalvi, F. André, F.R. Coelho, F.H.R. Franca, F. Nmira, M. Galtier, V. Solovjov, B.W. Webb, Assessment of engineering gas radiative property models in high pressure turbulent jet diffusion flames, *J. Quant. Spectrosc. Radiat. Transf.* 253 (2020) 107169.
- [249] H. Chu, F. Liu, J.L. Consalvi, Relationship between the spectral line based weighted-sum-of-gray-gases model and the full spectrum  $k$ -distribution model, *J. Quant. Spectrosc. Radiat. Transf.* 143 (2014) 111–120.
- [250] B.W. Webb, V.P. Solovjov, F. André, The spectral line weighted-sum-of-gray-gases (SLW) model for prediction of radiative transfer in molecular gases, *Adv. Heat Transf.* 51 (2019) 207–298.
- [251] M.F. Modest, H. Zhang, The full-spectrum correlated- $k$  distribution for thermal radiation from molecular gas-particulate mixtures, *J. Heat Transf.* 124 (2002) 30–38.
- [252] M.F. Modest, The spectral line weighted-sum-of-gray-gases (SLW) model for prediction of radiative transfer in molecular gases, *J. Quant. Spectrosc. Radiat. Transf.* 51 (2003) 69–83.
- [253] F. André, V.P. Solovjov, D. Lemonnier, B.W. Webb, Co-monotonic global spectral models of gas radiation in nonuniform media based on arbitrary probability measures, *Appl. Math. Model.* 50 (2003) 741–754.
- [254] C. Wang, M.F. Modest, T. Ren, J. Cai, B. He, Comparison and refinement of the various full-spectrum  $k$ -distribution and spectral line weighted-sum-of-gray-gases models for nonhomogeneous media, *J. Quant. Spectrosc. Radiat. Transf.* 271 (2021) 107695.
- [255] J. Cai, M.F. Modest, Improved full-spectrum  $k$ -distribution implementation for inhomogeneous media using a narrow-band database, *J. Quant. Spectrosc. Radiat. Transf.* 141 (2014) 65–72.
- [256] V.P. Solovjov, B.W. Webb, F. André, The rank correlated SLW model of gas radiation in non-uniform media, *J. Quant. Spectrosc. Radiat. Transf.* 197 (2017) 26–44.
- [257] V.P. Solovjov, B.W. Webb, F. André, The rank correlated FSK model for prediction of gas radiation in non-uniform media, and its relationship to the rank correlated SLW model, *J. Quant. Spectrosc. Radiat. Transf.* 214 (2018) 130–132.
- [258] M.F. Modest, R.J. Riazi, Assembly full spectrum  $k$ -distribution from a narrow band database: effects of mixing gases, gases and non-gray absorbing particles and nongray scatters in non-gray enclosures, *J. Quant. Spectrosc. Radiat. Transf.* 90 (2005) 169–189.
- [259] C. Wang, W. Ge, M.F. Modest, B. He, Full-spectrum  $k$ -distribution look-up table for nonhomogeneous gas-soot mixtures, *J. Quant. Spectrosc. Radiat. Transf.* 176 (2016) 129–136.
- [260] C. Wang, B. He, M.F. Modest, T. Ren, Efficient full-spectrum correlated- $k$ -distribution look-up table, *J. Quant. Spectrosc. Radiat. Transf.* 219 (2018) 108–116.
- [261] C. Wang, B. He, M.F. Modest, Full-spectrum correlated- $k$ -distribution look-up table for radiative transfer in nonhomogeneous participating media with gas-particle mixtures, *Int. J. Heat Mass Transf.* 137 (2019) 1053–1063.
- [262] Y. Zhou, C. Wang, T. Ren, C. Zhao, A machine learning based full-spectrum correlated  $k$ -distribution model for nonhomogeneous gas-soot mixtures, *J. Quant. Spectrosc. Radiat. Transf.* 268 (2021) 107628.
- [263] R. Demarco, J.-L. Consalvi, A. Fuentes, S. Melis, Assessment of radiative property models in non-gray sooting media, *Int. J. Therm. Sci.* 50 (2011) 1672–1684.
- [264] J. Badger, B.W. Webb, V.P. Solovjov, An exploration of advanced SLW modeling approaches in comprehensive combustion predictions, *Combust. Sci. Technol.* 194 (2022) 225–241.
- [265] P.J. Coelho, Radiative transfer in combustion systems, *Handbook of Thermal Science and Engineering*, Springer International Publishing (2018), pp. 1173–1199.
- [266] C.J. Sun, C.J. Sung, H. Wang, C.L. Law, On the structure of nonsooting counterflow ethylene and acetylene diffusion flames, *Combust. Flame* 107 (1996) 321–335.
- [267] H.P. Mungekar, A. Atreya, Flame radiation and soot emission from partially premixed methane counterflow flames, *J. Heat Transf.* 128 (2006) 361–367.
- [268] H. Guo, G.J. Smallwood, The interaction between soot and NO formation in a laminar axisymmetric coflow ethylene/air diffusion flame, *Combust. Flame* 149 (2007) 225–233.
- [269] V.R. Katta, W.M. Roquemore, A. Menon, S.-Y. Lee, R.J. Santoro, T.A. Litzinger, Impact of soot on flame flicker, *Proc. Combust. Inst.* 32 (2009) 1343–1350.
- [270] M.R.J. Charest, C.P.T. Groth, Ö.L. Gülder, A numerical study on the effects of pressure and gravity in laminar ethylene diffusion flames, *Combust. Flame* 158 (2011) 1933–1945.
- [271] C.K. Law, Comprehensive description of chemistry in combustion modeling, *Combust. Sci. Technol.* 177 (2005) 845–870.
- [272] N. Slavinskaya, Skeletal mechanism for kerene combustion with PAH production, *AIAA paper* 2008-0992.
- [273] S.G. Davis, C.K. Law, H. Wang, Propene pyrolysis and oxidation kinetics in a flow reactor and laminar flames, *Combust. Flame* 119 (1999) 375–399.
- [274] R.R. Dobbins, R.J. Hall, S. Cao, B.A.V. Bennett, M.B. Colket, M.D. Smooke, Radiative emission and reabsorption in laminar, ethylene-fueled diffusion flames using the discrete ordinates method, *Combust. Sci. Technol.* 187 (2015) 230–248.
- [275] W. Pejpichestakul, A. Frassoldati, A. Parente, T. Faravelli, Soot modeling of ethylene counterflow diffusion flames, *Combust. Sci. Technol.* 191 (2019) 1473–1483.
- [276] S. Zheng, Y. Yang, R. Sui, Q. Lu, Effects of  $C_2H_2$  and  $C_2H_4$  radiation on soot formation in ethylene/air diffusion flames, *Appl. Therm. Eng.* 183 (2021) 116194.
- [277] R.R. Dobbins, J. Tinjero, J. Squeo, X. Zhao, R.J. Hall, M.B. Colket, M.B. Long, M.D. Smooke, A combined experimental and computational study of soot formation in normal and microgravity conditions, *Combust. Sci. Technol.* (2022), doi:10.1080/00102202.2022.2041621.
- [278] R.J. Santoro, T.T. Yeh, J.J. Horvath, H.G. Semerjian, The transport and growth of soot particles in laminar diffusion flames, *Combust. Sci. Technol.* 53 (1987) 89–115.
- [279] C.S. McEnally, L.D. Pfefferle, Aromatic and linear hydrocarbon concentration measurements in a non-premixed flame, *Combust. Sci. Technol.* 116–117 (1996) 183–209.
- [280] K. Maruta, M. Yoshida, H. Guo, Y. Ju, T. Niioka, Extinction of low-stretched diffusion flame in microgravity, *Combust. Flame* 112 (1998) 181–187.
- [281] G.M. Faeth, J.P. Gore, S.G. Chuech, S.M. Jeng, Radiation from turbulent diffusion flames, *Annu. Rev. Numer. Fluid Mech. Heat Transf.* 2 (1989) 1–38.
- [282] M.E. Kounalakis, J.P. Gore, G.M. Faeth, Mean and fluctuating radiation properties of nonpremixed turbulent carbon monoxide air flames, *J. Heat Transf.* 111 (1989) 1021–1030.
- [283] J.P. Gore, G.M. Faeth, Structure and spectral radiation properties of turbulent ethylene/air diffusion flames, *Proc. Combust. Inst.* 21 (1986) 1521–1531.
- [284] V.P. Kabashnikov, G.I. Myasnikov, Thermal radiation in turbulent flows-temperature and concentration fluctuations, *Heat Transf. - Sov. Res.* 17 (1985) 16–125.
- [285] P.J. Coelho, Approximate solutions of the filtered radiative transfer equation in large eddy simulations of turbulent reactive flows, *Combust. Flame* 156 (2009) 1099–1110.
- [286] J.-L. Consalvi, F. Nmira, W. Kong, On the modeling of the filtered radiative transfer equation in large eddy simulations of lab-scale sooting turbulent diffusion flames, *J. Quant. Spectrosc. Radiat. Transf.* 221 (2018) 51–60.
- [287] A.Y. Snegirev, Statistical modeling of thermal radiation transfer in buoyant turbulent diffusion flames, *Combust. Flame* 136 (2004) 51–71.
- [288] P.J. Coelho, O.J. Teerling, D. Roekaerts, Spectral radiative effects and turbulence/ radiation interaction in a non-luminous turbulent diffusion jet flame, *Combust. Flame* 133 (2003) 75–91.
- [289] J.L. Consalvi, Influence of turbulence-radiation interactions in laboratory-scale methane pool fires, *Int. J. Therm. Sci.* 60 (2012) 122–130.
- [290] T. Ren, M.F. Modest, D.C. Haworth, Simulating turbulence-radiation interactions using a presumed probability density function method, *Int. J. Heat Mass Transf.* 232 (2018) 911–923.
- [291] K.V. Deshmukh, D.C. Haworth, M.F. Modest, Direct numerical simulation of turbulence-radiation interactions in homogeneous nonpremixed combustion systems, *Proc. Combust. Inst.* 31 (2007) 1641–1648.

- [292] G. Li, M.F. Modest, Application of composition PDF methods in the investigation of turbulence-radiation interactions, *J. Quant. Spectrosc. Radiat. Transf.* 73 (2002) 461–472.
- [293] G. Li, M.F. Modest, Importance of turbulence-radiation interactions in turbulent diffusion jet flames, *J. Heat Transf.* 125 (2003) 831–838.
- [294] L. Tessé, F. Dupoirieux, J. Taine, Monte Carlo modeling of radiative transfer in a turbulent sooty flame, *Int. J. Heat Mass Transf.* 47 (2004) 555–572.
- [295] J.-L. Consalvi, F. Nmira, Effects of soot absorption coefficient-Planck function correlation on radiative heat transfer in oxygen-enriched propane turbulent diffusion, *J. Quant. Spectrosc. Radiat. Transf.* 172 (2016) 50–57.
- [296] F. Nmira, J.L. Consalvi, Local contributions of resolved and subgrid turbulence-radiation interaction in LES/presumed PDF modelling of large-scale methanol pool fires, *Int. J. Heat Mass Transf.* 190 (2022) 122746.
- [297] P. Chatterjee, Y. Wang, K.V. Meredith, S.B. Dorofeev, Application of a subgrid soot-radiation model in the numerical simulation of a heptane pool fire, *Proc. Combust. Inst.* 35 (2015) 2573–2580.
- [298] A. Snegirev, E. Markus, E. Kuznetsov, J. Harris, T. Wu, On soot and radiation modeling in buoyant turbulent diffusion flames, *Heat Mass Transf.* 54 (2018) 2275–2293.
- [299] F.C. Miranda, P. Coelho, F. di Mare, J. Janicka, Study of turbulence-radiation interactions in large-eddy simulation of scaled SANDIA flame D, *J. Quant. Spectrosc. Radiat. Transf.* 228 (2019) 47–56.
- [300] F.C. Miranda, P. Coelho, F. di Mare, J. Janicka, Large-eddy simulation of a bluff-body stabilised nonpremixed flame with radiation heat transfer, *Combust. Theor. Model.* 24 (2020) 632–649.
- [301] P.J. Coelho, A theoretical analysis of the influence of turbulence on radiative emission in turbulent diffusion flames of methane, *Combust. Flame* 160 (2013) 610–617.
- [302] G.C. Fraga, P.J. Coelho, F.H.R. Franca, Assessing individual time-averaged emission and absorption correlations for large-scale turbulent pool fires, *Int. J. Heat Mass Transf.* 165 (2021) 120665.
- [303] S.J. Fisher, B. Hardouin-Duparc, W.L. Grosshandler, The structure and radiation of an ethanol pool fire, *Combust. Flame* 70 (1987) 291–306.
- [304] S.M. Jeng, M.C. Lai, G.M. Faeth, Nonluminous radiation in turbulent buoyant axisymmetric flames, *Combust. Sci. Technol.* 40 (1984) 41–53.
- [305] S.M. Jeng, M.C. Lai, G.M. Faeth, Radiative heat fluxes near turbulent buoyant methane diffusion flames, *J. Heat Transf.* 106 (1984) 886–888.
- [306] J.P. Gore, S.M. Jeng, G.M. Faeth, Spectral and total radiation properties of turbulent carbon monoxide/air diffusion flames, *AIAA J.* 25 (1987) 339–345.
- [307] M.E. Kounalakis, J.P. Gore, G.M. Faeth, Turbulence/radiation interactions in nonpremixed hydrogen/air flames, *Proc. Combust. Inst.* 22 (1988) 1281–1290.
- [308] M.E. Kounalakis, Y.R. Sivathanu, G.M. Faeth, Infrared radiation statistics of nonluminous turbulent diffusion flames, *J. Heat Transf.* 113 (1991) 437–445.
- [309] J.-L. Consalvi, F. Nmira, Modeling of large-scale under-expanded hydrogen jet fires, *Proc. Combust. Inst.* 37 (2018) 3943–3950.
- [310] F. Nmira, J.-L. Consalvi, F. André, Pressure effects on radiative heat transfer in hydrogen/air turbulent diffusion flames, *J. Quant. Spectrosc. Radiat. Transf.* 220 (2018) 172–179.
- [311] R.S. Barlow, J.H. Frank, Effects of turbulence on species mass fractions in methane-air jet flames, *Proc. Combust. Inst.* 27 (1998) 1087–1095.
- [312] R.S. Barlow, J.D. Carter, Raman/rayleigh/LIF measurements of nitric oxide formation in turbulent hydrogen jet flames, *Combust. Flame* 97 (1994) 261–280.
- [313] G.C. Fraga, F.R. Centeno, A.P. Petry, P.J. Coelho, F.H.R. Franca, On the individual importance of temperature and concentration fluctuations in the turbulence-radiation interaction in pool fires, *Int. J. Heat Mass Transf.* 136 (2019) 1079–1089.
- [314] K.B. McGrattan, S. Hostikka, R. McDermott, J. Floyd, M. Vanella, *Fire Dynamics Simulator User's Guide*, Technical Report, National Institute of Standards and Technology, 2015.
- [315] Y.R. Sivathanu, J.P. Gore, J. Dolinar, Transient scalar properties of strongly radiating jet flames, *Combust. Sci. Technol.* 76 (1991) 45–66.
- [316] Y.R. Sivathanu, J.P. Gore, Simultaneous multiline emission absorption measurements in optically thick turbulent flames, *Combust. Sci. Technol.* 76 (1991) 1–21.
- [317] Y.R. Sivathanu, J.P. Gore, Transient structure and radiation properties of strongly radiating buoyant flames, *J. Heat Transf.* 114 (1992) 1–21.
- [318] M. Klassen, J.P. Gore, Structure and Radiation Properties of Pool Fires, Technical Report, NIST; National Institute of Standards and Technology, 1992.
- [319] L.A. Gritzo, Y.R. Sivathanu, W. Gill, Transient measurements of radiative properties, soot volume fraction and soot temperature in a large pool fire, *Combust. Sci. Technol.* 139 (1998) 113–136.
- [320] J.J. Murphy, C.R. Shaddix, Soot property measurements in a two-meter diameter JP-8 pool fire, *Combust. Sci. Technol.* 178 (2006) 865–894.
- [321] D. Zeng, P. Chatterjee, Y. Wang, The effect of oxygen depletion on soot and thermal radiation in buoyant turbulent diffusion flames, *Proc. Combust. Inst.* 37 (2019) 825–832.
- [322] W. Kollmann, I.M. Kennedy, M. Metternich, J.Y. Chen, Application of a soot model to a turbulent ethylene diffusion flame, in: H. Bockhorn (Ed.), *Soot Formation in Combustion: Mechanism and Models*, Springer-Verlag, Berlin (1994), pp. 503–526.
- [323] F. Nmira, J.-L. Consalvi, M.A. Delichatsios, Radiant fraction from sooting jet fires, *Combust. Flame* 208 (2019) 51–62.